Impact of the ^{138,139}La Radiative Strength Functions and Nuclear Level Densities on the Galactic Production of ^{138}La

by

Bonginkosi Vincent Kheswa

Dissertation presented for the degree of Doctor of Philosophy

at Stellenbosch University

Department of Physics,
University of Stellenbosch,
Private Bag X1, Matieland 7602,
South Africa.

Promoters:

Dr. Mathis Wiedeking
iThemba LABS

Prof. Paul Papka
Dept. Physics

Dr. Francesca Giacoppo
University of Oslo

December 2014

Declaration

By submitting this dissertation electronically, I declare that the entirety of the work contained therein is my own, original work, that I am the owner of the copyright thereof (unless to the extent explicitly otherwise stated) and that I have not previously in its entirety or in part submitted it for obtaining any qualification.

Date: .....

Abstract

Impact of the ^{138,139}La Radiative Strength Functions and Nuclear Level Densities on the Galactic Production of ^{138}La

B. V. Kheswa

Department of Physics,
University of Stellenbosch,
Private Bag X1, Matieland 7602,
South Africa.

Dissertation: PhD (Physics)

December 2014

^{138}La is a very long-lived and low abundant p-isotope. Most p-nuclei with $Z > 54$ are thought to be produced through photodisintegration of s- and r-process seed nuclei. However, this p-process cannot satisfactorily explain the observed abundance of ^{138}La, and more exotic processes, such as $\nu_e + {}^{138}\mathrm{Ba} \rightarrow {}^{138}\mathrm{La} + \mathrm{e}^-$ have to be considered. This ν-process can reproduce the observed solar abundance of ^{138}La, but the significance of the p-process cannot be ruled

out due to very high uncertainties in its predicted reaction rates. These errors have been discussed to be mainly due to the unavailability of the experimental nuclear level densities and radiative strength functions of ^{138,139}La, which are critical ingredients for astrophysical reaction rate calculations based on the Hauser-Feshbach approach.

Thus, nuclear physics measurements are necessary to place the nuclear properties on a strong footing, in order to make statements regarding the importance of p- and ν-processes. In this research project the experimental nuclear level densities and radiative strength functions of ^{138,139}La were measured below the neutron thresholds. From this new experimental data, the Maxwellian averaged cross sections for the ^{137}La(n, γ) and ^{138}La(n, γ) reactions, at the p-process temperature of 2.5×10^9 K, were computed with the TALYS code. Using these reaction rates the nucleosynthesis calculations in the O/Ne-rich layers of Type II supernovae were performed. The results imply that the standard p-process still under-produces ^{138}La, which puts the ν-process on a very strong footing as the main production process for ^{138}La.

Opsomming

B. V. Kheswa

Departement Fisika,
Universiteit van Stellenbosch,
Privaatsak X1, Matieland 7602,
Suid Afrika.

Proefskrif: PhD (Fisika)

Desember 2014

^{138}La is 'n p-isotoop met 'n baie lang halfleeftyd. Daar word tans vermoed dat p-nukiede met $Z > 54$ geproduseer word deur fotodisintegrasie van s- en r-proses saadnukliede. Nogtans verklaar hierdie p-proses die waargenome natuurlike voorkoms van ^{138}La nie behoorlik nie, en meer eksotiese prosesse soos byvoorbeeld $\nu_e + {}^{138}\mathrm{Ba} \rightarrow {}^{138}\mathrm{La} + \mathrm{e}^-$ moet in aanmerking geneem word. Hierdie ν-proses kan die waargenome natuurlike voorkoms van ^{138}La verklaar, maar die belangrikheid van die p-proses kan nie afgewys word nie weens die onsekerheid in die voorspelde reaksie snelheid. Sodanige onsekerhede word bespreek en word hoofsaaklik toegeskryf aan die gebrek aan eksperimentele vlakdigthede en stralings sterkefunksies van die kerne ^{138,139}La, wat van kri-

tiese belang is vir berekeninge van astrofisiese reaksie snelhede gebaseer op die Hauser-Feshbach benadering.

Kernfisiese metings is derhalwe noodsaaklik om die eienskappe van kerne op 'n stewige grondslag te plaas sodat uitlatings gemaak kan word omtrent die belangrikheid van p- en ν-prosesse. In hierdie esperimentele navorsingsprojek is die kern vlakdigthede en stralings sterkefunksies van ^{138,139}La onder die neutron reaksiedrumpels gemeet. Die nuwe gemete data maak dit moontlik om die Maxwell-gemiddelde kansvlakke vir die ^{137}La(n,γ) en ^{138}La(n,γ) reaksies by 'n p-proses temperatuur van 2.5 x 109 K met die TALYS program te bereken. Hierdie reaksie snelhede is daarna gebruik om berekeninge van elementvorming in die O/Ne-ryke lae van Tipe-II supernovas te maak. Die resultate wys uit dat die stadaard p-proses nie genoegsame ^{138}La produseer nie, wat derhalwe die ν-proses op 'n baie stewige grondslag plaas as die hoof produksie proses vir ^{138}La.

Dedication

I would like to dedicate this work to my entire family.

Acknowledgements

I'm grateful to the following:

My supervisors Dr. Mathis Wiedeking from iThemba LABS and Prof. Paul Papka for allowing me the opportunity to work on such an interesting project.

National Research Foundation (NRF) and Department of Science and Technology (DST) for financial support (PDP funding) during my studies.

University of Oslo (UiO), in particular the SAFE department, for taking shifts during the experiment and allowing me to stay for six month at the UiO in order to learn the Oslo Method.

Prof. Ole Reistad, Prof. Sunniva Siem from UiO and the Norwegian minister of foreign affairs for funding my stay at UiO, while I was learning the Oslo Method and participating in the Non-Proliferation and Disarmament Program.

My co-supervisor Dr. Francesca Giacoppo from UiO for taking her time and teach me the Oslo method.

Prof. Magne Guttormsen, Dr. Ann-Cecilie Larsen, Miss Therese Renstrøm and Mr. Tomas Eriksen for all discussions and advice they offered me during the data analysis.

iThemba LABS for buying me good computers, such as a MacBook, which made this research possible.

Prof. Stephane Goriely from the Université Libre de Bruxelles for performing astrophysical calculations using our experimental radiative strength functions and nuclear level densities.

Mrs Ntombizonke Yvonne Kheswa for manufacturing the ^{139}La target which was used in the present work.

All my supervisors for their comments on the manuscript and for their suggestions for further reading.

My girlfriend for her understanding and support when I was in Norway, for six months, working on my data analysis.

My office mates and friends for the encouragement, motivation and support they provided me during the course of my PhD.

Finally, the guidance and support I received from Dr. Mathis Wiedeking, during the entire course of my PhD work, is highly appreciated.

Contents

List of Figures

List of Tables

Chapter 1

Introduction

After the Big Bang only nuclear reactions such as primordial nucleosynthesis, β-decay and the annihilation process took place in the Universe due to high temperatures ($T_9 \approx \frac{15}{\sqrt{t}}$ for time t in seconds, where $T_9 = 1$ is equivalent to $T = 10^9$ K) and energies (order of MeV) [1]. These produced very light isotopes up to ^{7}Li and resulted in an initial composition of the universe consisting almost entirely of p, d, ^{3}He, ^{4}He, e^-, γ rays and neutrinos. After 10^5 years temperatures and energies reached $\approx 4{\times}10^3$ K and ≈ 0.4 eV, respectively, as the universe was expanding and cooling down [1]. At these temperatures and energies the electrons could remain bound to nuclei creating atoms. A billion years later stars and galaxies formed by gravitational attraction. In stars with mass $0.1M_\odot < M < 1.5M_\odot$ processes such as triple-α and hydrogen burning, which produced nuclei up to C and O, became dominant, while those stars with mass $M > 8M_\odot$ underwent the α-burning process which resulted in the formation of heavier nuclei up to ^{28}Si. As the temperature increased due to gravitational contraction, a sequence of C, O, Ne and Mg burning took place, producing nuclei up to Fe.

During α-burning phases of the red giant stars where the temperature is ≈ 1 - $3{\times}10^8$ K [2], extra neutrons in the density range of ≈ 2 - $4{\times}10^8$ cm^{-3} [2] are

produced through (α, n) reactions. These are the neutrons that drive the slow neutron capture (s)-process that synthesizes half of the observed abundance of nuclei heavier than Fe. In contrast the rapid neutron capture (r)-process takes place during explosive scenarios such as core collapse supernovae where there are high neutron densities ($> 10^{20}$ cm^{-3}) and temperatures (≈ 2 - 3×10^{9} K). Once the r-process ceases these radioactive nuclei β-decay to stable nuclei up to the actinide region. This process produces heavy neutron rich isotopes up to U where fission begins to be more probable. Figure 1.1 illustrates the r-process path.

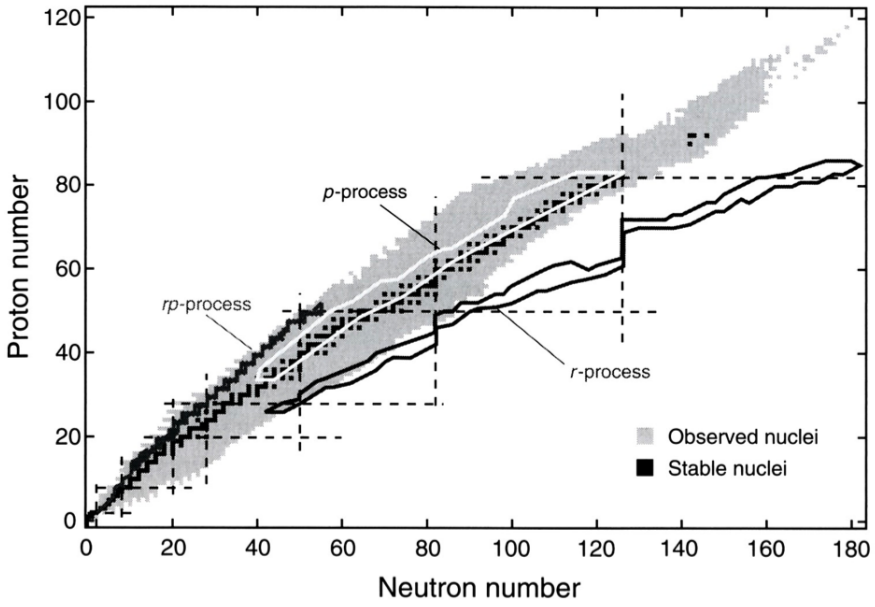

Figure 1.1: Illustration of r-, rp- and p-processes paths[1].

Even though most isotopes heavier than Fe result from s- and r-processes there are proton-rich (p)-isotopes, ranging from Se to Hg, that cannot be produced in this fashion [3], because they are shielded from these processes by the valley of β stability. Several other processes by which p-isotopes can be produced are invoked. Nuclei with low-proton numbers are produced by the rapid proton capture (rp)-process in high-temperature and proton-rich environments, such as found in neutron stars where high-proton densities are transfered from

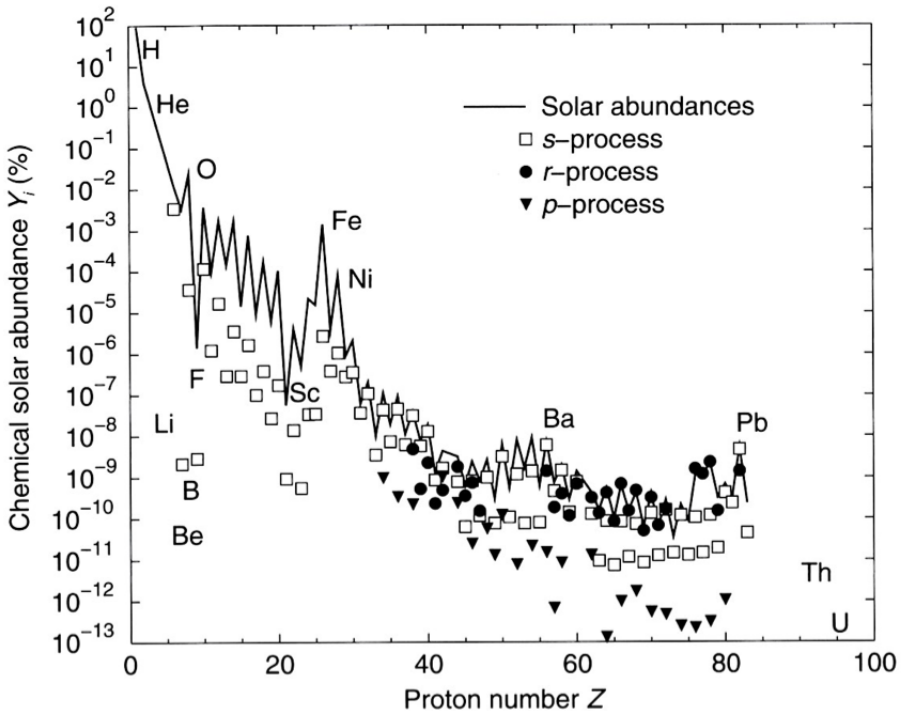

Figure 1.2: The contribution of s-, r- and p-processes on solar abundances [1].

the companion star to the neutron star. However this synthesis is limited to nuclei with $Z \leq 54$ due to the SnSbTe cycle [4] where α-decay terminates the rp-process. Thus the photodisintegration (p)-process that occurs in the O/Ne-rich layers of core-collapse supernovae remains the main source to create heavier p-isotopes. Above Te, p-nuclei are synthesized in three ways: i) through destruction of their neutron richer isotopes by successions of (γ, n) reactions, ii) through photodisintegration reactions such as (γ, p) and (γ, α) reactions and iii) through β-decay of nuclei produced in the p-process. The paths of the rp- and p-processes are also demonstrated in figure 1.1. Figure 1.2 shows the contribution of s-, r- and p-processes on solar system abundances.

1.1 Physics Motivation and Objectives

The p-process can explain the abundance of most heavy p-nuclei. The odd-odd neutron-deficient ^{138}La is very long-lived (half-life of $\approx$ 100 Gyr) but one of

the least abundant ($\approx 0.1\%$ natural abundance) nuclei in the solar system and the p-process cannot satisfactorily explain its observed solar abundance. This is demonstrated by figure 1.3 where ^{138}La is calculated to be under-produced by more than a factor of 10.

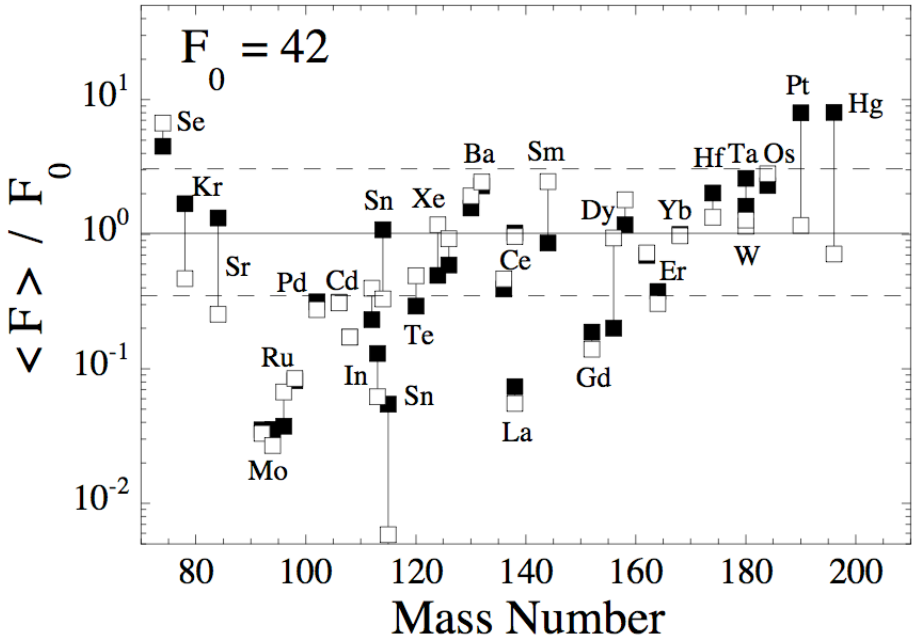

Figure 1.3: The p-abundance expressed by means of a normalized overproduction factor, $\langle F \rangle / F_0$, as function of mass number A computed by Ref. [3] (open squares) and Ref. [5] (black squares), using different sets of nuclear reaction rates. The ν-processes were not included in these calculations.

Hence, more exotic reactions such as neutrino (ν) processes have been proposed to explain its synthesis [6, 7]. These reactions can explain the observed solar abundance of ^{138}La through $\nu_e + {}^{138}\mathrm{Ba} \rightarrow \mathrm{e}^- + {}^{138}\mathrm{La}$ (see figure 1.4 for illustration). Nevertheless, the significance of the p-process cannot be ruled out due to the limited knowledge and uncertainties of nuclear properties entering the ^{138}La production, such as the nuclear level densities (NLD) and radiative strength function, (RSF) [3]. Although, these are critical ingredients of the Hauser-Feshbach formalism [8] on which the astrophysical reaction rate calculations are based, they have never been measured below the neutron binding

energy for ^{138}La and below 6 MeV for ^{139}La [9] which is the significant γ ray energy region for the synthesis of ^{138}La. It has been even pointed out in Ref. [3] that the errors related to these nuclear properties can amount to a factor of ≈ 2 for $^{139}\mathrm{La}(\gamma, n)^{138}\mathrm{La}$ and $^{138}\mathrm{La}(\gamma, n)^{137}\mathrm{La}$ (production and destruction of ^{138}La) at the relevant p-process peak temperature $T_9 \approx 2.5$.

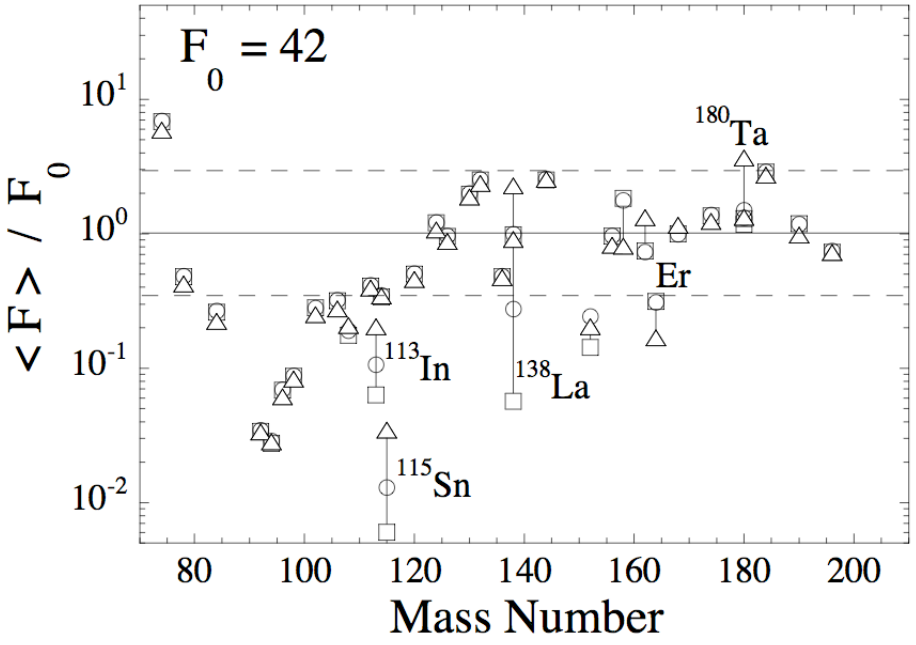

Figure 1.4: The p-abundance obtained with neutrino luminosities $L_\nu[10^{51}$ ergs $\mathrm{s}^{-1}] = (3, 4, 16)$ (circles) and (30, 40, 160) (triangles) for (ν_e, $\bar{\nu}_e$, ν_x), and without (squares) ν interaction [3].

Nuclear cosmochronometers are also of great interest in nucleosynthesis studies. They are used to measure ages of nucleosynthesis processes and hence stellar ages. For example U, which was suggested by Rutherford as a potential chronometer, has been used to estimate the stellar age [10]. In total there are six known very long-lived nuclear chronometers with half-life on the order of Gyr namely ^{238}U, ^{40}K, ^{232}Th, ^{87}Rb, ^{187}Re and ^{176}Lu [7]. These chronometers can only be used to measure ages of s- and r-processes, but there is no nuclear cosmochronometer for ν-processes. However, if ^{138}La is synthesized in the ν-

process, its long half-life of $\approx$ 100 Gyr may be used to estimate the elapsed time from its creation to the present time.

Clearly the nuclear physics parameters (NLD and RSF) and their uncertainties must be carefully measured to be able to confidently use the results in model calculations and to unambiguously investigate the importance of the p-process and / or ν_e-process as the main process for the production of ^{138}La.

The objectives of this thesis are the following: i) measure the RSF and NLD of ^{138,139}La using the ^{139}La(^{3}He, ^{3}Heγ)^{139}La and ^{139}La(^{3}He, α)^{138}La reactions with the so-called Oslo Method, ii) calculate the ^{137}La(n,γ) and ^{138}La(n,γ) cross-sections using the newly measured RSF and NLD obtained with Hartree-Fock-Bogoliubov (HFB) + Combinatorial model [11] as input parameters, iii) determine the corresponding astrophysical Maxwellian-average cross-sections at the p-process temperature and investigate their impact on ^{138}La p-process production and destruction, iv) address the astrophysical implications regarding p- and ν_e-processes.

Chapter 2

Theory and Literature Review

2.1 Oslo Method

The Olso Method is a model dependent experimental technique, based on the Brink hypothesis, for the simultaneous extraction of radiative strength function, RSF, and nuclear level density, NLD. This method was developed by the nuclear physics group at the University of Oslo in the 1980s and has received plenty of global recognition in the field of nuclear physics and nuclear astrophysics. It consists of three major steps: 1) unfolding of the continuum γ ray spectrum, 2) extraction of the primary γ ray matrix and 3) simultaneous extraction of the RSF and NLD. These major steps are discussed below. The detailed review of this method is provided in Refs. [12, 13].

2.1.1 Unfolding of a continuum γ ray spectrum

A statistical γ ray spectrum is a broad energy distribution with γ ray energy peaks which are closely spaced and unresolvable with the currently available experimental resolution. This spectrum consists of contributions from different processes in which γ rays interact with matter. These are photoelectric effects, pair production and Compton scattering and all have different energy depen-

dences. To obtain a true full energy spectrum an experimentally observed γ ray spectrum has to be properly unfolded to eliminate contributions from pair production and Compton scattering. This is achieved using the Compton subtraction method which makes use of the experimentally measured response functions, $R(E, E_\gamma)$, where E is the energy deposited by the γ ray with an initial energy of E_γ.

2.1.2 Detector Response Matrix

Ideally, $R(E, E_\gamma)$ must be experimentally established for all possible E_γ but this is impractical. As a result, $R(E, E_\gamma)$ can only be measured for a finite number of γ ray transitions. By interpolating between the spectra of those transitions, $R(E, E_\gamma)$ for all possible E_γ can be determined. In the case of the NaI(Tl) (Sodium Iodide doped with Thallium) detectors (referred to as the CACTUS array see chapter 3) ten $R(E, E_\gamma)$ of monoenergetic γ rays were measured in the energy region of 122 - 15110 keV [14]. The full energy, double escape, single escape and annihilation peaks have been removed from these response functions due to the following reasons:

(i) To simplify the interpolation between response functions since the positions and intensities have different energy dependence.

(ii) To be able to easily create a new response matrix with the appropriate energy resolution, in cases where the actual experimental resolution differs from the resolution of the observed response functions.

(iii) To be able to smooth the components of the spectrum with different energy resolutions (see section 2.1.4).

The interpolated full energy, single escape, double escape and annihilation peaks can be obtained by fitting the Gaussian function at interpolated E_γ.

The observed Compton background spectra of different E_γ differ in dynamical range (see figure 2.1). Hence, the interpolation is performed between channels that correspond to the same γ ray Compton scattering angle θ as illustrated in figure 2.1.

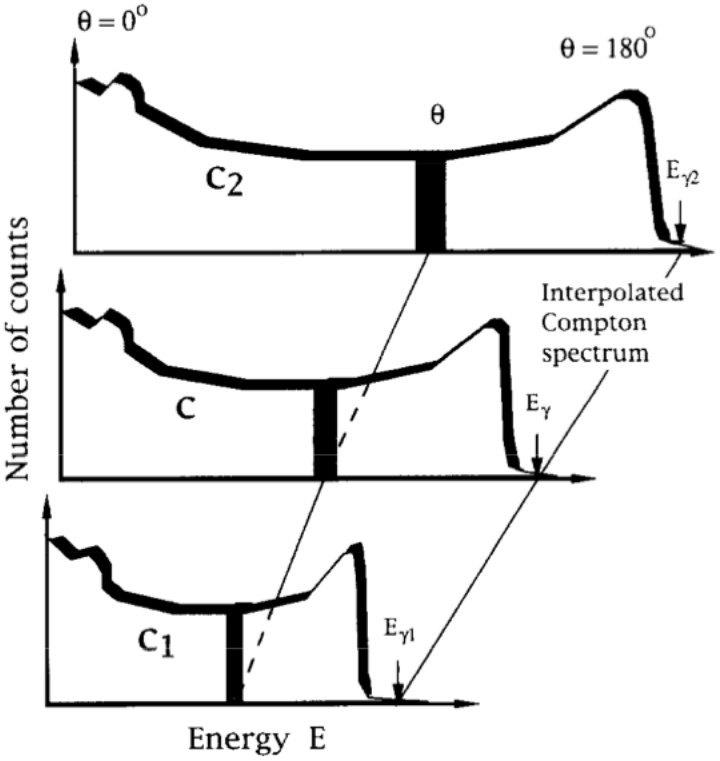

Figure 2.1: Interpolation of the Compton part from measured response functions c_1 and c_2 [14].

The counts of the interpolated Compton background at a given θ are calculated using [14]

$$c(E) = \left(\frac{dE}{d\theta}\right)^{-1}_{E_\gamma} \left(c_1(E_1) \left(\frac{dE}{d\theta}\right)_{E_{\gamma 1}} + \frac{E_\gamma - E_{\gamma 1}}{E_{\gamma 2} - E_{\gamma 1}} \right) \times \left(c_2(E_2) \left(\frac{dE}{d\theta}\right)_{E_{\gamma 2}} - c_1(E_1) \left(\frac{dE}{d\theta}\right)_{E_{\gamma 1}} \right), \tag{2.1}$$

where E_γ, $E_{\gamma 1}$, $E_{\gamma 2}$ are centroids of the full energy peaks of the interpolated spectrum and reference spectra. The corresponding energies that the electrons deposit in the detector due to Compton scattering at angle θ are denoted by E, E_1 and E_2. The quantities $\left(\frac{dE}{d\theta}\right)_{E_\gamma}$, $\left(\frac{dE}{d\theta}\right)_{E_{\gamma 1}}$ and $\left(\frac{dE}{d\theta}\right)_{E_{\gamma 2}}$ take into account the fact that the detected energy of a Compton scattered γ ray strongly depends on θ and γ ray energy.

In the E_γ region of 0 - $E_{b.sc}$, where $E_{b.sc}$ is the backscattering energy, a spectrum is dominated by background events such as X rays. Therefore, in this region the interpolation is performed between the same channel numbers. In the energy region above the Compton edge the Compton spectrum shows few counts and therefore this region should also be interpolated. The interpolation in this region is also performed between the same channel numbers.

2.1.3 The Folding Iteration Method

The Compton subtraction method requires an unfolded γ ray spectrum, u, as a starting point. The unfolded spectrum is obtained using the difference approach of the folding iteration method which allows u to be obtained using [14],

$$f = \boldsymbol{R}u \tag{2.2}$$

where f and $\boldsymbol{R}$ represent the folded γ ray spectrum and response matrix of the CACTUS array, respectively.

This means that more improved trial spectra u can be obtained, folded and compared to the observed spectrum r. The entries of $\boldsymbol{R}$ are response functions, R_{ij}, at channel i for E_γ that corresponds to channel j. The folding iteration method consists of the following steps:

i) The observed spectrum r is used as a first trial spectrum: $u^0 = r$

ii) u^0 is folded using equation (2.2) giving f^0

iii) The next trial function, u^1, is calculated from $u^1 = u^0 + (r - f^0)$

iv) u^1 is folded according to equation (2.2) to obtain f^1

v) Use this f^1 to calculate the next trial spectrum u^2 from $u^2 = u^1 + (r - f^1)$

The procedure is repeated until $f^i \approx r$ where i is the number of iterations which is typically 10 - 30.

2.1.4 The Compton Subtraction Method

Once the unfolded spectrum u is obtained, it can be used to produce a much less fluctuating unfolded spectrum using the Compton subtraction method [14]. This method begins by defining a new spectrum,

$$v(i) = p_f(i)u(i) + w(i) \tag{2.3}$$

which represents the observed spectrum minus Compton contribution. The first term $p_f(i)u(i)$ represents the full energy contribution at channel number i and probability, p_f, that an event corresponds to the full energy peak can be obtained from Ref. [14]. The second term $w(i) = u_s(i - i_{511}) + u_d(i - i_{1022}) + u_a(i_{511})$ includes the contribution from single escape, double escape and annihilation processes, respectively. These contributions are expressed as

$$u_s(i - i_{511}) = p_s(i)u(i) \tag{2.4}$$

$$u_d(i - i_{1022}) = p_d(i)u(i) \tag{2.5}$$

$$u_a(i_{511}) = \sum_i p_a(i)u(i) \tag{2.6}$$

where i_{511} and i_{1022} are channels with $E_\gamma = 511$ keV and 1022 keV, respectively. The probabilities p_s, p_d and p_a, that an event belongs to a single escape or double escape or annihilation peak are taken from Ref. [14].

The u_a spectrum has all its counts in channel i_{511} and has to be smoothed with a resolution of 1.0 FWHM (full width at half maximum) to obtain the energy resolution of the experimentally observed spectrum [14]. The energy resolution of u_s, $p_f(i)u(i)$ and u_d spectra are determined by the energy resolutions of the observed spectrum, 1.0 FWHM, and the response matrix, 0.5 FWHM, yielding $\sqrt{1.0^2 - 0.5^2}$ FWHM $= 0.87$ FWHM. Hence, these spectra are smoothed with additional 0.5 FWHM to obtain a spectrum with the observed resolution of 1.0 FWHM.

The Compton background spectrum, $c(i)$, is then extracted by subtracting the new spectrum $v(i)$ from the observed $r(i)$ and this yields

$$c(i) = r(i) - v(i). \tag{2.7}$$

The counts of this spectrum strongly fluctuate from channel to channel because it depends on the fluctuating unfolded spectrum u. This needs to be corrected since the Compton background is supposed to be a slow varying function of E_γ. Hence it is smoothed using the resolution of 1.0 FWHM [14]. The replacement

of $c(i)$ by $c_{smoothed}(i)$ and substitution of equation (2.3) into equation (2.7) results in,

$$u(i) = \frac{1}{p_f}[r(i) - c_{smoothed}(i) - w(i)] \tag{2.8}$$

which is the new and less fluctuating unfolded γ ray spectrum. Once the unfolded spectrum has been obtained it should be corrected for the energy dependent γ ray total detection efficiency, $\epsilon_{tot}(i)$, which is also multiplied by the efficiency due to the discriminator threshold. Thus the true unfolded γ ray spectrum, $u_{true}(i)$, is given by

$$u_{true}(i) = \frac{u(i)}{\epsilon_{tot}(i)}. \tag{2.9}$$

This is a spectrum from which a matrix of excitation energy, E_x, vs primary γ rays is constructed. Figure 2.2 shows examples of unfolded spectra, u, obtained using a Compton subtraction method, corresponding raw γ ray spectra, r, and Compton background spectra, c, obtained using equation (2.7).

2.1.5 The First Generation Method

The first generation method is an iterative procedure which is used to extract an E_x vs primary γ ray matrix from an unfolded E_x vs γ ray matrix. It is based on the assumption that states populated through the first γ ray transitions have the same decay properties as states populated directly in the particle reaction at that excitation energy.

The unfolded E_x vs γ ray matrix is divided into excitation energy bins of about 200 keV width depending on the experimental energy resolution. The first generation γ ray spectrum of each E_x bin is estimated by [15]

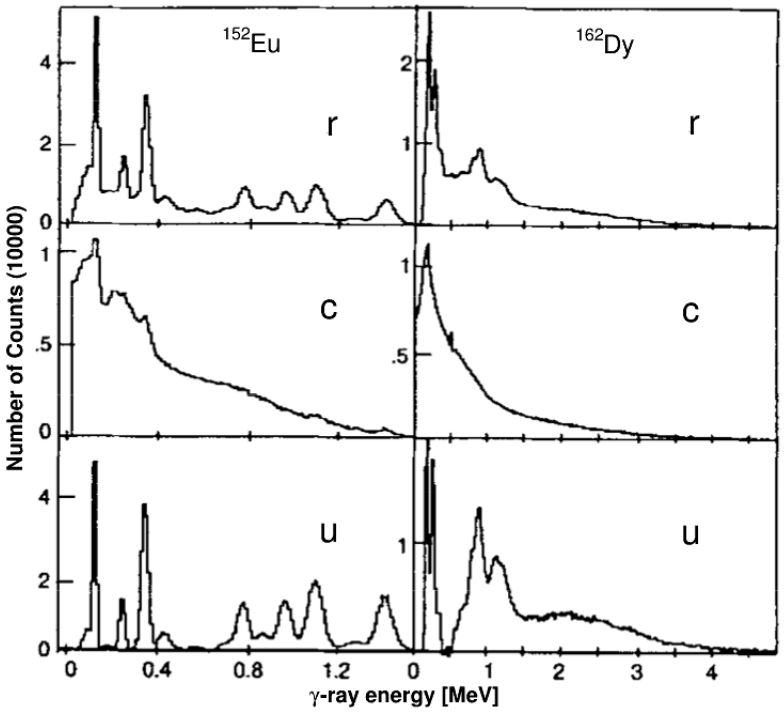

Figure 2.2: The raw (r), Compton (c) and unfolded (u) spectra of ^{152}Eu and ^{162}Dy. This figure is modified from Ref. [14].

$$h_i = f_i - g_i \tag{2.10}$$

where f_i is a γ ray spectrum of excitation energy bin i and g_i is a weighted sum of all spectra of the excitation bins $j < i$ that is

$$g_i = \sum_{all j<i} n_{ij} w_{ij} f_j. \tag{2.11}$$

The coefficients n_{ij} are correction factors for the different cross-sections of populating levels in bin i and underlying levels in bin j. They are determined in such a way that the product of the total area of each spectrum f_i and n_{ij} yields the same number of cascades. This is achieved using the multiplicity normalization method that was discussed in Ref. [16] and hence

$$n_{ij} = \frac{\langle M_j \rangle A_i}{\langle M_i \rangle A_j} \tag{2.12}$$

where $\langle M_j \rangle$ and A_j are the average multiplicity of γ ray in bin j and the total number of counts of spectrum f_j, respectively. The average multiplicity of γ rays can be determined from [13],

$$\langle M_j \rangle = \frac{E_x^j}{\langle E_\gamma \rangle} \tag{2.13}$$

where E_x^j and $\langle E_\gamma \rangle$ are excitation energy of bin j and average γ ray energy of the γ ray spectrum f_j. The weighting function w_{ij} is the probability of decay from bin i to bin j and $\sum_j w_{ij} = 1$. Hence, the distribution of w_{ij} is the same as h_i that is unfolded with the response function of the CACTUS multi-detector array. This close relationship between w_{ij} and h_i is used to determine them simultaneously through the following fast converging iterative procedure:

i) Define the trial function w_{ij}, it can be an unfolded spectrum f_i or a constant function

ii) Use w_{ij} from step i) to calculate h_i

iii) Transform h_i to w_{ij}, i.e. give h_i the same energy calibration as w_{ij} and normalize the area h_i to 1

iv) If the current $w_{ij} \approx$ previous w_{ij} then convergence is achieved, which takes typically 10 - 30 iterations

v) Otherwise start from step ii)

In cases when M_i is well determined an area consistency check can be applied to equation (2.10) so that the area of the first generation matrix is $A(h_i) = A(f_i) - \alpha A(g_i)$, where the correction factor α, which is close to unity, is given by $\alpha = \left(1 - \frac{1}{M_i}\right) \frac{A(f_i)}{A(g_i)}$. This factor is useful in cases where there is an improper choice of the weighting function. Figure 2.3 illustrates the first generation method. The typical primary γ ray matrix that is extracted with the above method is shown in figure 2.4 together with its corresponding unfolded matrix obtained using the unfolding procedure discussed in the previous section.

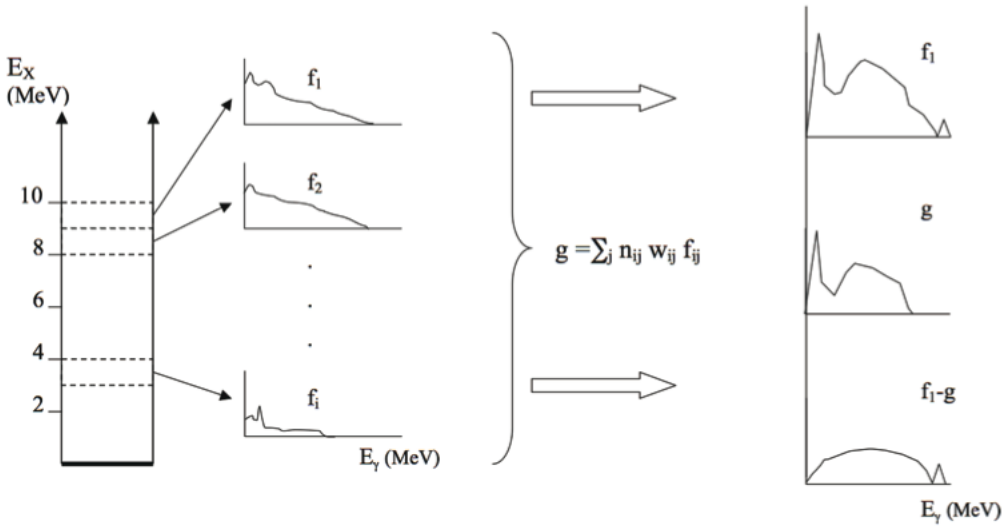

Figure 2.3: Extraction of the first generation matrix [15].

2.1.6 Extraction of Radiative Strength Function and Nuclear Level Density

According to Fermi's Golden Rule the decay probability, λ_{if}, between every initial state i and final state f is proportional to the transition matrix element, $|\langle f|H'|i\rangle|^2$, and the level density at the final state, $\rho(E_f)$ [17]. That is $\lambda_{if} = \frac{2\pi}{\hbar}|\langle f|H'|i\rangle|^2\rho(E_f)$. Further, the primary γ ray matrix is proportional to the decay probability of emitting a γ ray of energy E_γ. The assumption that the residual nucleus reaches a compound-like state before γ ray emission means

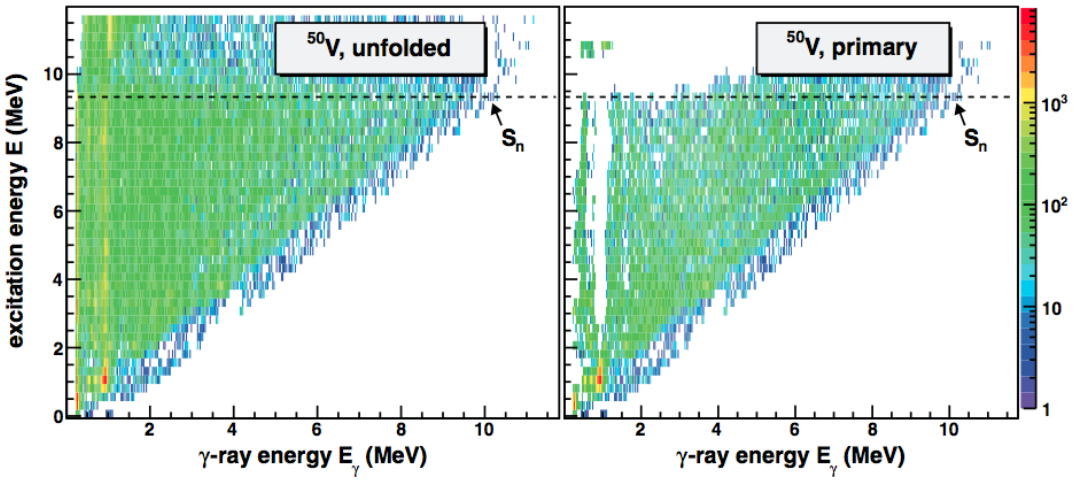

Figure 2.4: The unfolded and first generation matrices of ^{50}V [13].

that the relative probability for decay into any specific set of final states is independent of how the compound nucleus was formed [18]. Hence an equivalent decay probability expression for the primary γ ray matrix can be written as $P(E_i, E_\gamma) \propto \rho(E_f)\mathcal{T}_{if}$, where $\mathcal{T}_{if}$ is the γ ray transmission coefficient for the γ decay from state i to state f [12, 13]. The Brink hypothesis states that a giant electric dipole resonance (GEDR) can be built on every excited state and its properties do not depend on the temperature of the nuclear state on which it is built [19]. Assuming that the Brink hypothesis is valid and generalizing it to any type of collective excitation means that the γ ray transmission coefficient does not dependent on the properties of the initial and final states. It only depends on the γ ray energy E_γ. As a result $\mathcal{T}_{if}$ can be replaced by $\mathcal{T}(E_\gamma)$. Therefore, a first generation matrix can be factorized as [12]:

$$P(E_x, E_\gamma) \propto \rho(E_f)\mathcal{T}(E_\gamma) \tag{2.14}$$

where $\mathcal{T}(E_\gamma)$ and $\rho(E_f)$ are the γ ray transmission coefficient and level density at $E_f = E_x - E_\gamma$, respectively. It should the emphasized that this relation is only applicable at high excitation energy since it only holds for compound

states with higher degrees of freedom. The $\mathcal{T}(E_\gamma)$ and $\rho(E_f)$ are extracted by fitting theoretical first generation matrices $P_{th}(E_x, E_\gamma)$ to the experimental $P(E_x, E_\gamma)$ and by minimizing

$$\chi^2 = \frac{1}{N} \sum_{E_x} \sum_{E_\gamma} \frac{(P_{th}(E_x, E_\gamma) - P(E_x, E_\gamma))}{\Delta P(E_x, E_\gamma)} \tag{2.15}$$

where N and $\Delta P(E_x, E_\gamma)$ are the degrees of freedom and the uncertainty in the primary matrix according to the iterative procedure presented in Ref. [12] and

$$P_{th}(E_x, E_\gamma) = \frac{\rho(E_f)\mathcal{T}(E_\gamma)}{\sum_{E_\gamma} \rho(E_f)\mathcal{T}(E_\gamma)}. \tag{2.16}$$

Figure 2.5 shows an example of a fitted and factorized region of $P(E_x, E_\gamma)$ and corresponding $P_{th}(E_x, E_\gamma)$.

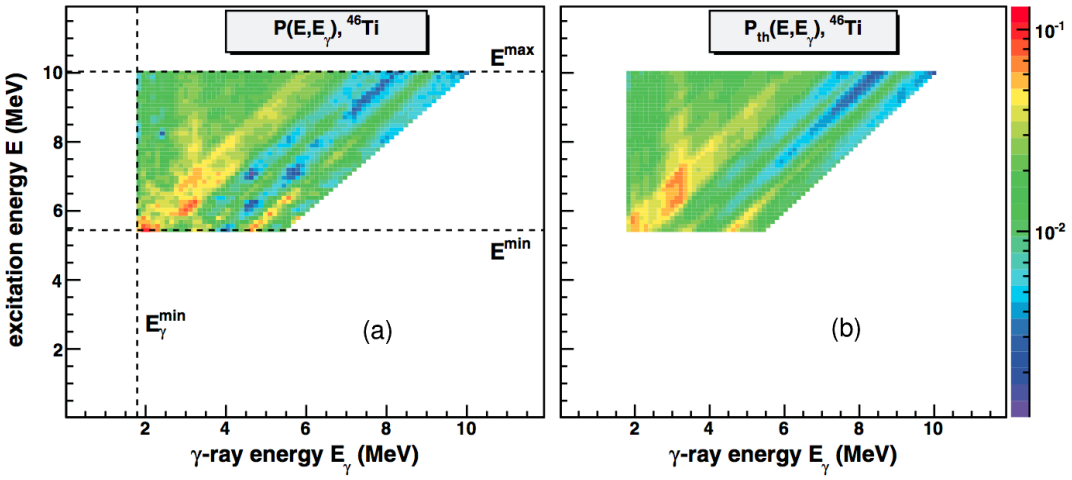

Figure 2.5: Example of a fitted region of a $P(E_x, E_\gamma)$ (a) and corresponding $P_{th}(E_x, E_\gamma)$ (b) [13].

Once the $\rho(E_f)$ and $\mathcal{T}(E_\gamma)$ have been extracted, infinitely many solutions of $P(E_x, E_\gamma)$ can be found of the form

$$\tilde{\rho}(E_f) = A\rho(E_f)e^{\alpha E_f} \tag{2.17}$$

$$\tilde{\mathcal{T}}(E_\gamma) = B\mathcal{T}(E_\gamma)e^{\alpha E_\gamma}. \tag{2.18}$$

The α parameter is the common slope between $\tilde{\rho}(E_f)$ and $\tilde{\mathcal{T}}(E_\gamma)$ and A and B are normalization parameters. The parameters α and A are obtained by normalizing $\tilde{\rho}$ to $\rho(S_n)$ and the level density of known discrete states, where S_n is the neutron separation energy. Note that, for simplicity, in the remainder of this thesis the notations $\mathcal{T}$ and ρ are used instead of $\tilde{\mathcal{T}}$ and $\tilde{\rho}$. The $\rho(S_n)$ can be calculated from [13]

$$\rho(S_n) = \frac{2\sigma^2}{D_0(J_T+1)e^{[-(J_T+1)^2/2\sigma^2]} + e^{\left(-J_T^2/2\sigma^2\right)}J_T} \tag{2.19}$$

where σ, D_0, J_T are a spin cut-off parameter, average neutron resonance spacing and spin of a target nucleus in (n,γ) reactions, respectively. The average neutron resonance spacing and J_T can be obtained from Refs. [20, 21], respectively. The spin cut-off parameter is obtained from the back-shifted Fermi gas formula (see section 2.2.1).

The absolute normalization parameter B is calculated from the experimental average total radiative width $\langle \Gamma_\gamma(S_n,\ J_T, \pi_T)\rangle$ according to [13],

$$\langle \Gamma_\gamma(S_n, J_T \pm \frac{1}{2}, \pi_T)\rangle = \frac{D_0}{4\pi}\int_0^{S_n} dE_\gamma \mathcal{T}(E_\gamma)\rho(S_n - E_\gamma) \times \sum_{J=-1}^{1} g(S_n - E_\gamma, J_T \pm \frac{1}{2} + J) \tag{2.20}$$

where J_T, π_T are the spin and parity of the target nucleus in the (n, γ) reactions, and $\rho(S_n - E_\gamma)$ is the experimental level density. The spin distribution is defined as [13]

$$g(E_x, J) = \frac{2J+1}{2\sigma^2} e^{(-(J_T+1)^2/2\sigma^2)}, \tag{2.21}$$

and normalized to $\sum_J g(E_x, J) \approx 1$. The typical spin distribution that has been used in the method is shown in figure 2.6. In this figure the solid lines were calculated with equation (2.21) while the open squares were predicted with the Combinatorial Bardeen-Cooper-Schrieffer (BCS) model [22], for the ^{119}Sn(^{3}He, $\alpha\gamma$)^{118}Sn reaction.

The γ ray transmission coefficient and radiative strength function are related according to

$$\mathcal{T}_{XL}(E_\gamma) = 2\pi E_\gamma^{2L+1} f_{XL}(E_\gamma). \tag{2.22}$$

Assuming that the statistical decay is dominated by $E1$ and $M1$ transitions means that

$$\mathcal{T}(E_\gamma) = \mathcal{T}_{E1}(E_\gamma) + \mathcal{T}_{M1}(E_\gamma), \tag{2.23}$$

and the radiative strength function, $f(E_\gamma)$, is given by

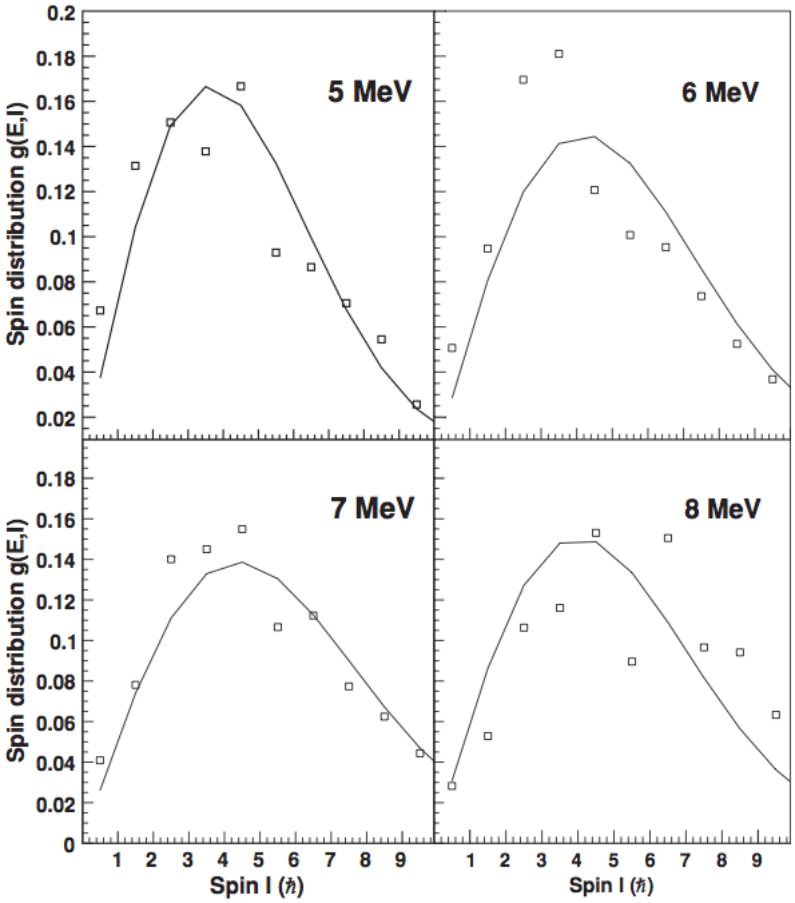

Figure 2.6: Spin distribution used for ^{118}Sn for different E_x [23].

$$f(E_\gamma) = f_{E1}(E_\gamma) + f_{M1}(E_\gamma) = \frac{\mathcal{T}(E_\gamma)}{2\pi E_\gamma^3}. \tag{2.24}$$

This also implies that the α parameter is the common slope between $\rho(E_f)$ and $f(E_\gamma)$.

Figures 2.7 and 2.8 show the typical nuclear level densities, transmission coefficients and radiative strength functions that have been obtained using the Oslo method. In figure 2.7 (upper panel) the open square at $\approx$ 7.7 MeV is the $\rho(S_n)$ calculated using equation (2.19). The dotted line is the interpolation between $\rho(S_n)$ and experimental data using the back-shifted Fermi gas model (see section 2.2.1). The solid line at low energies is the level density of

known discrete states. The two sets of vertical arrows show the regions where a χ^2 minimization is performed between the density of discrete states and the interpolated level density. In the lower panel the solid line represents the extrapolation of $\mathcal{T}(E_\gamma)$ and the vertical arrows show the two regions where the χ^2 minimization has been performed between the experimental data and the extrapolation. The $f(E_\gamma)$ in figure 2.8 was extracted by factorizing $P(E_x, E_\gamma)$ in three different excitation energy regions. It is interesting to note that the shape of the $f(E_\gamma)$ is independent of the E_x region. This feature strongly supports the Brink hypothesis.

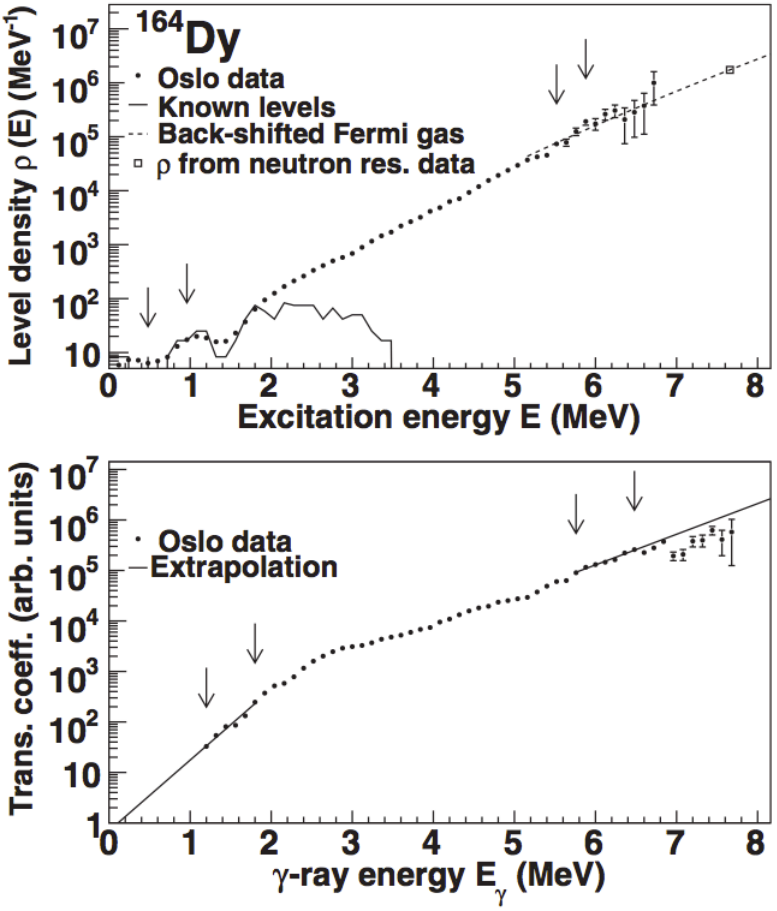

Figure 2.7: Nuclear level density and transmission coefficient of ^{164}Dy [24].

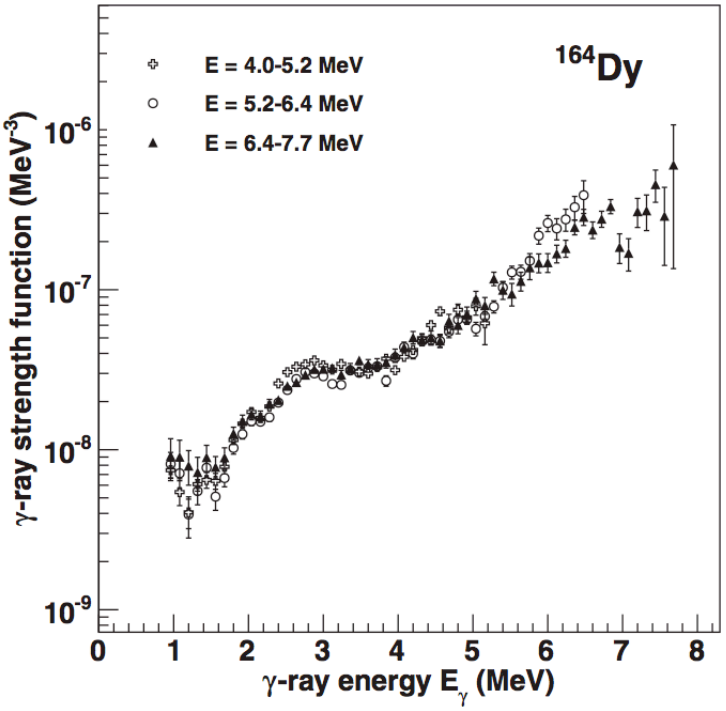

Figure 2.8: Radiative strength function of ^{164}Dy in three regions of excitation energy[13].

2.2 Nuclear Level Density

A nucleus can be excited to numerous higher energy quantum states. At low excitation energies, E_x, the nuclear excited states display a discrete spectrum. The number and widths of these levels increase as the excitation energy approaches the neutron separation energy S_n. These excited states eventually overlap creating a quasicontinuum (see figure 2.9 for illustration), which is impossible to resolve with the present experimental detection resolution. The E_x at which the quasicontinuum begins depends on the mass of the nucleus, A. At such high energies the nuclear levels are described using nuclear level density models that define it as a function of E_x, and spin and parity, J^π. These models predict the level density as an exponential function of E_x which is consistent with a cumulated discrete level histogram showing a level density integral up to a specified excitation energy as a function of E_x. The observed

weak mean-spacing of s-wave resonances, D_0, in neutron resonance experiments is an indication of the existence of up to 10^9 levels per few MeV, which also confirms the exponential increase in the number of quantum states.

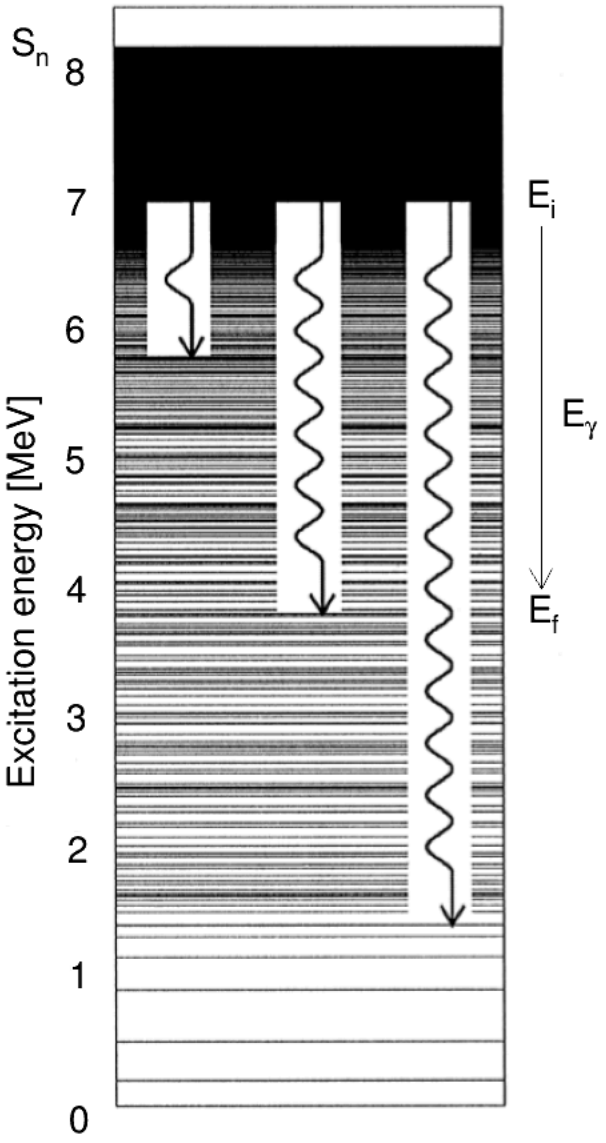

Figure 2.9: The nuclear level density as function of excitation energy. This figure has been modified from Ref. [12].

There are various nuclear level density models in the literature that may be used for practical applications. However, this thesis will only focus on those

that have been found applicable to this research project and these are discussed below.

2.2.1 Back-Shifted Fermi Gas Model

In 1965 Gilbert and Cameron proposed a back-shifted Fermi gas (BSFG) model for nuclear level density which can be used when there is no experimental information known about the nucleus in question [25]. They suggested that for high energies the density of levels with spin and parity, J^π, at E_x is given by

$$\rho(E_x, J^\pi) = \frac{(2J+1)e^{(-(J+\frac{1}{2})^2/2\sigma^2)}}{2\sqrt{2\pi}\sigma^3}\frac{\sqrt{\pi}}{12}\frac{e^{(2\sqrt{aU})}}{a^{\frac{1}{4}}U^{\frac{5}{4}}} \tag{2.25}$$

which is integrated over all possible J^π and yields the density of levels for all J^π at a given E_x

$$\rho(E_x) = \frac{\sqrt{\pi}}{12}\frac{e^{(2\sqrt{aU})}}{a^{\frac{1}{4}}U^{\frac{5}{4}}}\frac{1}{\sqrt{2\pi}\sigma}. \tag{2.26}$$

where U, σ^2 are back-shifted excitation energy and spin cut-off parameter, respectively, and are given by

$$U = E_x - E_1 \tag{2.27}$$

$$\sigma^2 = 0.0888A^{\frac{2}{3}}\sqrt{a(S_n - E_1)}. \tag{2.28}$$

The level density parameter a and back-shift parameter E_1 can be obtained

from Ref. [26]. The parameter a can also be calculated from total shell corrections as follows

$$\frac{a}{A} = 0.00917S + 0.142 \tag{2.29}$$

and

$$\frac{a}{A} = 0.00917S + 0.120 \tag{2.30}$$

where A and S are the nuclear mass and total shell correction, respectively, and S can be obtained from Ref [25]. Equation (2.29) is for spherical nuclei while (2.30) is for deformed nuclei.

In 2009 Egidy and Bucurescu proposed that a spin cut-off parameter as a function of A and E_x for the BSFG model can also be calculated with [26]:

$$\sigma^2 = 0.391A^{0.675}(E_x - 0.5Pa')^{0.312} \tag{2.31}$$

where Pa' is the deuteron pairing energy.

2.2.2 Constant Temperature Model

The constant temperature (CT) model assumes a nearly constant nuclear temperature at $E_x < 10$ MeV [25]. Hence the density of levels of all J^π in this E_x region can be defined by:

$$\rho(E_x) = \frac{1}{T} e^{\frac{E_x - E_0}{T}} \tag{2.32}$$

where T and E_0 are the nuclear temperature and the energy-shift parameter, respectively. These two parameters can be calculated according to Ref. [26]:

$$E_0 = -1.004 + 0.5Pa' \tag{2.33}$$

and

$$T = \frac{1}{A^{\frac{2}{3}}(0.0597 + 0.00198S')} \tag{2.34}$$

$$S' = S + 0.5Pa'. \tag{2.35}$$

The values of Pa' and shell correction, S, can be obtained from Ref [26].

2.2.3 Overview of HFB + Combinatorial Model

The Hartree-Fock-Bogoliubov (HFB) + Combinatorial Model is a microscopic combinatorial approach that is used to calculate an energy-, spin- and parity-dependent nuclear level density [11]. It is implemented in the TALYS code [8] where the level density as function of spin, for several stable and unstable nuclei, are tabulated up to excitation energy of 200 MeV. The name HFB + Combinatorial model is derived from the fact that this Combinatorial approach is based on the nuclear structure properties obtained within the Hartree-Fock-Bogoliubov model. It uses the HFB single particle level scheme to compute incoherent particle-hole (ph) state densities, $\rho_{ph}(E_x, M, \pi)$, as a function of E_x, spin projection M on the intrinsic symmetry axis of the nucleus, and the parity π. Once the incoherent state densities have been determined, the collective effects such as rotational and vibrational enhancement and the disappearance

of deformation effects at high E_x are accounted for. The detailed discussion of this method can be obtained from Refs. [11, 27].

To estimate $\rho(E_x)$ the following basic nuclear structure properties must be known: single-particle energies, ε_i^k, pairing strength, δ_i^k, for each level, quadrupole deformation, β_2, and deformation energy, E_{def} [11, 27]. These parameters can be derived from HFB calculations using a given effective nucleon-nucleus interaction. It is also important to note that the s-wave spacings at S_n are too pairing-dependent and the poor description of pairing interactions in the HFB calculation may cause large discrepancies in $\rho(E_x)$ predictions. Therefore, to obtain reliable and accurate estimates the interaction field must be properly considered.

This model has also been recently compared [11] with experimental data, in particular to the s- and p-wave neutron resonance spacing obtained from Ref. [20]. The ratios of the theoretical resonance spacing, D_{th}, calculated with HFB + Combinatorial to the experimental s- and p-wave resonance spacing, D_{exp}, are displayed in figure 2.10. This comparison shows that generally resonance spacing are predicted within a factor of 2.

Further, the predicted number of levels is compared with experimental data of light, medium and heavy mass nuclei. As shown in figure 2.11 it gives satisfactory agreement at low E_x. However, it was pointed out that for accurate and reliable estimations of cross-sections and many other nuclear physics applications, the $\rho(E_x)$ calculated with this model has to be renormalized to both the experimental levels at low E_x and neutron resonance spacing at S_n according to Ref. [11]

$$\rho(E_x, J^\pi)_{renorm} = e^{\beta\sqrt{E_x-\delta}} \times \rho(E_x - \delta, J^\pi), \tag{2.36}$$

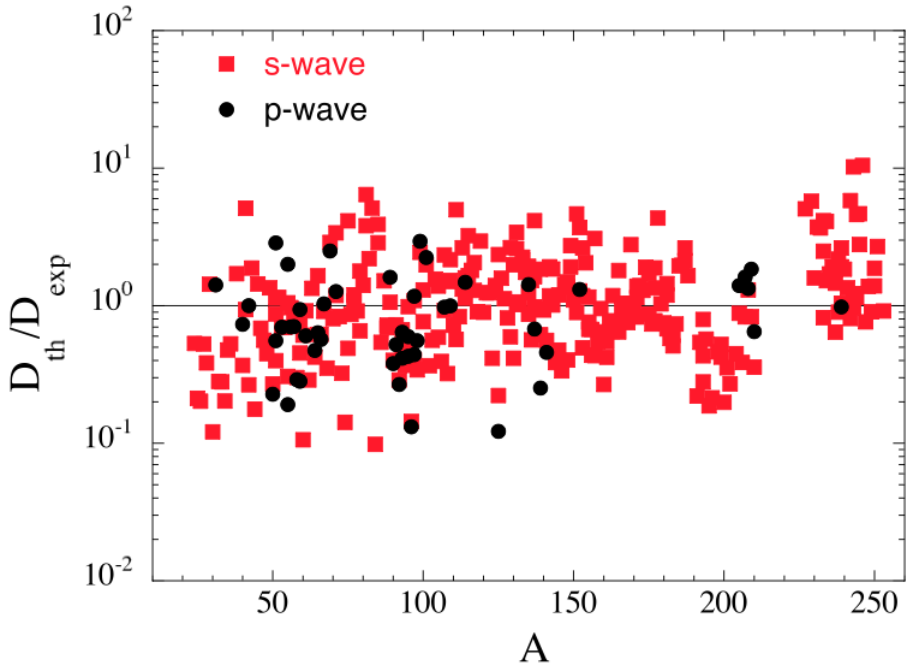

Figure 2.10: Comparison of HFB + Combinatorial Model with experimental s- and p-wave resonance spacings [11].

where the energy shift δ is extracted from the analysis of the cumulative number of levels and β from the experimental s-wave neutron resonance spacing. These values are tabulated in Ref. [11] for the mass regions $A = 24$ to 204. Additionally, in the HFB + Combinatorial Model $\rho(E_x)$ can be used to calculate the reaction cross-sections within the Hauser-Feshbach formalism in the TALYS program [8]. For instance, this procedure has been used to calculate the $^{89}\mathrm{Y}(n,\gamma)^{90}\mathrm{Y}$ cross-section which compares well to the experimental cross-section (see figure 2.12) [11]. These results show that the HFB + Combinatorial calculated $\rho(E_x)$ reproduces the experimental data better after it has been renormalized.

2.3 Radiative Strength Function

The radiative strength function, $f_{XL}(E_\gamma)$, is a distribution of average reduced widths for transitions of a given multipole type XL between states of energies

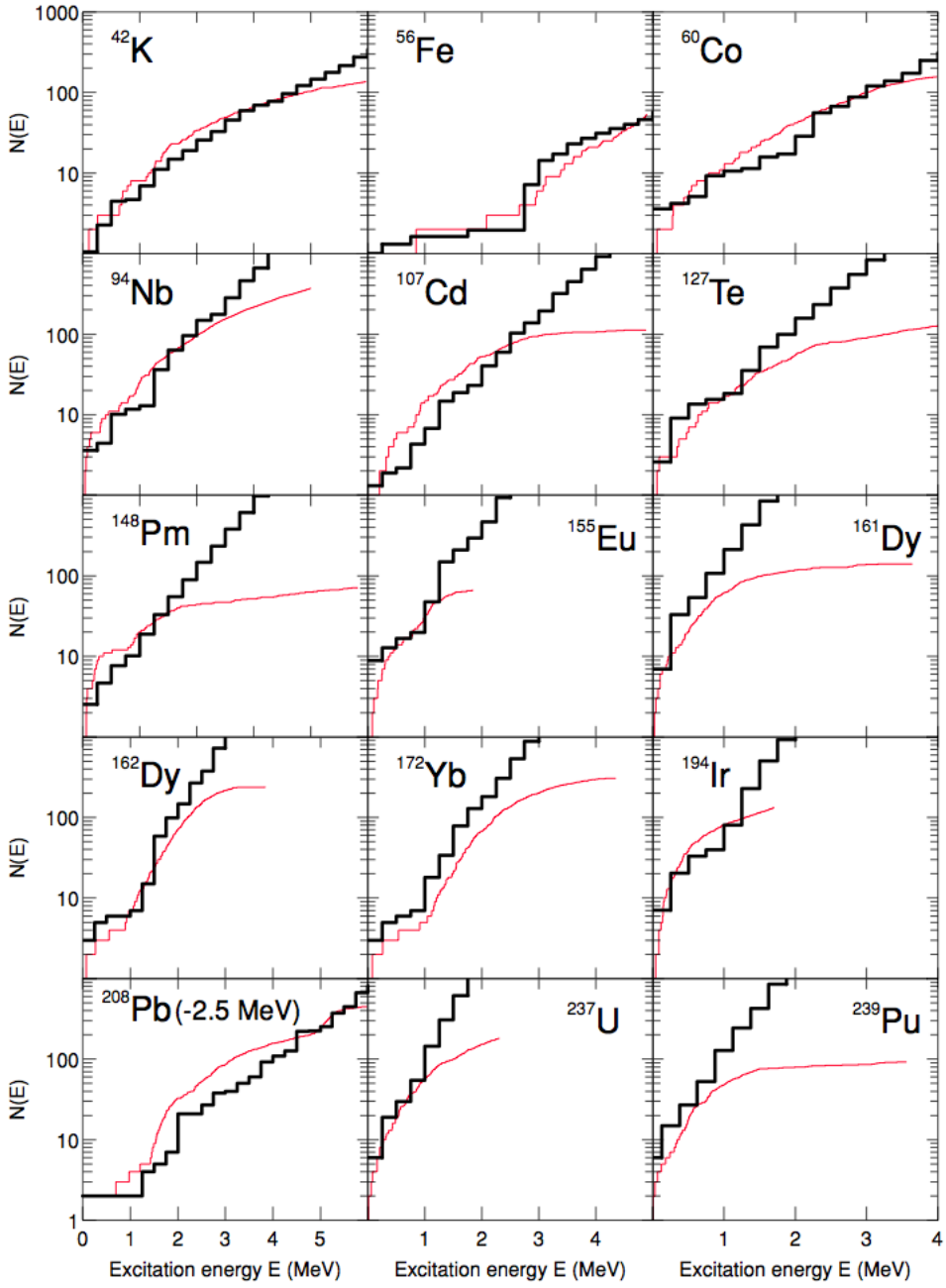

Figure 2.11: Cumulative number of observed levels (red line) and HFB + Combinatorial Model calculations (black line) as a function of E_x [11].

E_i and E_f, as a function of $E_\gamma = E_i - E_f$ where $E_i > E_f$ [28]. The transition between E_i and E_f can occur in two ways. These are the photoabsorption from a low energy state (which is normally the ground state) to a range of excited states, and decay from an interval of excited states to a range of lower energy

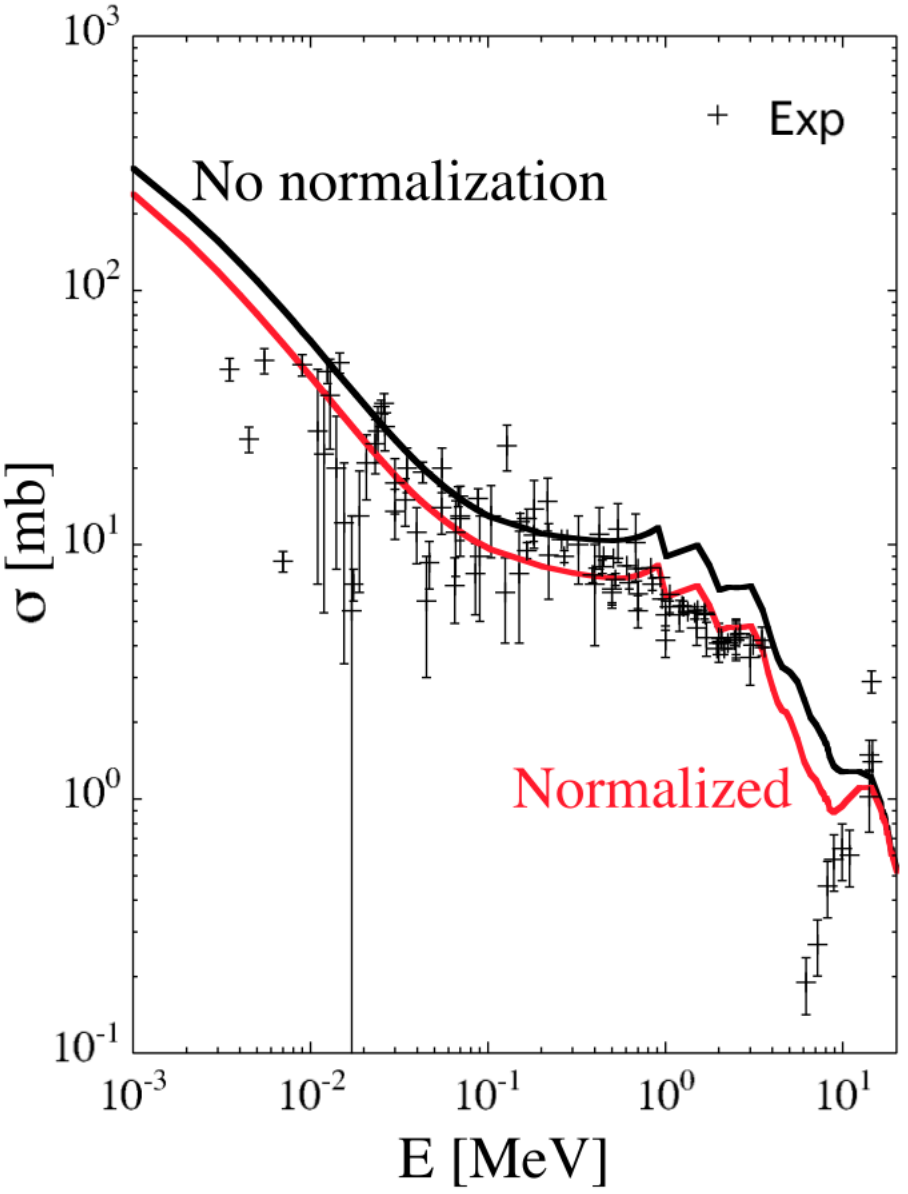

Figure 2.12: cross-section of the $^{89}\mathrm{Y}(n,\gamma)^{90}\mathrm{Y}$ reaction obtained with (red line) and without (black line) normalization of $\rho(E_x)$ compared to experimental data [11].

states. Hence $f^J_{ifXL}(E_\gamma)\uparrow$ and $f^J_{ifXL}(E_\gamma)\downarrow$ can be used to differentiate between the strength functions for photoexcitation and γ ray decay, respectively. However, the focus of this research is restricted to $f^J_{ifXL}(E_\gamma)\downarrow$. Therefore $f^J_{ifXL}(E_\gamma)$ will be used instead of $f^J_{ifXL}(E_\gamma)\downarrow$ and only the strength function corresponding to γ ray decay will be discussed.

The strength function for decay of excited states with spin J within a unit energy interval at fixed E_i to a lower energy state at E_f, by emitting a γ ray of multipole XL and energy E_γ is defined as [28]

$$f^J_{ifXL}(E_\gamma) = \frac{\rho_{J^\pi}(E_i)\bar{\Gamma}^J_{\gamma ifXL}}{E^{2L+1}_\gamma}, \tag{2.37}$$

where $\bar{\Gamma}^J_{\gamma ifXL}$ is the average partial radiative width for transitions between level i of spin J and state f, and $\rho_J(E_i)$ is the level density of spin J states at excitation E_i. The average $\bar{\Gamma}^J_{\gamma ifXL}$ is taken over a larger number of levels of the same spin and parity at E_i.

There are various types of theoretical models that can be used to describe $f^J_{ifXL}(E_\gamma)$ for γ rays of a given multipole type resulting from a given mode of excitation. These will be referred to as Resonance Models and are briefly discussed below together with their corresponding modes of excitation. For simplicity $f(E_\gamma)$ will be used instead of $f^J_{ifXL}(E_\gamma)$ in the remainder of this thesis.

2.4 Resonances of the Radiative Strength Function

Before discussing the Resonance Models it is important to review various resonances that are usually observed as part of the total strength function, because the models are based on these resonances.

2.4.1 Giant Electric Dipole Resonance

The giant electric dipole resonance (GEDR) results from the isovector, $\Delta T = 1$, collective mode of nuclear excitation with high frequency and small ampli-

tude [29]. In this mode the protons and neutrons vibrate out of phase as it is illustrated in figure 2.13. This is a very broad resonance with a width of 2 - 7 MeV and located at high mean energies of 14 -22 MeV depending on the mass of the nucleus [30]. It is due to the extra energy required to separate the proton and neutron distributions.

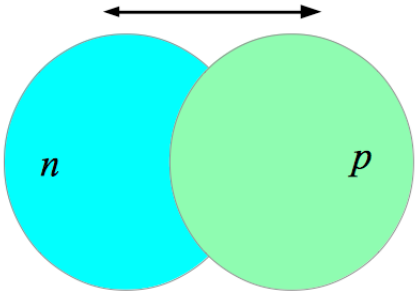

Figure 2.13: The GEDR nuclear excitation modes.

2.4.2 The Giant Magnetic Dipole Resonance

The Giant Magnetic Dipole Resonance (GMDR) is due to the spin-flip collective excitation which is divided into two modes of excitation namely, isoscalar and isovector modes [29]. In the isoscalar mode nucleons with spin ↑ oscillate against those with spin ↓. In the isovector mode protons with spin ↑ oscillate against neutrons with spin ↓ and vice versa (see the illustration in figure 2.14).

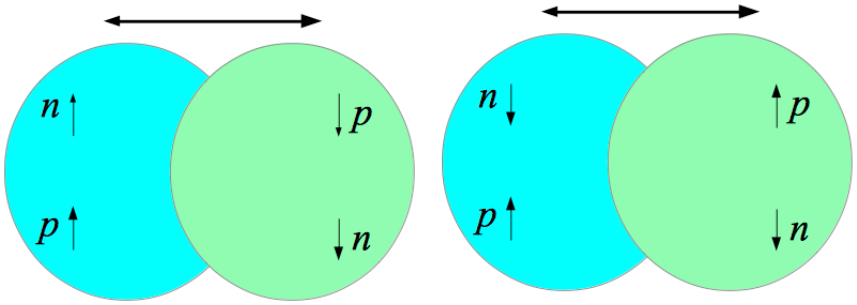

Figure 2.14: The isoscalar (left panel) and isovector (right panel) spin-flip modes of nuclear excitation.

2.4.3 Pygmy Resonance

In addition to the GEDR resonance there is another E1 resonance which is located at noticeably lower energies compared to the GEDR [31]. This is called the pygmy resonance and is observed only in nuclei with neutron excess. It has been explained to be due to the oscillation of the neutron skin against a symmetric proton-neutron core with isospin $T = 0$ (see figure 2.15 for illustration). However, it is not clear yet if this experimentally observed resonance is due to this kind of collective excitation or single-particle effects. It is still impossible with available experimental techniques to comprehensively study the nature of pygmy resonances. Therefore, the origin of this low energy E1 resonance is still subject of theoretical modelling. A recent review of the pygmy resonance can be found in Ref. [32].

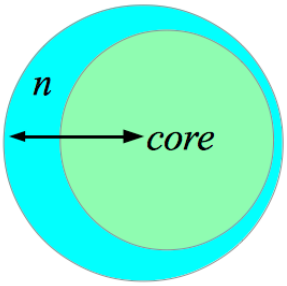

Figure 2.15: Pygmy dipole collective excitation.

2.4.4 Scissors Resonance

The Scissors resonance is a M1 collective excitation that is located at low energies around 3 MeV and is only observed in deformed nuclei [33]. In this collective excitation the protons and neutrons, and hence their angular momenta, oscillate against each other following a similar movement as a pair of scissors. This is illustrated in figure 2.16 below.

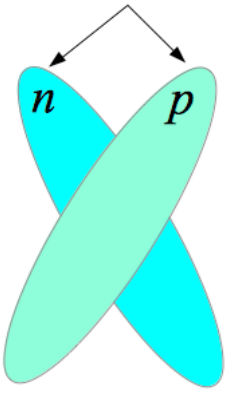

Figure 2.16: Scissors modes.

2.4.5 Resonance Models for E1 Resonance

The original Brink approach suggests that the GEDR can be described using the standard Lorentzian (SLO) function with an energy and temperature independent width [34]:

$$f_{E1}^{SLO} = 8.68X10^{-8}\frac{\sigma_0 E_\gamma \Gamma_0^2}{(E_\gamma^2 - E_0^2)^2 + E_\gamma^2\Gamma_0^2} \tag{2.38}$$

where the Lorentzian parameters σ_0, Γ_0^2 and E_0^2 are the peak cross-section, GEDR width and centroid energy, respectively. This description of the GEDR overestimates the experimental strength function at and below S_n. Hence the Lorentzian (LO) function with the energy dependent width, $\Gamma(E_\gamma)$, was proposed and is written as [34]

$$f_{E1}^{LO} = 8.68X10^{-8}\frac{\sigma_0 E_\gamma \Gamma_0 \Gamma(E_\gamma)}{(E_\gamma^2 - E_0^2)^2 + E_\gamma^2\Gamma_0^2}. \tag{2.39}$$

The dependence of $\Gamma(E_\gamma)$ on E_γ is due to spreading of particle-hole states into two hole and two particle states. In addition to the E_γ dependence, the temperature dependence of the width was introduced and is given by [34]:

$$\Gamma(E_\gamma, T) = \Gamma_0 \frac{E_\gamma^2 + 4\pi^2 T^2}{E_0^2}. \tag{2.40}$$

The nuclear temperature, $T = \sqrt{\left(\frac{S_n - E_\gamma}{a}\right)}$, where S_n and a are the neutron separation energy and the BSFG level density parameter respectively, accounts for the temperature of a state on which the GEDR is built.

Although the LO function was improved by including the temperature and γ ray energy dependent width, it was still failing to describe the electric dipole operator in the limit of zero E_γ [34]. Hence the generalized Lorentzian (GLO) function, which overcomes this problem, was proposed and reads as:

$$f_{E1}^{GLO} = 8.68X10^{-8}\sigma_0\Gamma_0 \left[\frac{E_\gamma \Gamma(E_\gamma, T)}{(E_\gamma^2 - E_0^2)^2 + E_\gamma^2\Gamma_0^2} + 0.7\frac{\Gamma(E_\gamma = 0, T)}{E_0^3}\right]. \tag{2.41}$$

The GLO reproduces the experimental $f(E_\gamma)$ reasonably well for target nuclei in the mass region of $A \sim 55 - 197$. However, it underestimates the experimental $f(E_\gamma)$ for strongly deformed nuclei in the mass region $A \sim 150 - 175$ by up to a factor of 4 [35]. The enhanced generalized Lorentzian (EGLO) is therefore used to describe the GEDR of deformed nuclei in the mass region of $A \sim 150 - 175$, since it reproduces the experimental data.

The only difference between the EGLO and GLO functions is that the width of the GEDR in the EGLO function is enhanced. This width is given by the following empirical equation [35]:

$$\Gamma(E_\gamma, T) = k_0 + (1 - k_0)\left(\frac{E_\gamma - \epsilon_0}{E_0 - \epsilon_0}\right)\frac{\Gamma_0}{E_0^2}(E_\gamma^2 + 4\pi^2 T^2) \tag{2.42}$$

where the enhancement k_0 is a purely empirical expression which depends on the mass of the target nucleus. For the constant $\epsilon_0 = 4.5$ MeV, k_0 is 1 for $A < 148$ and $1 + 0.09(A - 148)^2 e^{(-0.180(A-148))}$ for $A \geq 148$.

2.4.6 Resonance Model for M1 Resonance

The strength function of a spin-flip resonance is described using the SLO, that is equation (2.38), with a temperature and energy independent width. The Lorentzian parameters in this case are $\Gamma_0 = 4$ MeV, $E_0 = 41A^{-\frac{1}{3}}$ and σ_0 is adjusted to $f_{E1}/f_{M1} = 0.0588A^{0.878}$ [20].

2.5 Low-Energy Enhancement

In addition to the GEDR, GMDR, pygmy and scissors resonances there is a low-energy enhancement (up-bend) in $f(E_\gamma)$. This feature has been observed in the medium mass nuclei such as (^{44,45}Sc [22], ^{50,51}V [36], ^{44,45,46}Ti [37, 38, 39], ^{56,57}Fe [40, 41], $^{93-98}$Mo [42]), using the Oslo Method. This is illustrated in figure 2.17. It should also be emphasized that this up-bend does not imply the use of an inappropriate slope of $f(E_\gamma)$, which is verified by comparing the measured strength function to photo-neutron data, obtained from the literature. This comparison is illustrated in figures 2.17 and 2.18. Clearly the $f(E_\gamma)$ of ^{56}Fe and $^{116-119}$Sn show a good agreement with the tail of the GEDR in the respective figures. Refs. [43, 23] argued that there is a possibility that the low-energy enhancement is only found in the mass region $A \leq 106$ (see figures 2.18 and 2.19).

This low-energy enhancement generally provoked debates about whether it is a real feature or if it is due to systematic errors in the Oslo Method. However, its existence has been recently confirmed by Ref. [44] using a completely different experimental setup and analysis technique which, unlike the Olso Method,

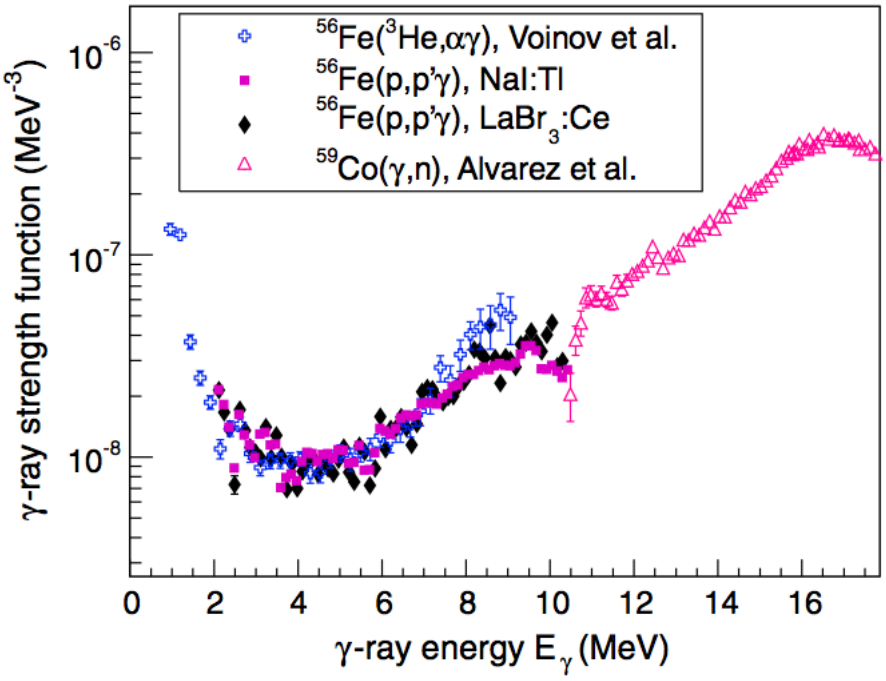

Figure 2.17: Radiative strength functions of ^{56}Fe obtained using (^{3}He, $\alpha\gamma$) and (p, $p\gamma$) reactions and compared with the GEDR data [41].

is model-independent and is based on particle-γ-γ coincidence measurements. These measurements were performed at the 88-Inch cyclotron of the Lawrence Berkeley National Laboratory, and the excited ^{95}Mo isotopes were produced through ^{94}Mo$(d, p\gamma)$ ^{95}Mo reaction with a beam energy of 11 MeV.

In this method the $f(E_\gamma)$ can be extracted for statistical γ rays deexciting a compound nucleus to well resolved discrete states of same J^π. In the experimental data of Ref. [44] 3 pairs of discrete levels with respective $J^\pi = \frac{1}{2}^+, \frac{7}{2}^+$ and $\frac{9}{2}^+$ and seven discrete states with $J^\pi = \frac{3}{2}^+$ were utilized to extract $f(E_\gamma)$ of the primary transitions deexciting the nucleus from excitation energies of 3, 4, 5, 6 and 7 MeV. The results are shown in figure 2.20. They were also compared to data obtained using the Oslo Method in (^{3}He, α) reaction [42]. The solid curve is a quadratic fit to $f(E_\gamma)$ of Ref. [42] while the dotted curves give the lower and upper error limits to the fit. The absolute normalization of the Ref. [44] results were obtained using χ^2 minimizations between the quadratic

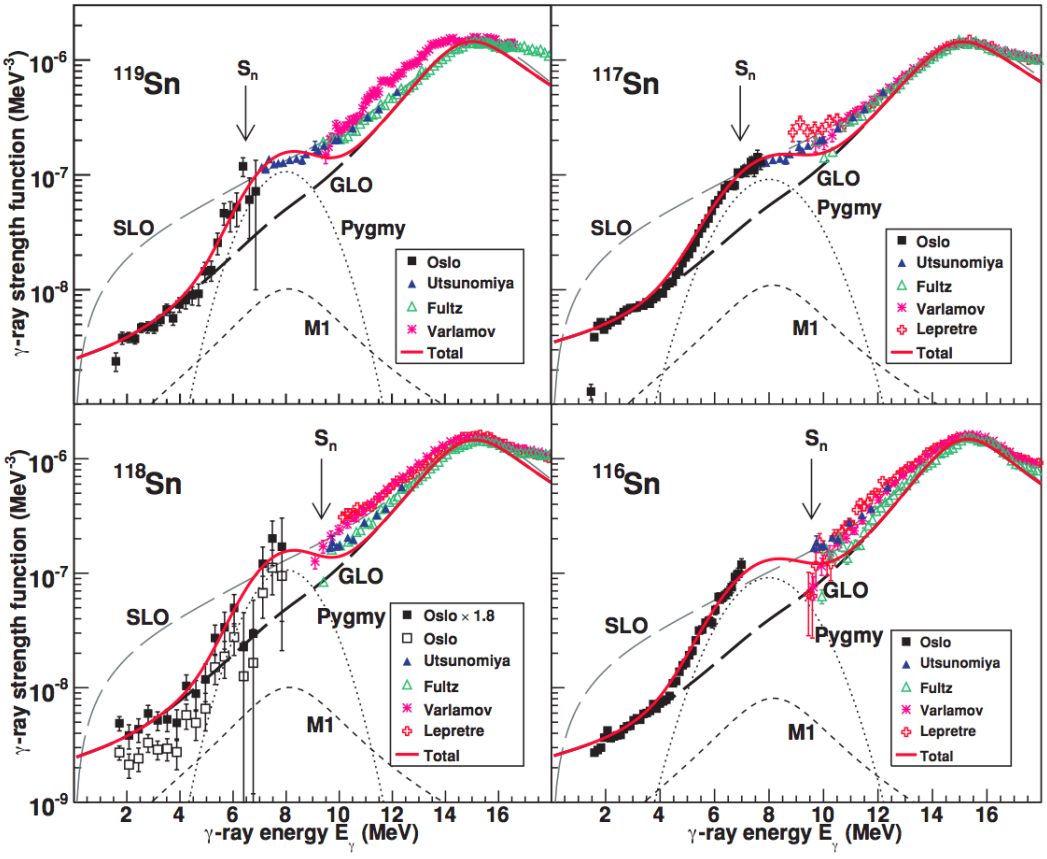

Figure 2.18: Radiative strength functions of $^{116-119}$Sn obtained using (^{3}He, $\alpha\gamma$) and (^{3}He, ^{3}Heγ) reactions and compared with GEDR photo-neutron data [23].

fit and the $f(E_\gamma)$ for each E_i.

The physical origin of this new feature of the radiative strength function has been a mystery for many years and is still a subject of interest in theoretical nuclear physics. So far there have been two attempts [45, 46] that yield different explanations for the origin of the low-energy enhancement. The first theoretical work predicts that it is due to $M1$ transitions generated by the reorientation of the spins of high-j neutron and proton orbits [45]. This was accomplished using shell model calculations of $M1$ transition strengths in $^{94-96}$Mo which reproduced the up-bend [45]. Some of the results from these calculations are shown in figure 2.21. The (γ, n) and (^{3}He, ^{3}He') data were taken from Refs. [42, 47] and the $E1$ strength is f^{EGLO} fitted on the experimental data. Due

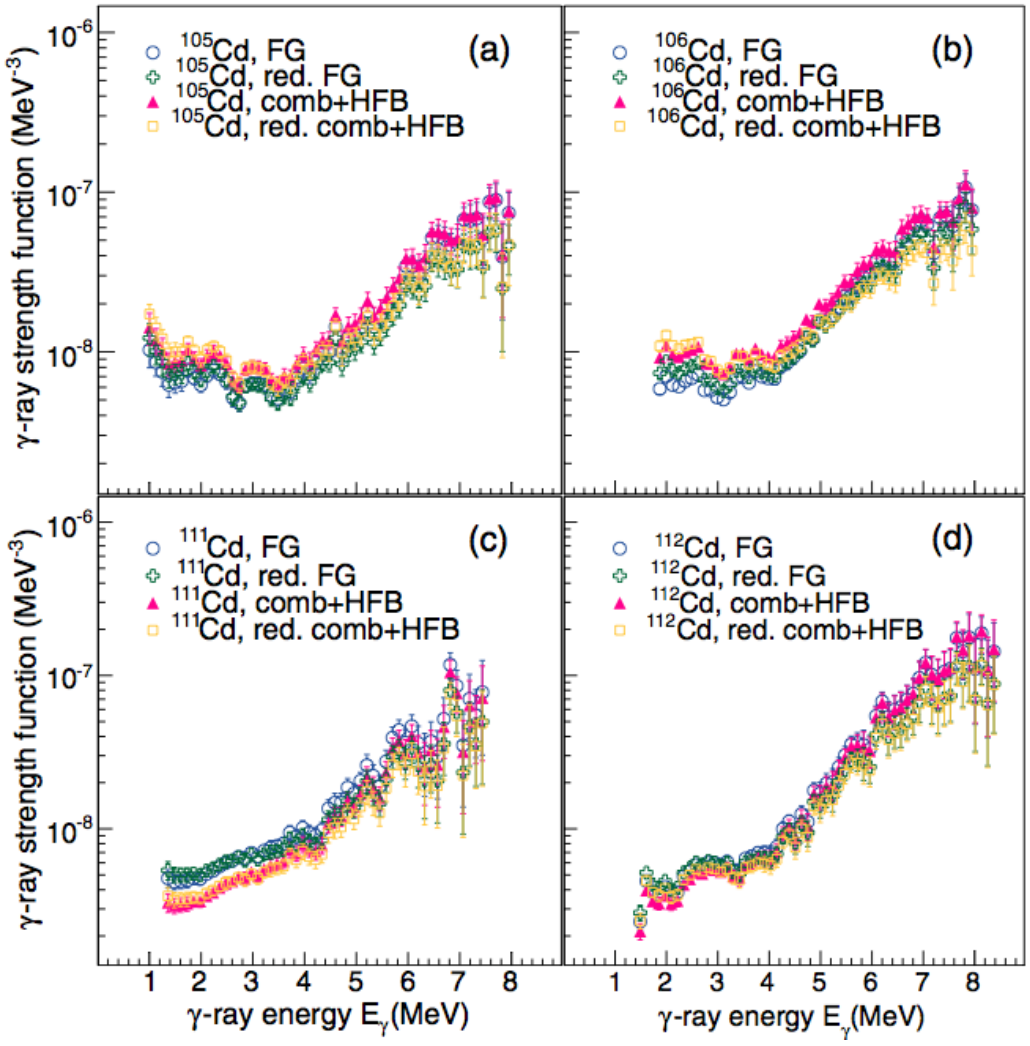

Figure 2.19: Radiative strength functions of Cd isotopes obtained using (^{3}He, $\alpha\gamma$) and (^{3}He, ^{3}Heγ) reactions [43].

to the limitation of the shell model this approach cannot be used to verify the observed absence of the low-energy enhancement in heavier systems.

The second theoretical approach [46] predicts that the up-bend is due to transitions from the single-particle quasicontinuum to continuum states, which occurs at nuclear temperatures of the order of MeV resulting in $E1$ transitions. The $E1$ radiative strength function was calculated within the thermal continuum quasiparticle random phase approximation (TCQRPA) at finite temperatures, and compared to experimental data from Refs. [23, 42, 48, 49].

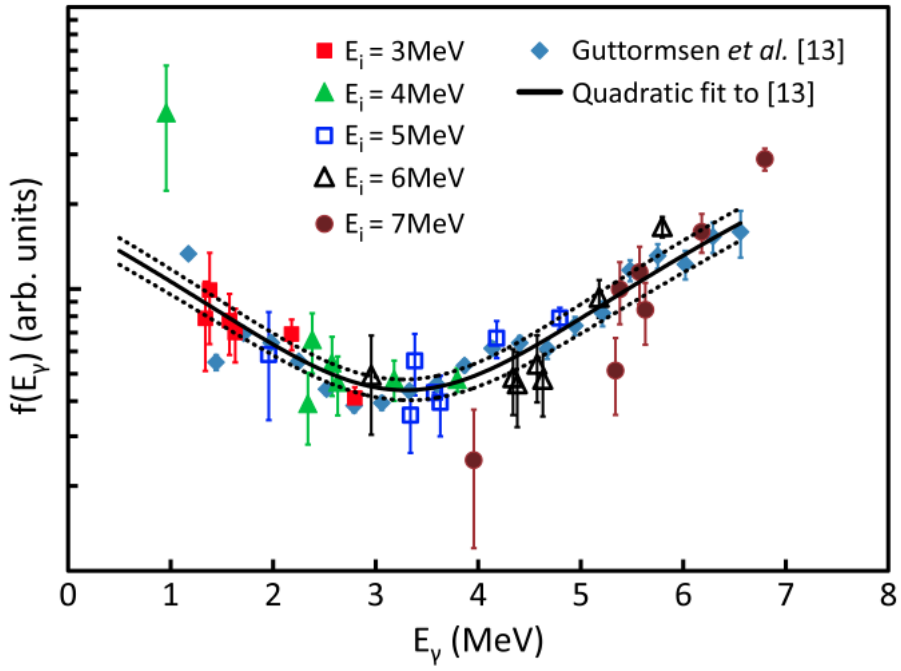

Figure 2.20: Comparison between the ^{95}Mo radiative strength function of Refs. [42, 44].

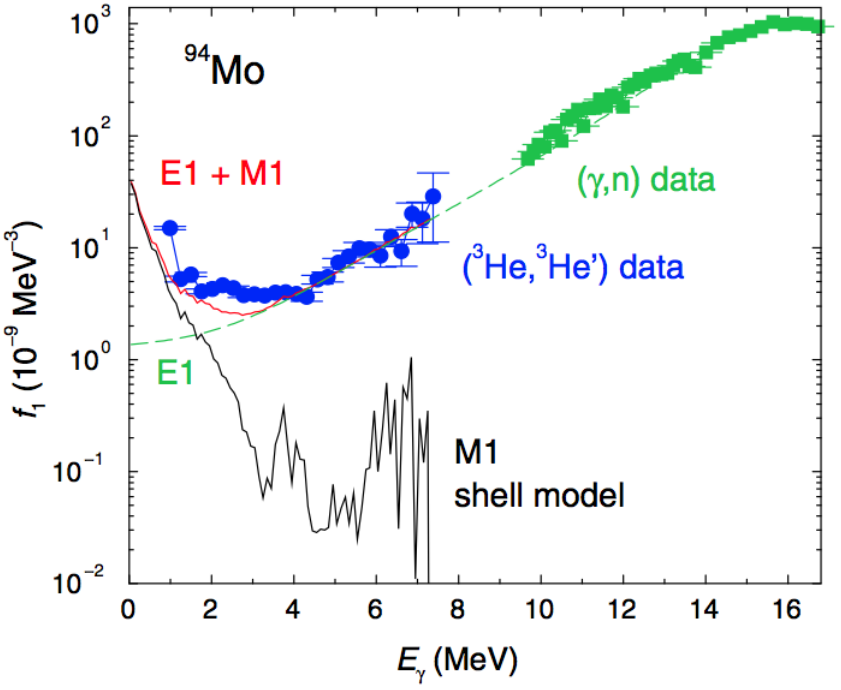

Figure 2.21: Experimental and theoretical radiative strength function of ^{94}Mo [45].

In contrast to the shell model calculation, this theoretical approach can be used even in heavier mass regions. Thus, it does not only reproduce the low-energy enhancement of Mo isotopes but also its absence in heavier isotopes. This is illustrated in figures 2.22 and 2.23.

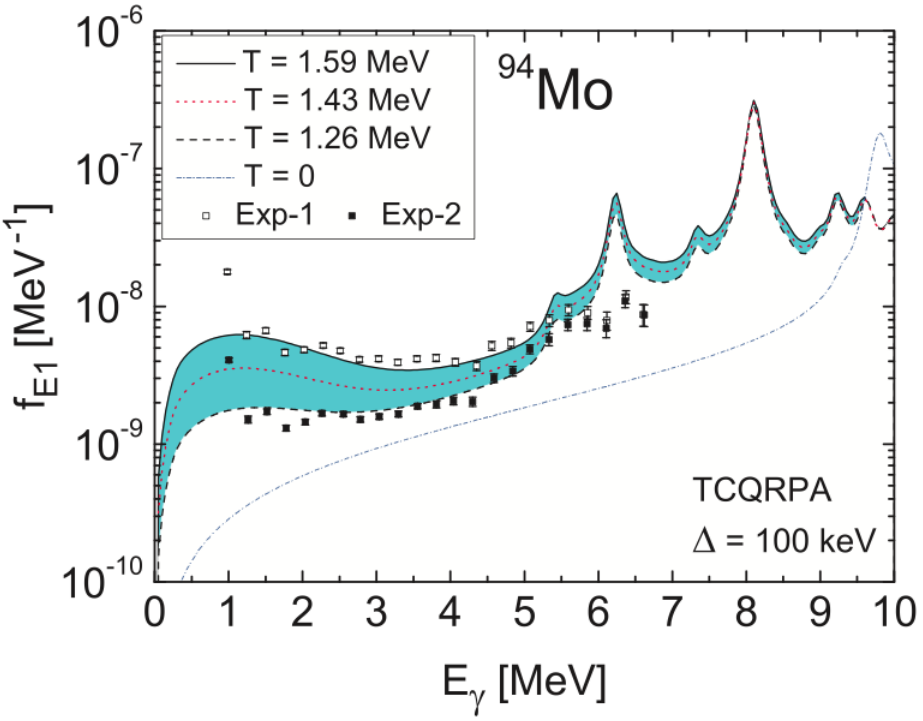

Figure 2.22: The theoretical radiative strength function of ^{94}Mo compared with experimental data [46].

Although the theoretical approaches predict different mechanisms for the origin of the low-energy enhancement, they both suggest that it is of dipole nature. However, this does not rule out the possibility of having strong collective transitions, such as vibrational ($E3$) or rotational ($E2$) transitions in the quasicontinuum, causing an enhancement of the $f(E_\gamma)$ at low energies. A recent work [41] suggests the up-bend to be predominantly dipole in nature. To reach this conclusion an experiment using the ^{56}Fe(p, $p\gamma$)^{56}Fe reaction was performed at the Oslo cyclotron laboratory. The primary γ ray matrices were extracted from p-γ coincidence events for the γ ray detection angular range of

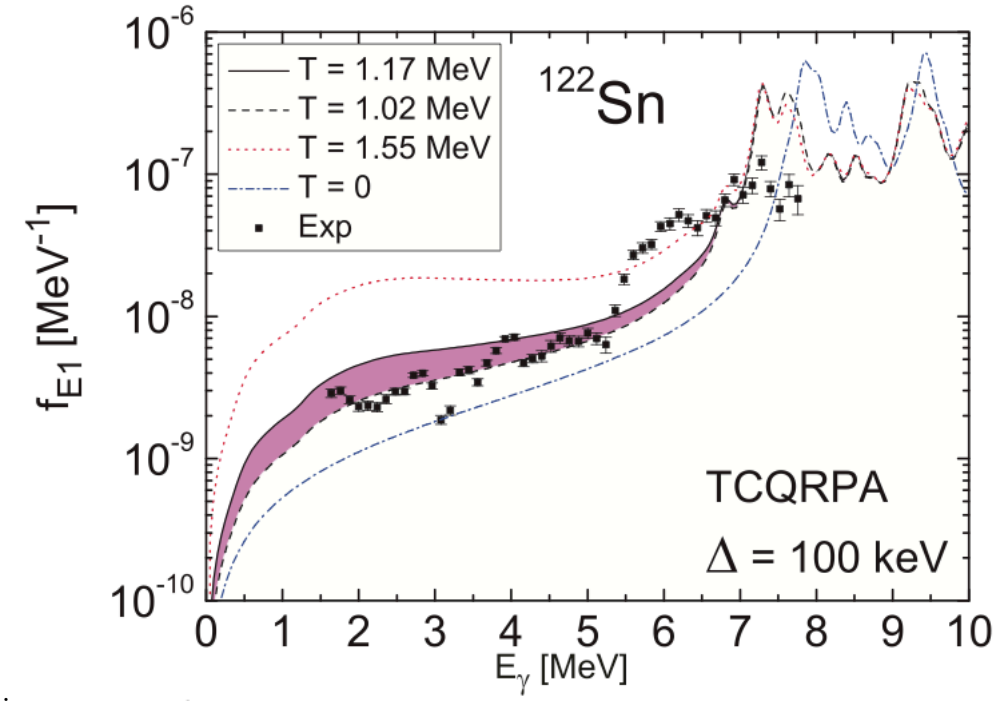

Figure 2.23: The theoretical radiative strength function of ^{122}Sn compared with experimental data [46].

$\theta_{lab} = 37.4 - 142.6°$. These matrices were gated in the narrow energy region $E_\gamma = 2.5 - 2.7$ MeV and $E_x = 7.4 - 7.9$ MeV where the low-energy enhancement is observed. Thus the intensity of γ ray transitions in this region was plotted as a function of angle (see figure 2.24). This angular distribution of the intensity was fitted with angular distribution functions of the form [41]

$$W(\theta) = A_0 + A_2 P_2(cos\theta) + A_4 P_4(cos\theta), \tag{2.43}$$

where $P_k(cos\theta)$ is a Legendre polynomial of degree k.

In figure 2.24 this theoretical fit is shown with the blue line assuming pure dipole transitions confirming the dipole nature of the low-energy enhancement.

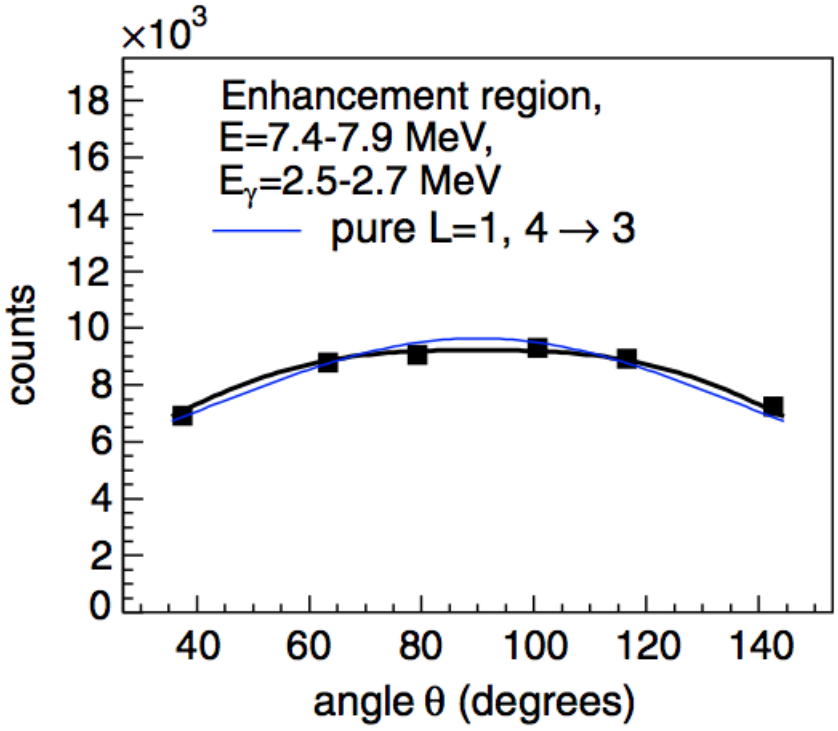

Figure 2.24: Angular distribution of the primary γ ray matrix gated in the energy region corresponding to the up-bend [41].

2.5.1 Impact of the Low-Energy Enhancement on Astrophysical Reaction Rates

An interesting feature of the up-bend in the $f(E_\gamma)$ is its significant impact on astrophysical reaction rates, especially on the neutron-rich isotopes. This has been demonstrated by the Maxwellian-average neutron capture, (n, γ), rates $\langle \sigma \mathrm{v} \rangle$, for entire isotopic chains of Mo, Fe and Cd up to the neutron drip line [48] at $T = 10^9$ K, the temperature at which r-process nucleosynthesis takes place. These predictions suggest that the influence of the low-energy enhancement becomes more significant as the neutron number increases, and can increase the r-process reaction rates up to 2 orders of magnitude (see figures 2.25 and 2.26). This is due to the exponential increase in the level density as function of excitation energy, leading to a greater role in the significance of the up-bend portion of the $f(E_\gamma)$ linking the capture states to the high level density near

the neutron separation energy.

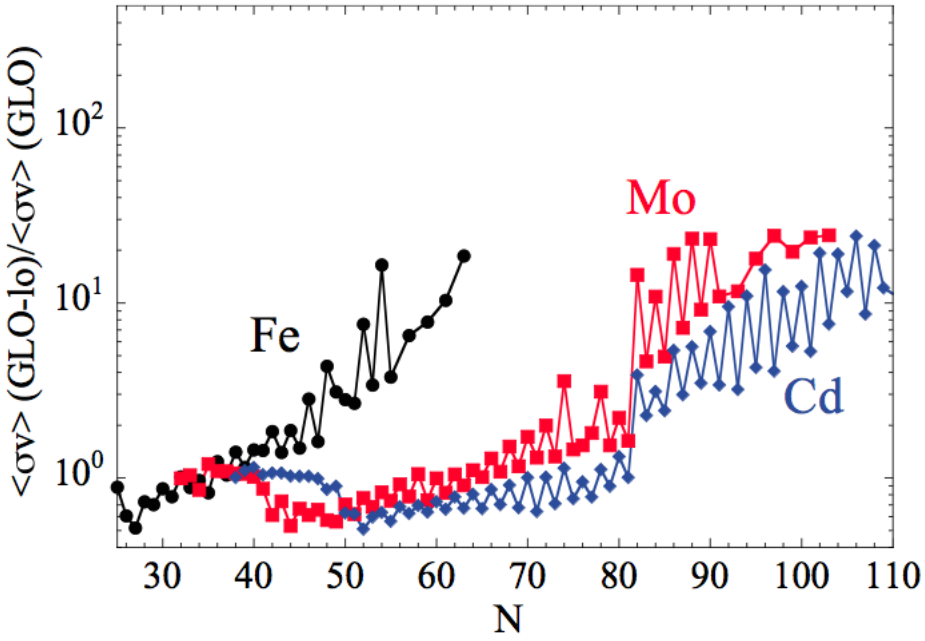

Figure 2.25: Maxwellian-average reaction rates when the low-energy enhancement is not included [48].

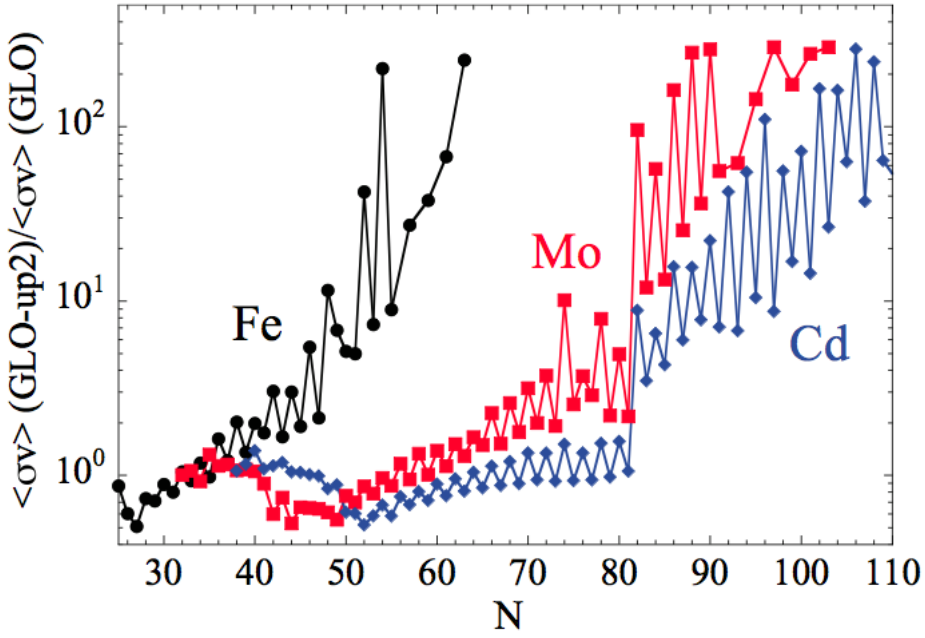

Figure 2.26: Maxwellian-average reaction rates with the low-energy enhancement included [48].

2.5.2 Impact of the Pygmy Resonance on Nucleosynthesis

In addition to the low-energy enhancement, the effect of the $E1$ pygmy resonance on r-process nucleosynthesis has been investigated [50]. This was performed using the non-equilibrium canonical model [51] in which a full reaction network is solved for a given set of parameters. These are neutron density in an astrophysical site, N_n, its temperature, T, and the period of the neutron irradiation, τ_{irr}. Figure 2.27 illustrates the predicted r-abundance with and without the pygmy resonance at $T = 10^9$ K, $N_n = 10^{20}$ cm^{-3} and $\tau_{irr} = 2.4$ s. It can be seen from figure 2.27 that the consideration of only the giant dipole resonance (blue curve) mostly produces the nuclei in the mass region $A \approx 90$ - 110. As soon as the pygmy is included the predicted r-abundance decreases by up to 2 orders of magnitude in this mass region, and is enhanced by up to the same order of magnitude in the $A \approx 130$ mass region (green curve). Clearly the pygmy resonance has a significant impact on r-process nucleosynthesis.

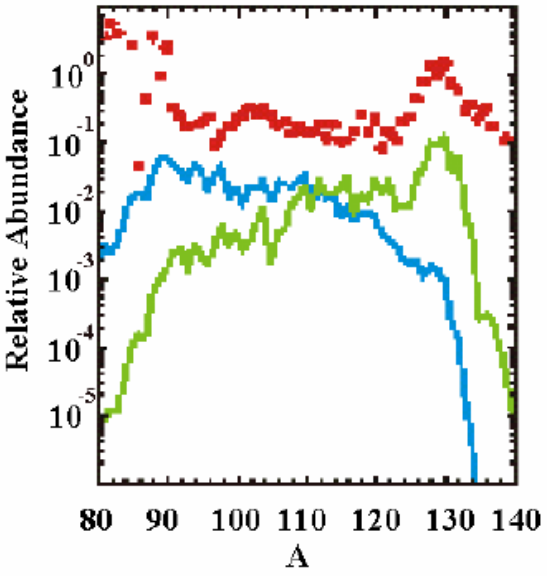

Figure 2.27: r-abundance distributions (blue and green curves). The red curve is the solar abundance distribution. [52].

2.6 Astrophysical Reaction Rates and p-Abundance Calculations

The astrophysical reaction (such as (n,γ)) rates are calculated, using the statistical emission model Hauser-Feshbach (HF) which is implemented in the TALYS reaction code [8, 53]. Basically, TALYS is a publicly available computer program which is used to simulate nuclear reactions that involve γ rays, neutrons, protons, deuteron, tritons, helions, and α particles, in the energy range of 1 keV - 200 MeV. The HF Model takes into account that 1) in the stellar interior the compound nucleus (CN) can be formed in different states with different J^{π}, and 2) the formation of the CN is possible only if the nuclear level density in the CN, at E_x corresponding the projectile incident energy, is sufficiently high. It therefore allows for the calculation of the capture reaction cross-sections, σ^{E_x}, for a CN produced in states with specific E_x and J^{π} according to

$$\sigma^{E_x} = D^{comp}\pi\lambda^2 \sum_{J,\Pi} \frac{(2J+1)}{(2s+1)(2I^{\mu}+1)} \times \sum_{j,l,j',l'} \delta(\alpha)\delta(\alpha') \times \frac{\langle T^J_{\alpha lj}(E_a)\rangle \langle T^J_{\alpha' l' j'}(E_{a'})\rangle}{\sum_{\alpha'',l'',j''} \delta_{\pi}(\alpha'')\langle T^J_{\alpha'' l'' j''}(E_{a''})\rangle} W^J_{\alpha lj\alpha' l' j'} \tag{2.44}$$

where j, l, s, π, E_a represent the projectile angular and orbital momentum, spin, parity and energy. The variables with a prime correspond to the ejectile. The symbols J and Π are the spin and parity of a compound system. In this equation λ is the relative motion wave length, T the transmission coefficient, W the width fluctuation correction factor and D^{comp} the depletion factor which is calculated according to Ref. [53]. The function $\delta_{\pi}(\alpha)$ is unity if $(-1)^l \pi \Pi^{\mu} = \Pi$, and zero otherwise. The quantities I^{μ} and Π^{μ} are the spin and parity of a target nucleus, while all those with double prime correspond to the decay of

the residual nucleus to lower energy states.

The calculation of the transmission coefficient requires the following parameters which are therefore ingredients for the HF approach: the ground- and excited-state properties (masses, deformation, matter densities, excited state E_x and J^π), nuclear level density, radiative strength function, optical model potential and fission properties. Further, in the stellar interior the thermodynamic equilibrium holds locally to a good approximation. Hence, the energies of target nuclei and projectiles, as well as their relative energies, obey a Maxwell-Boltzmann distribution of energies corresponding to a temperature, T, at that location. Therefore the astrophysical reaction rates, $\langle \sigma v \rangle$, are obtained by integrating σ^{E_x} over the Maxwell-Boltzmann distribution at a given T according to Ref. [53]. According to the detailed balance theorem, if a compound system ${}^{A}X_Z$ is formed through ${}^{A-1}X_Z + n \longrightarrow {}^{A}X_Z + \gamma$ and ${}^{A+1}X_Z + \gamma \longrightarrow {}^{A}X_Z + n$ then

$$|\langle \phi_{(A-1)n}|H|\phi_{(A)\gamma}\rangle|^2 = |\langle \phi_{(A+1)\gamma}|H|\phi_{(A)n}\rangle|^2, \tag{2.45}$$

where $|\langle \phi_{(A-1)n}|H|\phi_{(A)\gamma}\rangle|$ and $|\langle \phi_{(A+1)\gamma}|H|\phi_{(A)n}\rangle|$ are the transition matrix elements for the first and second reactions, respectively. This implies that the (n,γ) cross-section will be equal to the (γ,n) cross-section [54].

The synthesis of p-nuclei can be investigated using the parametrized explosion model [3, 55]. This enables the calculation of p-abundances resulting from nuclear reactions taking place in the exploding of O/Ne-rich layers of Type II supernovae. The input parameters for this model are: temperature and density profile of O/Ne-rich layers, initial abundances of s-process seed nuclei and rates of all reactions involved in the reaction network. The reaction network involves 2500 stable and neutron deficient nuclei with $Z \leq 84$ [3]. These nuclei

are linked together by all possible reactions: (n,γ), (n,p), (n,α), (p,α), (p,γ), (α,γ) and their photodisintegrations: (γ,n), (γ,p) and (γ,α). In fact the rates of these reactions can be obtained using the HF approach as discussed above. The resulting abundance of each p-nucleus i produced through this nuclear reaction network is then represented by its mean overproduction factor

$$\langle F_i \rangle = \frac{\langle X_i \rangle}{X_{i,\odot}}, \tag{2.46}$$

where $X_{i,\odot}$ is its solar mass fraction and

$$\langle X_i \rangle = \frac{1}{M_p} \sum_{n \geq 1} \frac{(X_{i,n} + X_{i,n-1})(M_n - M_{n-1})}{2}, \tag{2.47}$$

where $X_{i,n}$ is the mass fraction of isotope i at mass coordinate M_n, and M_p is the total mass of all O/Ne-rich layers. The comparison of the computed abundance with the solar abundance is achieved using the ratio $\frac{\langle F_i \rangle}{F_0}$ where $F_0 = \frac{1}{35} \sum_i \langle F_i \rangle$ is the measure of global p-nuclei enrichment in the p-process layers. This ratio would be unity for all i if the calculated abundances were exactly solar. Furthermore it has been shown in Ref. [3] that $\frac{\langle F_i \rangle}{F_0} \approx 1$ for ^{138}Ce which is one of the p-nuclei and neighbor to ^{138}La. Therefore, this comparison can be done using $\langle F_i \rangle / F$ (^{138}Ce) instead.

Chapter 3

Experimental Details

The ^{139}La(^{3}He, X), where X refers to ^{3}He and α particles, experiment was conducted at the Cyclotron Laboratory of the University of Oslo (OCL) for seven days. The target was manufactured at iThemba LABS (see section 3.5) with a thickness of 2.5 mg/cm^2. The beam energy and intensity were 38 MeV and $\approx$ 0.4 - 0.7 pnA, respectively. The particle-γ coincident events were detected using the SiRi and CACTUS arrays. The details of the Oslo cyclotron, SiRi and CACTUS arrays are given below. The additional experiment, ^{28}Si(^{3}He, X), was also conducted for calibration purposes.

3.1 Overview of the Oslo Cyclotron Laboratory

At OCL, a M-35 Scanditronix cyclotron delivers pulsed light-ion beams at the typical frequency of $\sim$ 15.3 MHz for 38 MeV ^{3}He ions. The schematic layout of the beam line in the laboratory is shown in figure 3.1. The beam from the cyclotron is collimated and focused using slits, $S1$ and quadrapole magnet $Q1$. It proceeds to the 90° analysing magnet where it is bent through 90° to the experimental hall. The beam energy resolution after the analysing magnet is $\sim$ 60 keV. It is further collimated by slits $S2, S3$ and $S4$ and focused

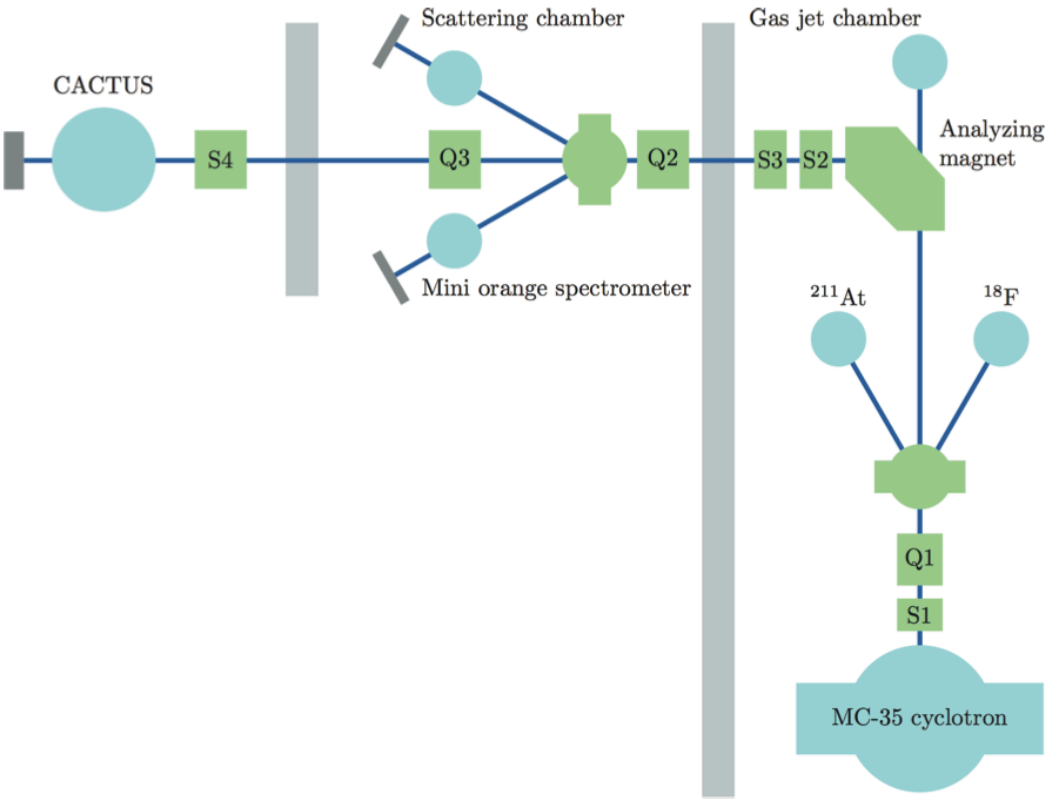

Figure 3.1: Schematic Layout of the OCL [15].

by quadrapole magnets $Q2$ and $Q3$ to the target chamber. This chamber is located at the center of the cylindrical frame that holds the CACTUS array. The typical diameter of the beam when it reaches the target is $\approx$ 1- 2 mm. The SiRi array which is used for charged particle detection is located under vacuum within the target chamber.

3.2 The SiRi Array

The SiRi (silicon ring) array was used to detect charged ejectiles from the reaction such as α and ^{3}He particles. It also allows for the discrimination of different charged ejectiles such as protons, deuterons, ^{3}He and α, due to their differences in mass and energy loss through the silicon detectors. The array consists of 8 trapezoidal shaped $\Delta E - E$ telescope detectors which form a

ring (see figure 3.2) around the target. The ΔE and E are $\approx$ 130 and 1550 μm thick Si detectors, respectively [56]. The ΔE detectors are positioned a few mm in front of the E detectors. Figure 3.3 illustrates the position of the $\Delta E - E$ telescope with respect to the beam axis and target.

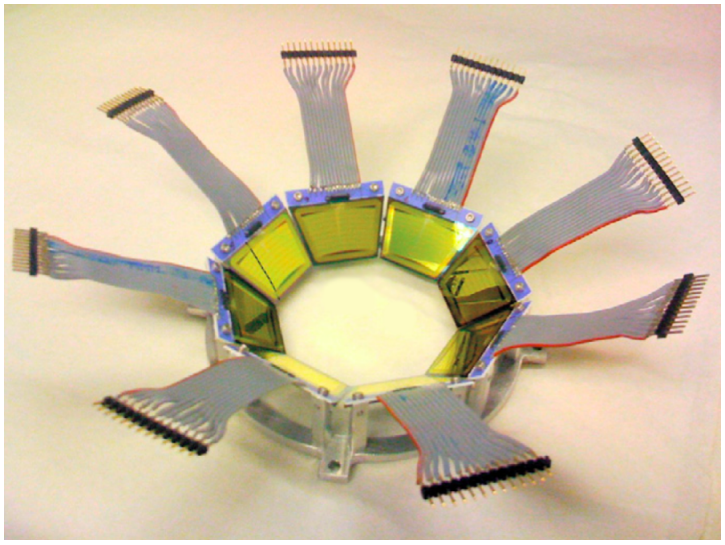

Figure 3.2: SiRi particle telescope modules [56].

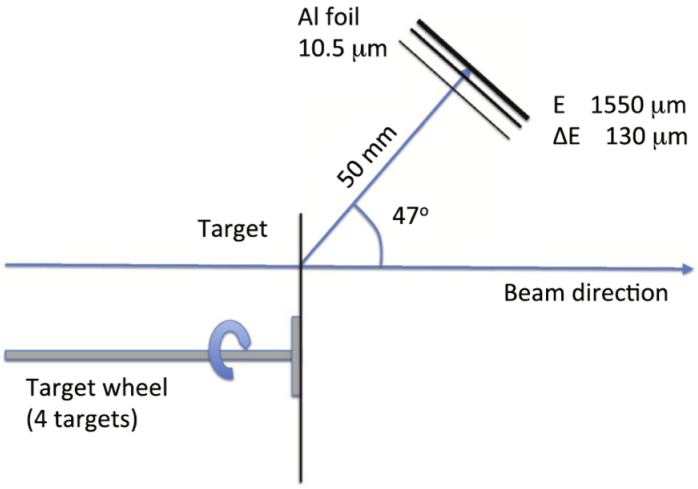

Figure 3.3: Position of the Si particle-telescope with respect to beam axis and target [56].

Each ΔE detector is segmented into 8 strips (see figure 3.4) which makes a total of 64 $\Delta E - E$ sub-particle-telescopes. The segmentation reduces pile-up events, which are rejected in the E detector shared by ΔE pads by requiring that only one ΔE pad fires.

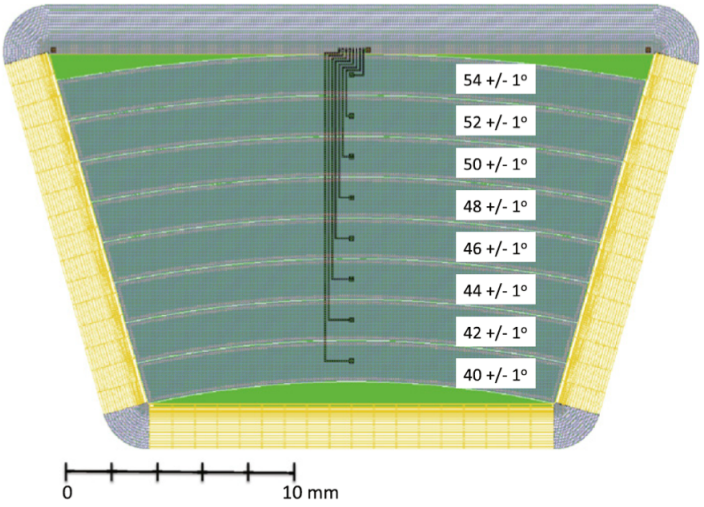

Figure 3.4: Layout of the front of one ΔE detector [56].

Each telescope covers a mean scattering angle θ between 40° and 54° in steps of 2° (equivalent to 1.7 mm) per pad. The energy resolution, for the present work, of the entire SiRi array is $\approx$ 260 keV which was determined from the FWHM of the ^{3}He elastic peak of 38 MeV. In front of the 8 telescope modules there is a cone of 10.5 μm thick aluminum foil (see figure 3.3) that shields the $\Delta E - E$ telescopes from δ electrons, which are ejected from the target atoms when bombarded by the beam particles.

3.3 CACTUS Array

The CACTUS multi-detector array was used to detect γ rays that were in coincidence with charged particles. The name CACTUS originates from its resemblance to a cactus tree. This array comprises 26 NaI(Tl) (Sodium Iodide

doped with Thallium) detectors with crystal dimensions of 5" x 5" each [57]. The NaI(Tl) detectors are mounted on a spherical frame (see figure 3.5) and located 22 cm away from the target. Each NaI(Tl) crystal is equipped with a conical 10 cm thick lead collimator of 7 cm diameter at the front surface of the NaI detector. Hence the array covers a solid angle of 17 % of 4π sr. It has a total efficiency and energy resolution of $\approx$ 14.1 % and $\approx$ 7 % FWHM for a 1332 keV transition. In front of each NaI(Tl) detector, a 2 mm thick copper absorber suppresses X rays. Each NaI(Tl) detector is surrounded by 3 mm thick lead sheets to avoid cross-talk between adjacent detectors.

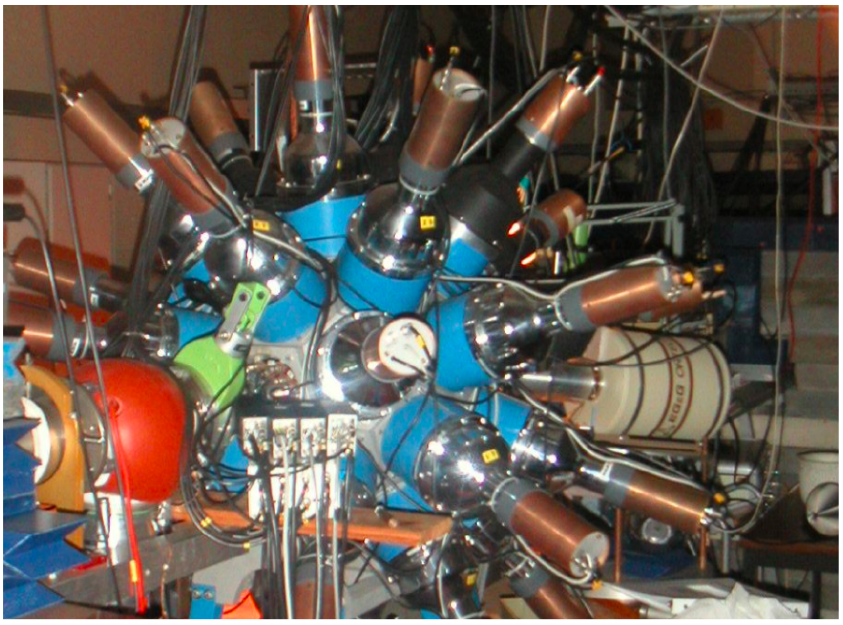

Figure 3.5: The CACTUS array of OCL [15].

3.4 Electronics

At OCL the first stage of the electronic chain is placed in the experimental hall very close to the detector setup. In particular, a multichannel power supply system (CAEN SY2527 Universal Multichannel Power Supply System)

is connected to the photomultipliers of the 26 NaI(Tl) detectors of CACTUS. This system is very stable and includes a CPU and Front Panel Section which can be interfaced to the desktop computer in the acquisition room. In this way the high voltage for each detector can be remotely monitored and set without the need to access the experimental hall. The HV applied to the NaI(Tl) photomultipliers range between 700 and 800 V. The SiRi silicon telescopes are biased with 30 V (ΔE detectors) and 350 V (E detectors) provided by four Mesytec MHV-4 modules (4 channel 400 V high precision bias supply units). These electronic units are also remotely controlled from the acquisition room. The signals generated from the eight 8-fold segmented ΔE detectors are sent to four Mesytec MPR-16 16-channel preamplifier modules. The signals from the eight E detectors are all processed by an additional Mesytec MPR-16 module. All the preamplifiers have sensitivities adapted to the expected energy deposits in the front and back detectors. The primary function of the preamplifiers is to extract the signal from the detectors without significantly degrading the intrinsic signal-to-noise ratio and drive it to the amplifiers situated in the data acquisition room. These preamplifiers are located very close to the scattering chamber, that contains the SiRi array, to reduce cable-induced noise.

The ΔE and E signals are then transferred to the data acquisition room, as differential signals to the Mesytec STM-16 modules including both spectroscopic amplifiers and timing-filter amplifiers, and also leading-edge discriminators. Figure 3.6 illustrates the electronics located in the data acquisition room. The signals of the NaI(Tl) detectors are also split into two STM-16 modules. Each of these modules gives a logical OR output of all the channels and which are finally summed up through the Fan in Fan out module. The OR of all the NaI(Tl) and all the SiRi E detectors are sent to a discriminator module, where the width of the NIM signal can be adjusted and a threshold is set for the input signal such that an output is generated. Wide OR signals en-

sure that they overlap when sent to the coincidence unit. The NaI(Tl) signals are delayed by ≈ 522 ns to ensure that the silicon detector signals are used as a start signal in the Time to Digital Converter (TDC) module to acquire only γ rays emitted together with the charged particles. In this experiment only the particle events are given as input trigger on the Amplitude to Digital Converter (ADC), where the a gate of 3 μs is provided by the Gate Generator.

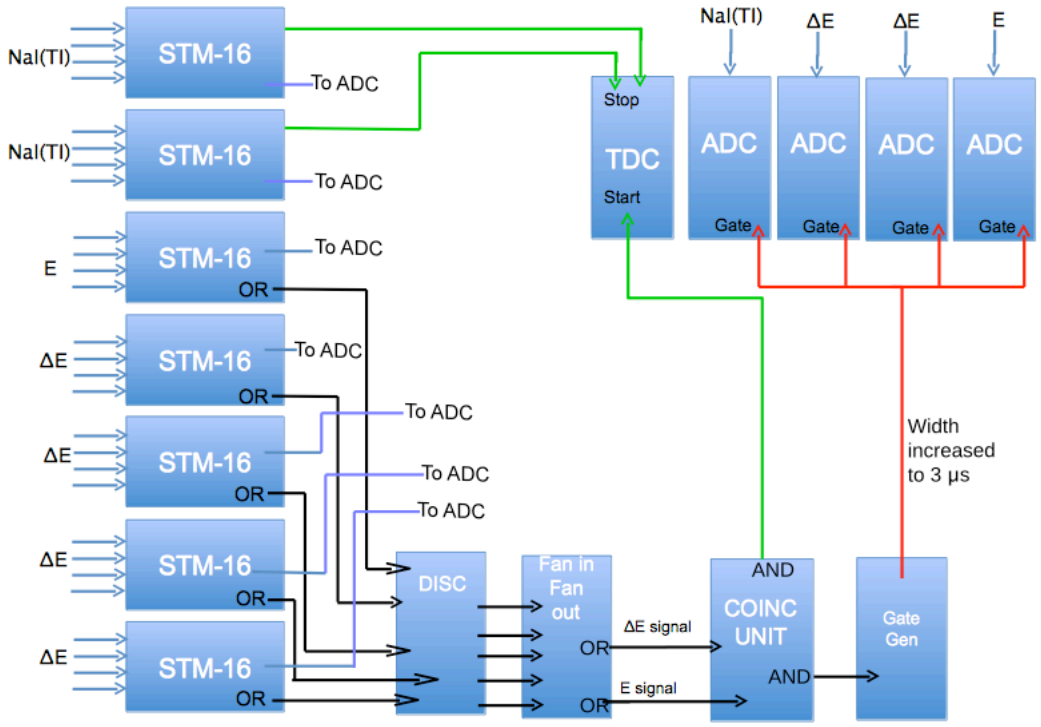

Figure 3.6: Block diagram for electronics in the data acquisition room of OCL.

3.5 Manufacturing of ^{139}La targets

The natural La target, with 99.9 % enrichment of ^{139}La, was manufactured under inert atmosphere inside a glove box. This atmosphere was achieved by removal of water and air using a mechanical pump and argon gas (inert) was used to vent the glove box. The target was rolled using mechanical rolling as La is ductile and allows the deformation process easily; this procedure was repeated until the desired thickness of 2.5 mg/cm^2 was reached. Targets

were transported in a glass container with silica gel and filled with argon gas to reduce water content which negatively affects La material that oxidizes rapidly when in contact with air. They were stored and transported in this condition for a period of 24 hours, maintaining their shinny slivery colour before use. Targets transported under vacuum and argon without silica gel oxidized. Figure 3.7 shows some of these targets.

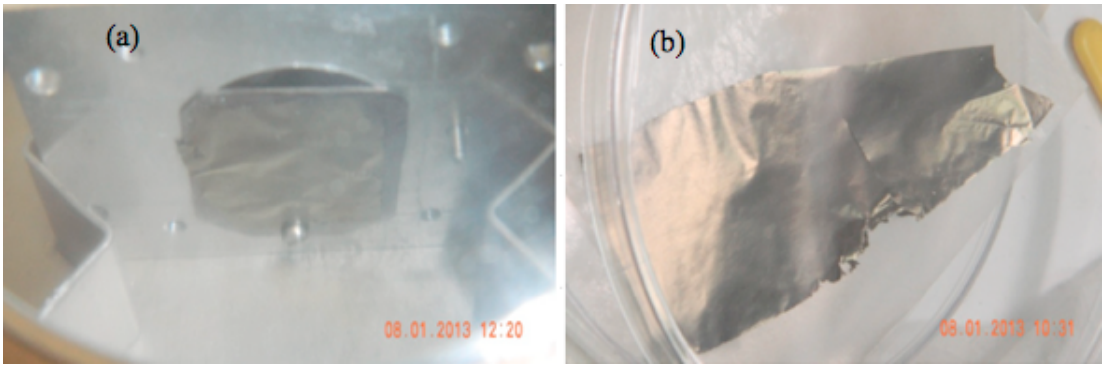

Figure 3.7: ^{139}La target on the frame (a) and sealed container (b) containing argon gas.

Chapter 4

Data Analysis and Results

4.1 Calibration of the SiRi Array

The calibration of the $\Delta E - E$ detectors was achieved using the SiRi kinematic calculator [58]. This calculator is used to compute particle energies which are expected to be deposited by charged ejectiles at various scattering angles of the SiRi array. It is based on the Bethe-Bloch formula [59] and it includes energy loss corrections of the charged particles in the target and the δ electron aluminum foil (see figure 3.3) spanned across the front face of the ΔE detectors.

The calculated $\Delta E - E$ plot of the ^{139}La(^{3}He, X) experiment, at 38 MeV beam energy, obtained using the SiRi calculator is shown in figure 4.1. This plot is for the innermost $\Delta E - E$ ring, at 40° with respect to the beam axis, and similar plots were obtained for other rings. The corresponding experimental $\Delta E - E$ plots before calibration are shown in figure 4.2. Figure 4.1 clearly reveals the energy distributions for all five charged particles (protons, deutrons, tritons, ^{3}He and α) detected in the SiRi particle telescopes. However, this is not straightforward identify in figure 4.2 because the particle telescopes had not been calibrated yet.

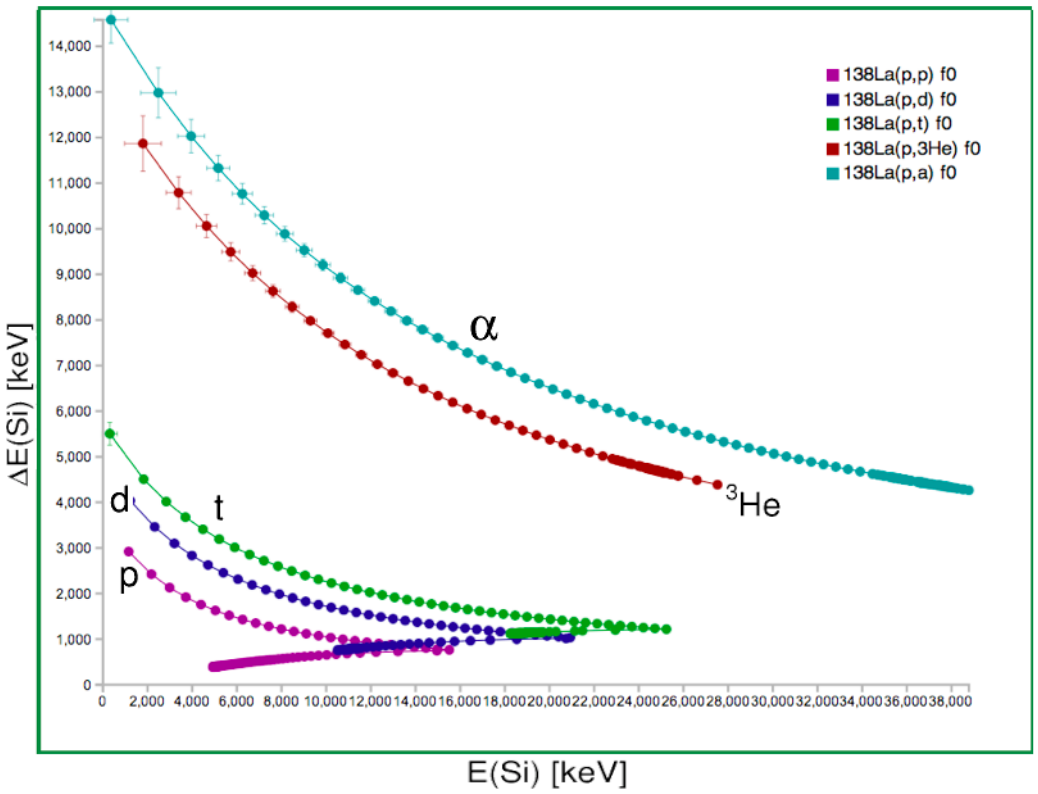

Figure 4.1: Calculated $\Delta E - E$ plot of the inner most ring obtained using the SiRi kinematic calculator.

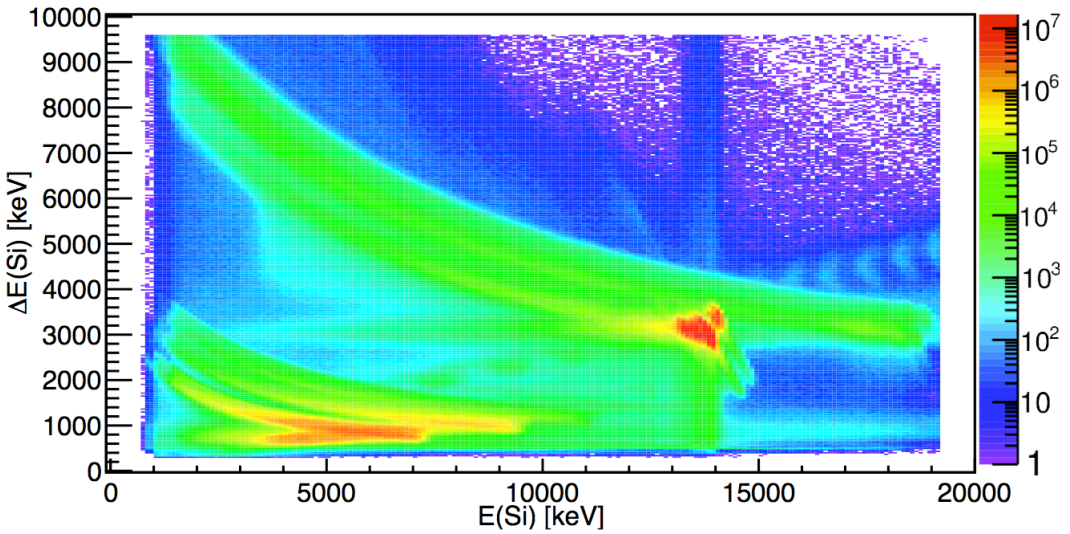

Figure 4.2: $\Delta E - E$ plots for the ^{139}La(^{3}He, X) reaction before calibration.

In fact there are 64 experimental $\Delta E - E$ plots corresponding to 64 $\Delta E - E$ telescope detectors. However, the outermost ring consisting of 8 telescopes was

excluded due to technical problems which were experienced during the calibration. Hence 56 experimental $\Delta E - E$ plots were fitted to their corresponding calculated $\Delta E - E$ plots and calibrated. An experimental $\Delta E - E$ plot, of the 56 $\Delta E - E$ telescopes, after calibration is shown in figure 4.3 and clearly reveals the energy distributions for different charged particles.

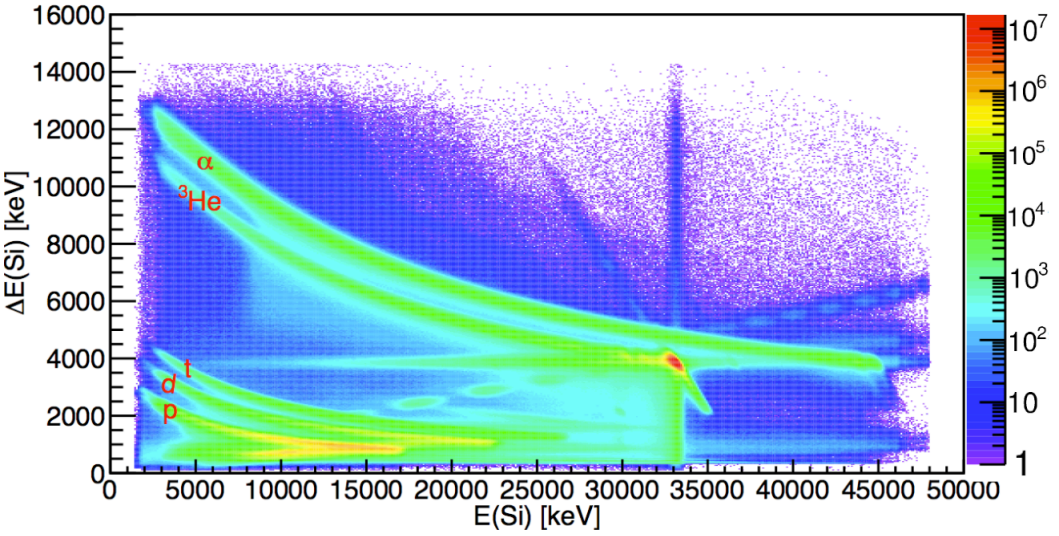

Figure 4.3: $\Delta E - E$ plots for the ^{139}La(^{3}He, X) reaction after calibration.

In addition to the calibration of the particle telescopes for the ^{139}La(^{3}He, X) experiment, these were also calibrated for the ^{28}Si(^{3}He, X) experiment. This was achieved following the same procedure as explained above. Figure 4.4 shows the corresponding calibrated experimental $\Delta E - E$ plot. This calibration was performed in order to obtain the excitation energy, E_x, spectrum on which well resolved γ ray peaks could be gated and used to calibrate the γ ray spectra.

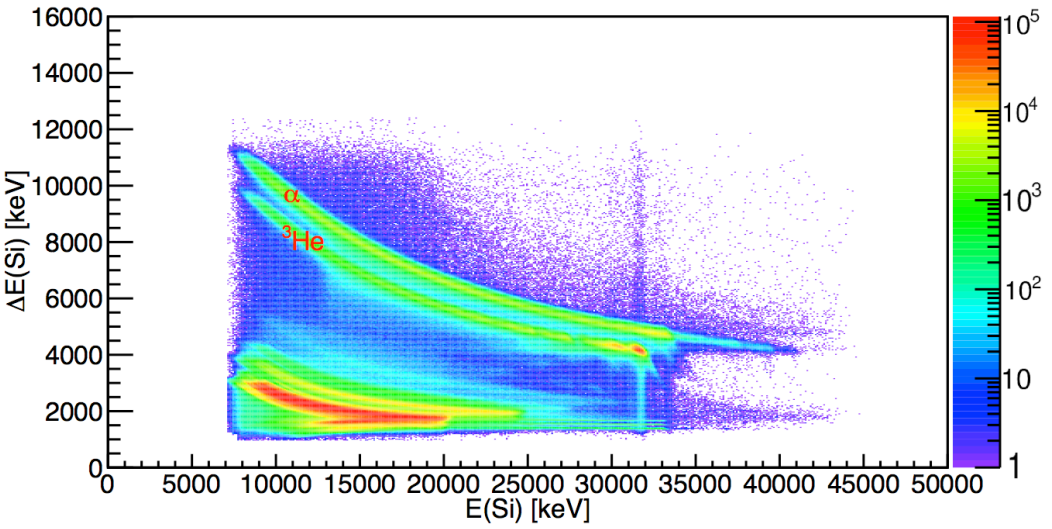

Figure 4.4: The calibrated $\Delta E - E$ plots for the ^{28}Si(^{3}He, X) experiment.

4.2 Excitation Energies of ^{138,139}La

The ^{139}La(^{3}He, X) experiment opened various reaction channels as seen in figure 4.3. Of particular interest to this research were the ^{139}La(^{3}He, $\alpha\gamma$)^{138}La and ^{139}La(^{3}He, ^{3}Heγ)^{139}La reactions. As a result the desired reactions and random events were reduced by gating on either α or ^{3}He particles through a "banana" gate (see figures 6.1 and 6.2 in the appendix).

The measured energies of the α and ^{3}He particles were converted to E_x for the ^{138}La and ^{139}La nuclei produced in the ^{139}La(^{3}He, $\alpha\gamma$)^{138}La and ^{139}La(^{3}He, ^{3}Heγ)^{139}La reactions, respectively, using the kinematics and Q-values of the reactions. Figures 4.5 and 4.6 show the constructed E_x spectra of both nuclei.

4.3 Calibration of the CACTUS Array

The $\Delta E - E$ plot in figure 4.4 was used to gate on the α particles to eliminate all other unwanted reactions and focus only on the ^{28}Si(^{3}He, $\alpha\gamma$)^{27}Si reaction channel, following the same procedure discussed in the previous section. The energies of these α particles were also converted into E_x of ^{27}Si to construct

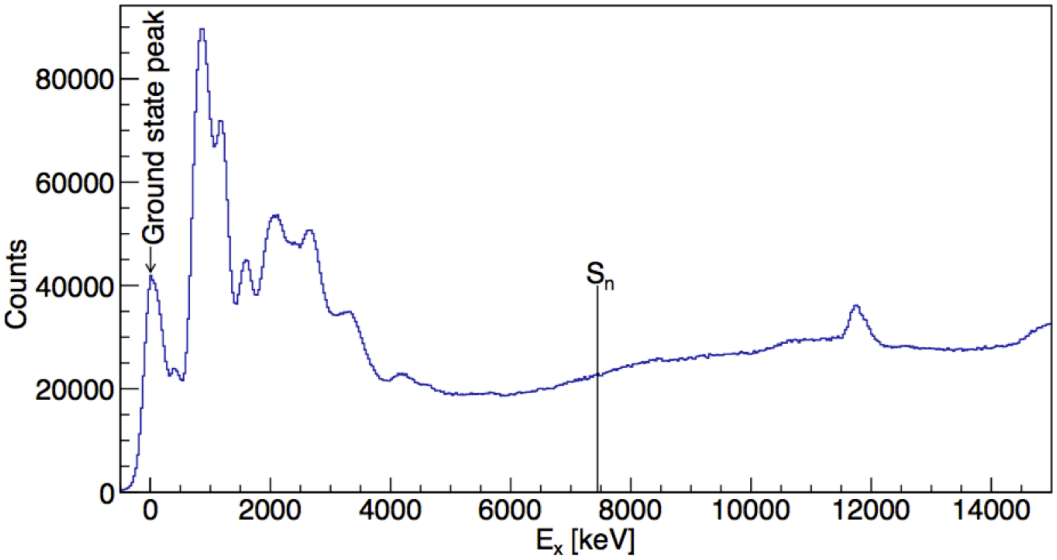

Figure 4.5: The excitation energy spectrum, without γ ray coincidence requirement, for ^{138}La. S_n indicates the location of neutron separation energy.

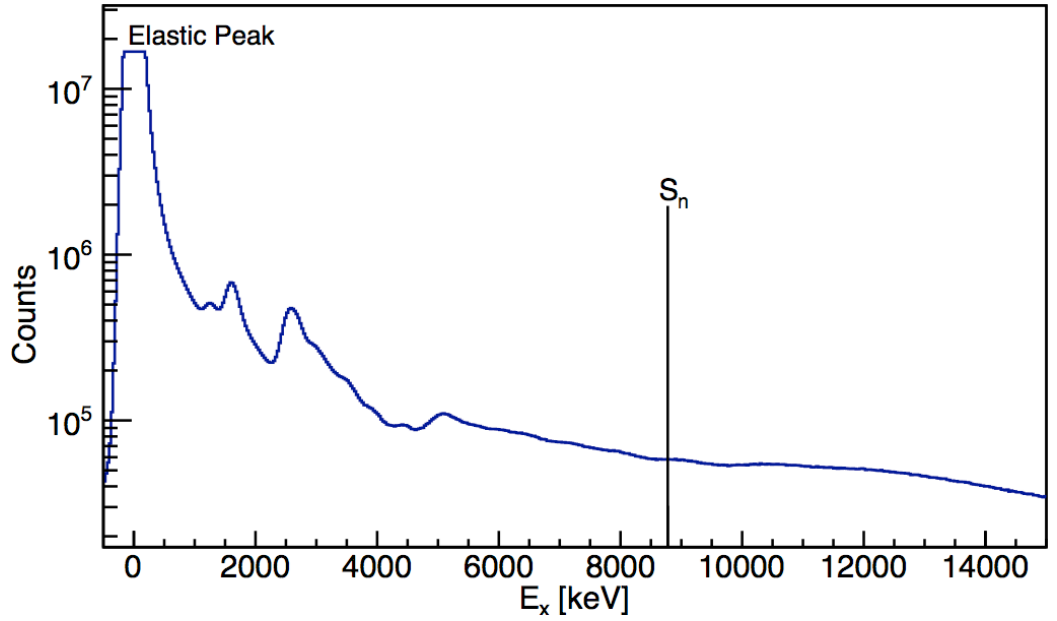

Figure 4.6: The excitation energy spectrum, without γ ray coincidence requirement, for ^{139}La. S_n indicates the location of neutron separation energy.

an excitation energy spectrum of ^{27}Si (see figure 4.7).

By gating on the $E_x = 3540.2$ keV state (see figure 4.7) and extracting the γ ray spectra for all 26 NaI(Tl) detectors, the two well resolved γ ray peaks

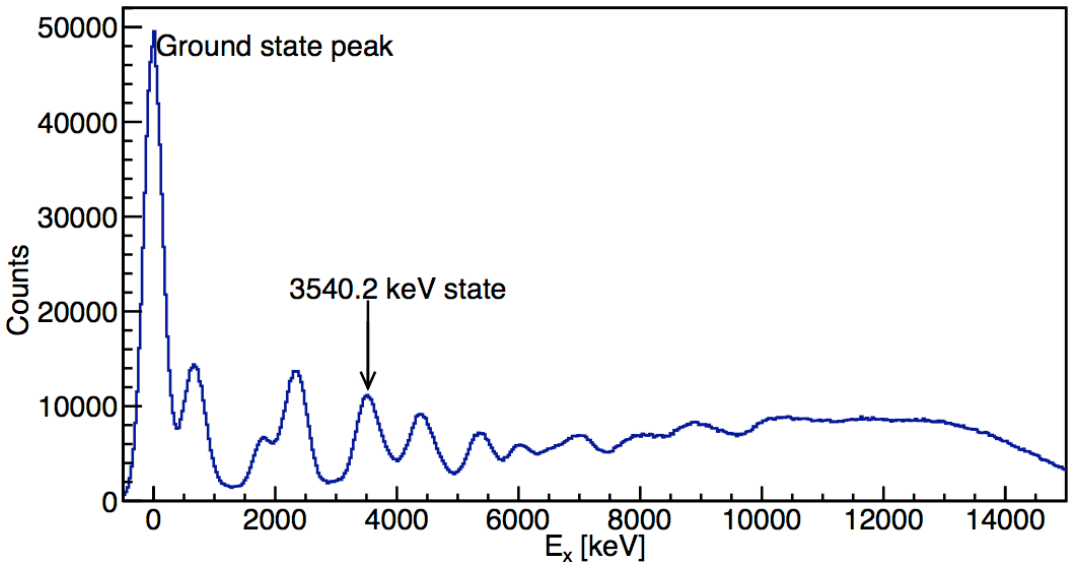

Figure 4.7: The excitation energy spectrum of ^{27}Si constructed from α energies without γ ray coincidence requirements.

corresponding to the 780.9 keV and 2759.1 keV γ ray transitions originating from this state in ^{27}Si were obtained (see figure 4.8). Other particle gates do not yield well enough resolved γ ray transitions. The linear calibration of γ ray spectra for each NaI(Tl) detector was achieved using these two γ ray transitions. The calibrated γ ray spectrum, of all detectors combined, showing the 780.9 keV and 2759.1 keV peaks is given in figure 4.8.

4.4 Time Calibration

During the detection of particle γ ray coincidence events the SiRi array triggers a start signal, while the CATCUS array triggers the corresponding stop signal in the TDC modules. However, the rise time of those signals depends on the signal amplitudes. The high-energy events have shorter rise times compared to low-energy events. This means that the high-energy signals will cross the discriminator threshold earlier in time than the low-energy signals. This effect is the so-called *walk* with the implication that high-energy events will be detected as if they occurred before the low-energy events, even if they oc-

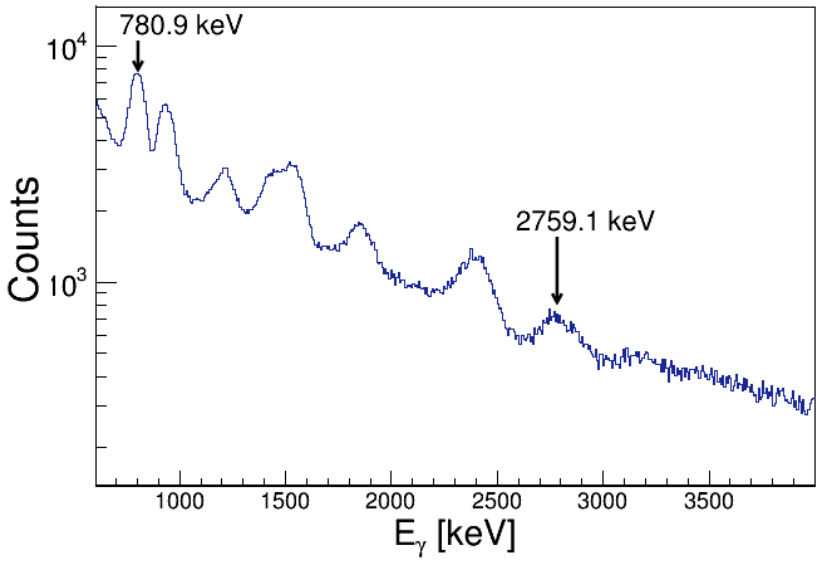

Figure 4.8: The calibrated γ ray energy spectrum of ^{27}Si obtained with the E_x gate on the 3.5 MeV state for all NaI(Tl) detectors in the CACTUS array.

curred at the same time. This is illustrated by the energy-time matrix in figure 4.9 gated on ^{3}He. A similar matrix was obtained for the ^{139}La(^{3}He, $\alpha\gamma$)^{138}La reaction (see figure 6.3 in the appendix).

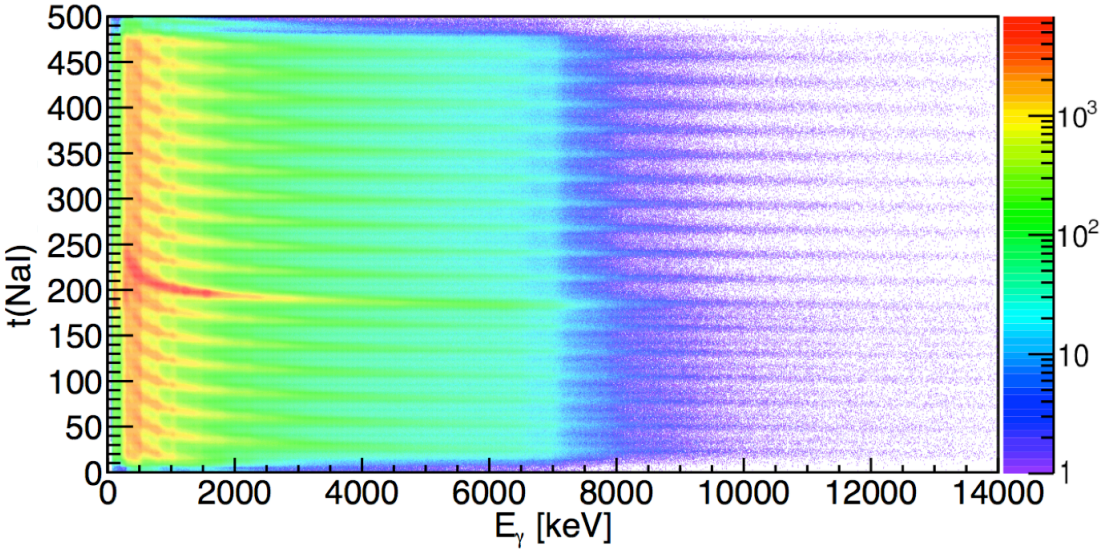

Figure 4.9: The energy-time matrix of the CACTUS array for the ^{139}La(^{3}He, ^{3}Heγ)^{139}La reaction.

The correction of the *walk* effect is achieved by fitting the function of the form,

$$t(x) = a + \frac{b}{x+c} + dx + 200 \tag{4.1}$$

where $t(x)$ and x are channels corresponding to time and γ ray energy, respectively, to the energy-time matrices and obtain the values of the coefficients a, b, c and d for the energy-time matrix. These coefficients are then used to correct for *walk*, aligning the time peaks of all coincidence events. The prompt peaks are all positioned at channel $\approx$ 200 which is represented by the offset value of equation (4.1). The energy-time matrix, for ^{139}La, after this correction is shown in figure 4.10. For ^{138}La this matrix is displayed in the appendix (see figure 6.4). These matrices are specifically for NaI(Tl) detectors but similar matrices were obtained also for the silicon detectors using the same *walk* correction method. The corresponding time spectra are shown in figures 4.11 and 4.12.

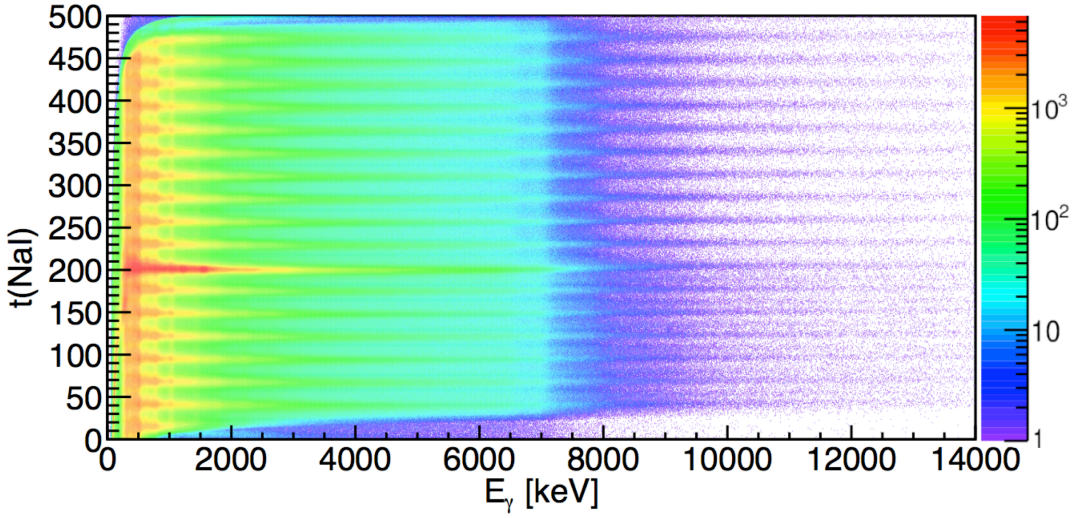

Figure 4.10: The energy-time matrix from the ^{139}La(^{3}He, ^{3}He'γ)^{139}La reaction after *walk* correction for the CACTUS array.

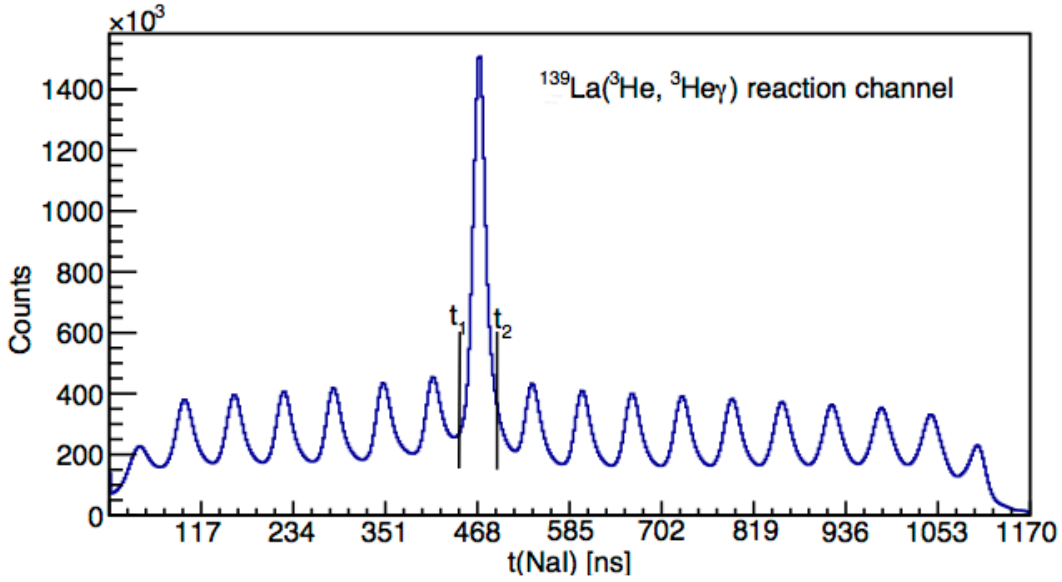

Figure 4.11: The projection of figure 4.10 on the time-axis after time calibration. t_1 and t_2 corresponds to the time gate used to reduce random events.

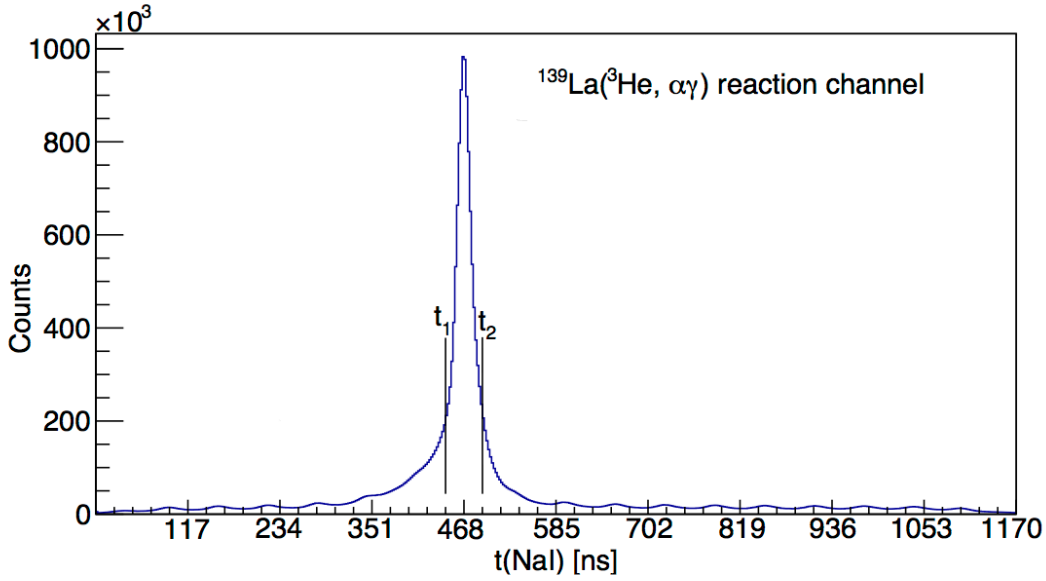

Figure 4.12: The projection of figure 6.4 on the time-axis after time calibration. t_1 and t_2 corresponds to the time gate used to reduce random events.

4.5 Particle γ ray Coincidence Matrices

The particle γ ray coincidence events were extracted for both reactions of interest by gating on either ^{3}He or α particles, and the corresponding time prompt peak (see figures 4.11, 4.12, 6.1 and 6.2). Each time gate, $t_2 - t_1$, is 20 channels wide which is equivalent to $\approx$ 50 ns, since the OCL RF (radio frequency) frequency of 15.3 MHz gives 65.36 ns time between beam pulses for the 38 MeV ^{3}He beam. From these events the E_x vs E_γ matrices were generated using the constructed E_x and calibrated E_γ data, and gating on the respective prompt time peaks ($t_2 - t_1 \approx 50$ ns). These matrices are shown in figures 4.13 and 4.14. The 45° diagonal lines on these matrices signify that no γ ray can exist which is emitted from a state with energy less than the energy of that γ ray. The counts start decreasing at $\approx S_n$, as expected, because beyond this energy the nuclei emit both neutrons and γ rays. This channel competes with the one where only gamma rays are emitted, and the emission of a neutron with a low-energy γ ray is more probable than the emission of a single higher-energy γ ray. These clear features in the matrices further confirm good calibration of both the SiRi and CACTUS arrays.

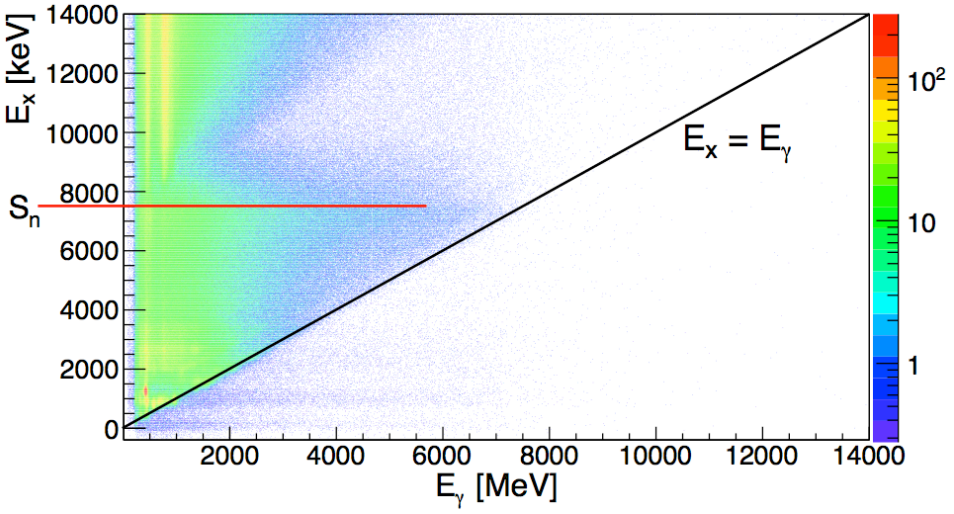

Figure 4.13: The E_x vs E_γ matrix of ^{138}La. The horizontal red line indicates the neutron separation energy, S_n.

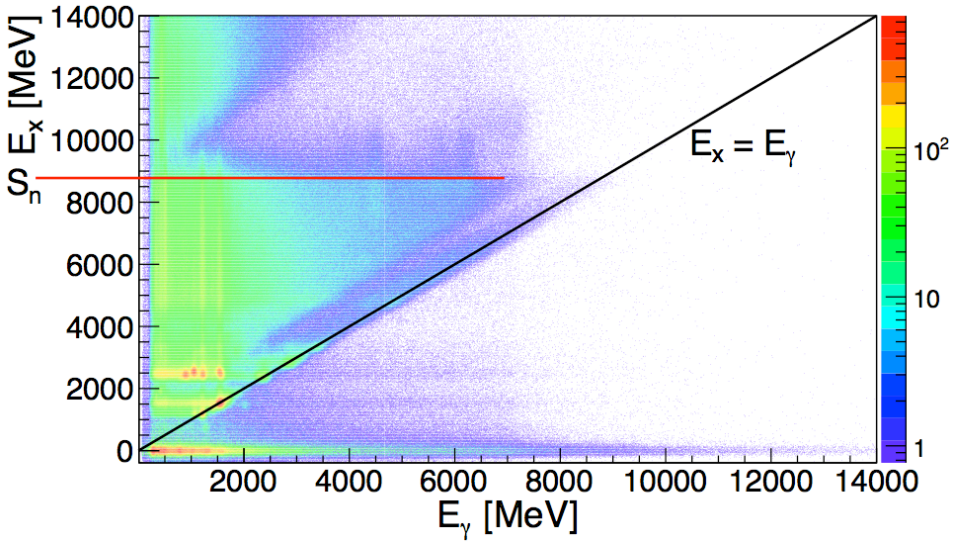

Figure 4.14: The E_x vs E_γ matrix of ^{139}La. The neutron separation energy, S_n, is indicated by the horizontal red line.

Further, the γ ray spectra of both nuclei were unfolded using the unfolding iterative method discussed in section 2.1.1. The respective raw and unfolded γ ray spectra are shown in figures 4.15 and 4.16.

4.6 Primary γ ray Matrices

From the unfolded γ ray spectra the unfolded E_x vs E_γ matrices were constructed and used to generate the primary γ ray matrices for both nuclei, using the first generation iterative procedure which is discussed in section 2.1.5. The first generation matrices of ^{138}La and ^{139}La are shown in figure 4.17. From these matrices the nuclear level densities and radiative strength functions of the ^{138}La and ^{139}La nuclei were extracted. The first generation matrix of ^{139}La reveals a valley of no data (see figure 4.17 (b)) which corresponds to the 1043.1 keV gap (see Ref. [21]) between the first- and second-excited states of ^{139}La. In the same figure two vertical regions corresponding to $E_\gamma \approx 1$ and 1.7 MeV are visible which are characterized by lower statistics due to over-subtraction of discrete and strong γ ray transitions during the generation of $P(E_x, E_\gamma)$.

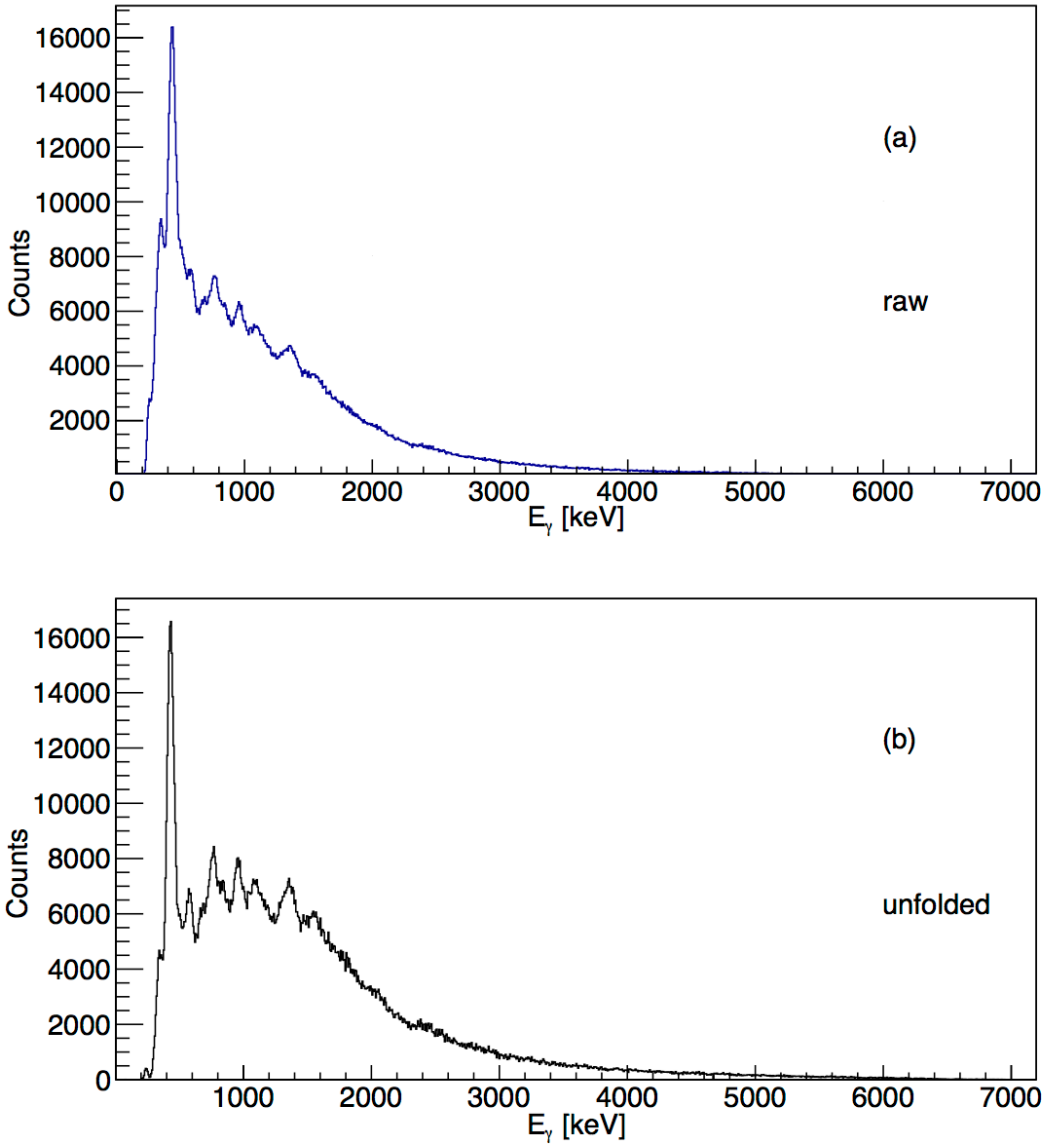

Figure 4.15: The raw (a) and unfolded (b) γ ray spectra for ^{138}La corresponding to $E_x \leq 7.1$ MeV.

4.7 Radiative Strength Functions and Nuclear Level Densities

The $f(E_\gamma)$ and $\rho(E_x)$ were extracted by following the method discussed in section 2.1.6. The χ^2 minimization between $P(E_x, E_\gamma)$ and $P_{th}(E_x, E_\gamma)$ was performed in the energy regions of $E_\gamma \geq 1$ MeV and 3.5 MeV $\leq E_x \leq 7.1$

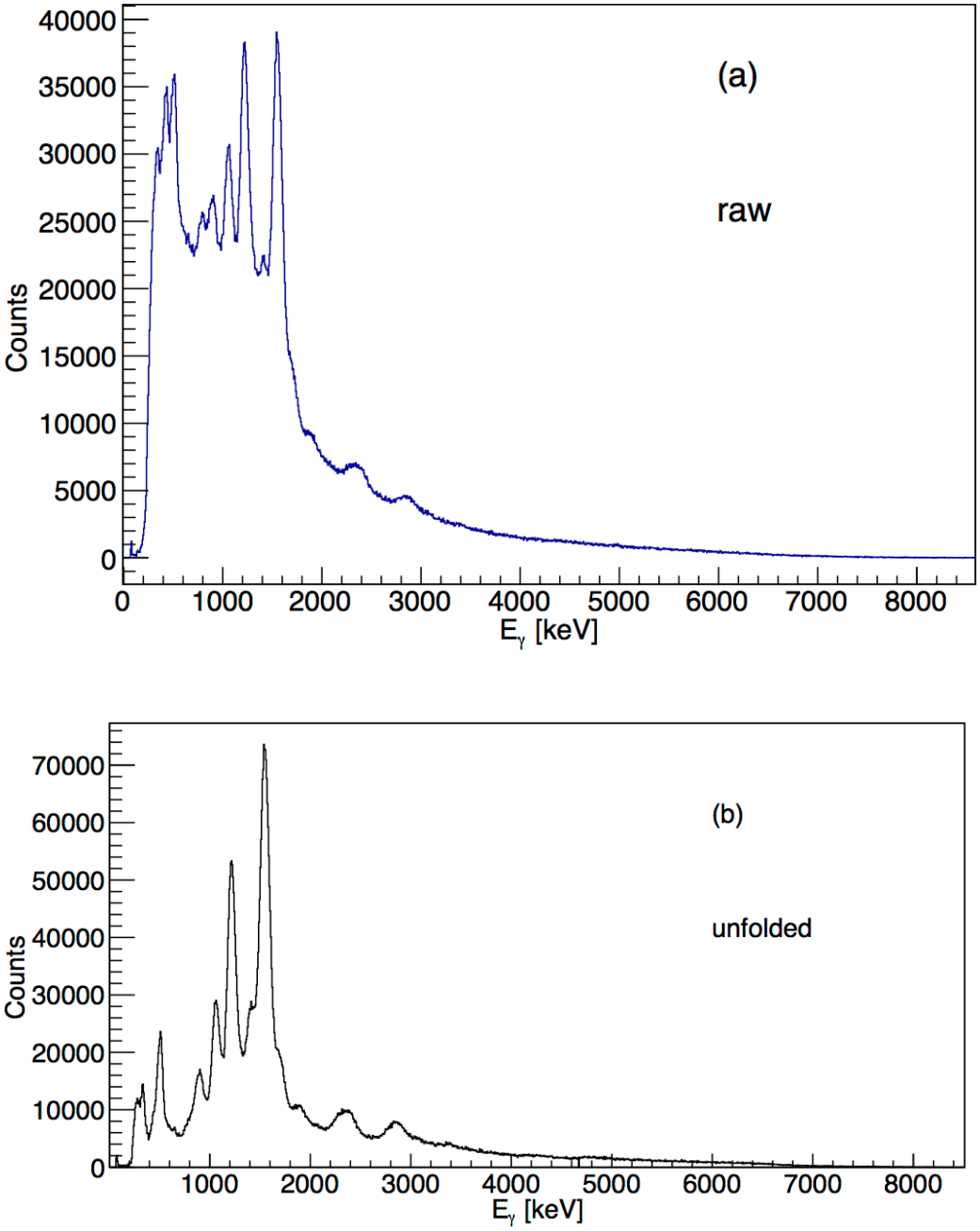

Figure 4.16: The raw (a) and unfolded (b) γ ray spectra of ^{139}La for $E_x \leq 8.5$ MeV.

MeV for ^{138}La, and $E_\gamma \geq 1.7$ MeV and 3.5 MeV $\leq E_x \leq 8.5$ MeV for ^{139}La, to exclude the non-statistical excitation energy regions. The fitted regions of the experimental primary γ ray matrices, $P(E_x, E_\gamma)$, of ^{138}La and ^{139}La and

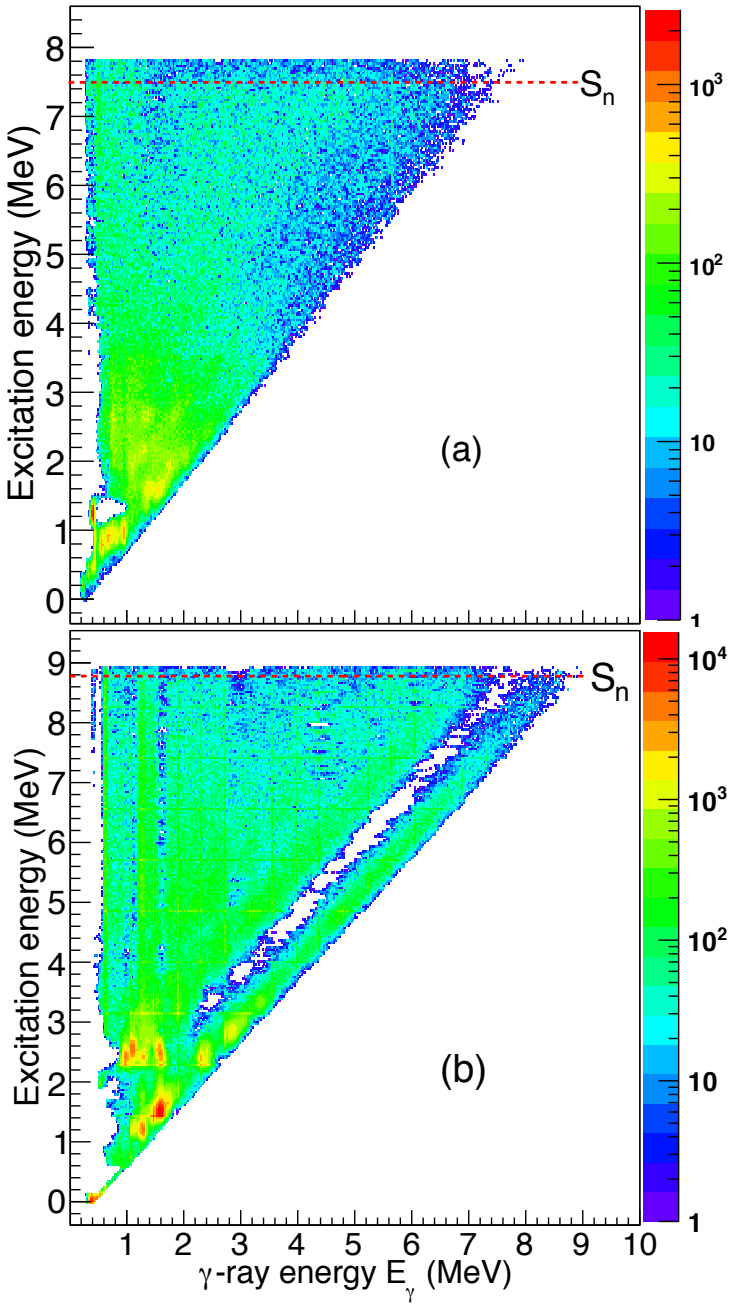

Figure 4.17: The primary γ ray matrices for ^{138}La (a) and ^{139}La (b).

the corresponding theoretical primary γ ray matrices, $P_{th}(E_x, E_\gamma)$, are shown in figures 4.18 and 4.19. Overall, for both nuclei the $P_{th}(E_x, E_\gamma)$ appear very similar to $P(E_x, E_\gamma)$ providing confidence about the $P_{th}(E_x, E_\gamma)$ used.

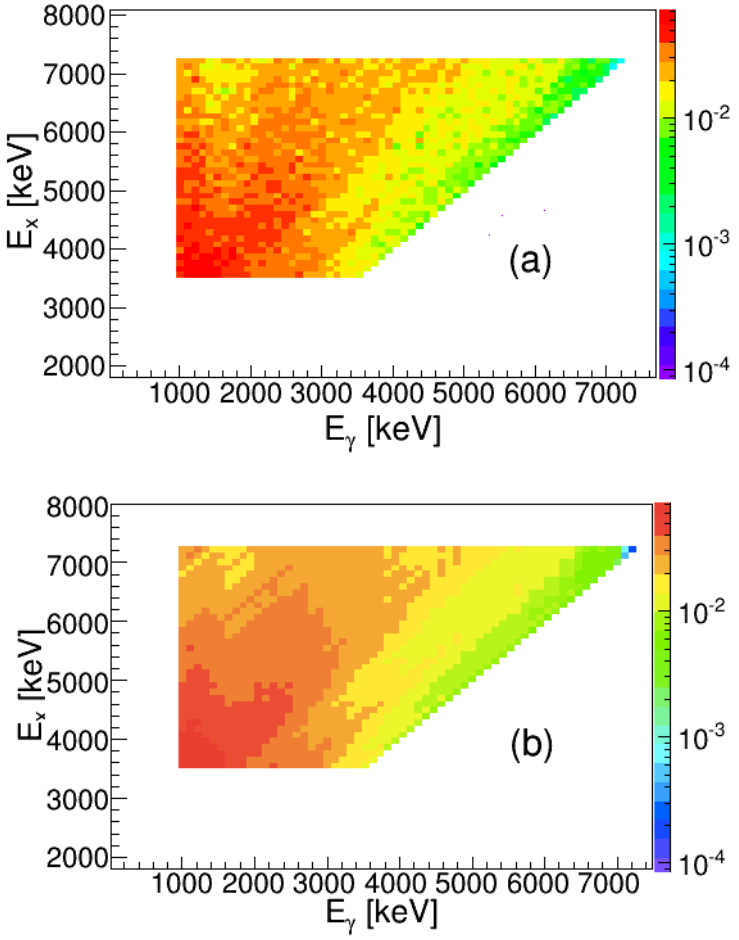

Figure 4.18: The fitted region of the $P(E_x, E_\gamma)$ (a) and corresponding $P_{th}(E_x, E_\gamma)$ (b) for ^{138}La.

The resulting $\rho(E_x)$ and $f(E_\gamma)$ are shown in figures 4.20 and 4.21 for both La isotopes. The solid line at low energies is the nuclear level density of known discrete states while the dotted line is the interpolated nuclear level density using the CT model (equation 2.32). The sets of vertical arrows at low and high energies in figure 4.20 show the regions where the experimental $\rho(E_x)$ was normalized to the level density of known discrete states and the interpolated level density, respectively.

In the case of ^{139}La, $\rho(S_n) = 2.9 \pm 0.6 \times 10^5$ MeV^{-1}, was used for normalization and was calculated from the experimental average neutron resonance level

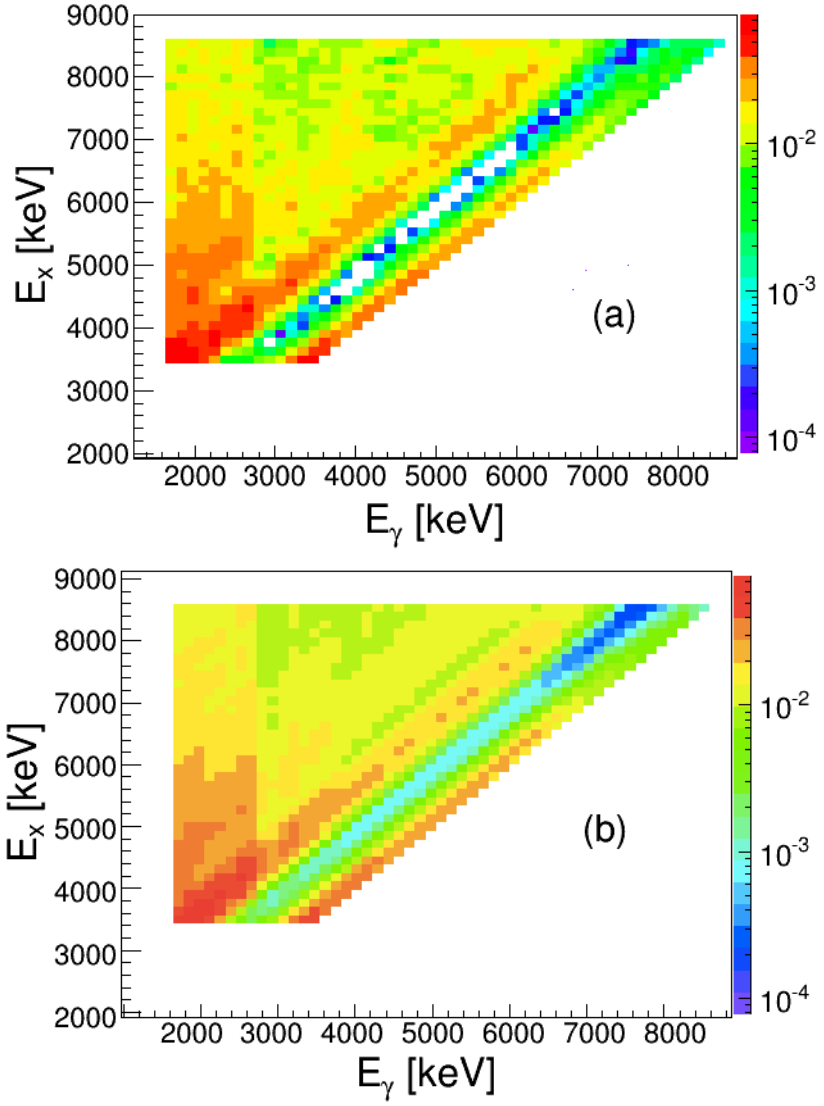

Figure 4.19: The fitted region of the $P(E_x, E_\gamma)$ (a) and corresponding $P_{th}(E_x, E_\gamma)$ (b) for ^{139}La.

spacing, D_0 (see Table 4.1), using the HFB + Combinatorial model (see section 2.2.3). This value is in excellent agreement with $\rho(S_n) = 2.5 \pm 0.6 \times 10^5$ MeV^{-1} from the back-shifted Fermi gas approach discussed in section 2.2.1. The absolute normalization parameter B is calculated using equation (2.20). The D_0 and $\langle \Gamma_\gamma(S_n,\ J_T, \pi_T)\rangle$, are average values and were obtained from [20, 60]. However, for ^{138}La there are neither D_0 nor $\langle \Gamma_\gamma(S_n,\ J_T, \pi_T)\rangle$ experimental values available in the literature. Therefore, the value of $\langle \Gamma_\gamma(S_n,\ J_T, \pi_T)\rangle$ was

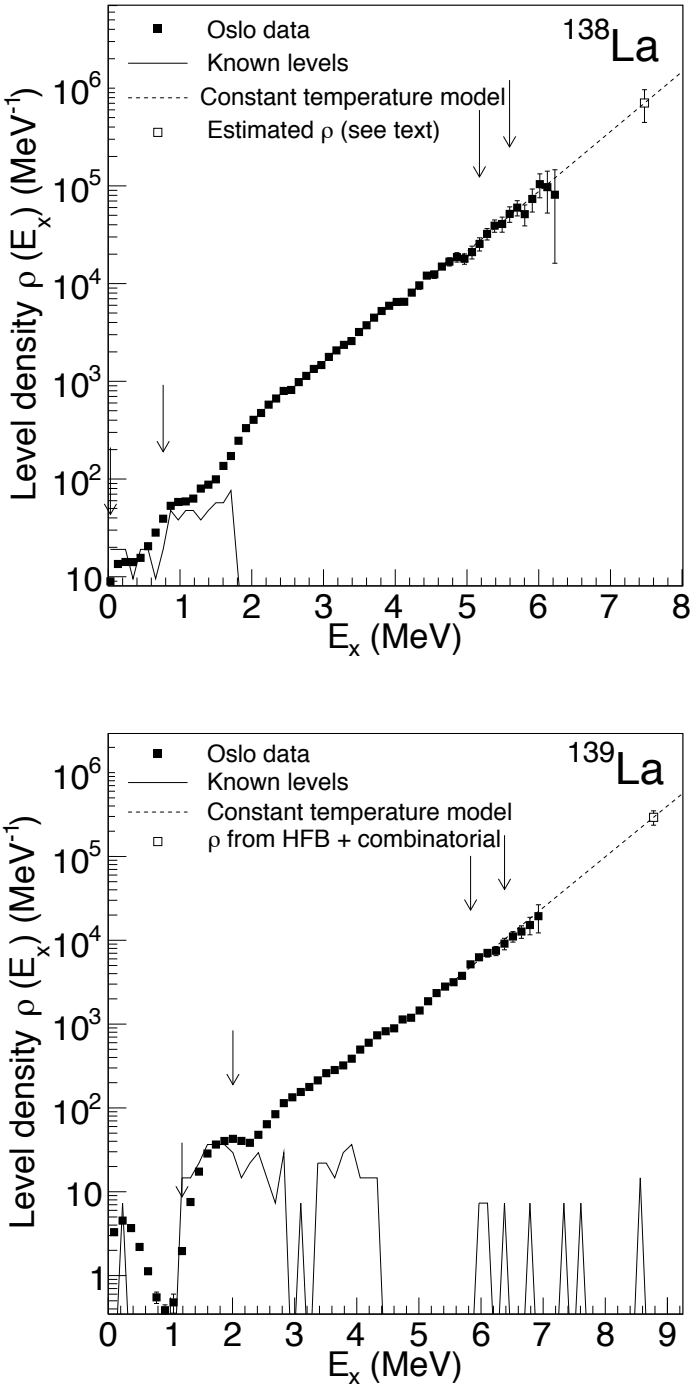

Figure 4.20: The measured nuclear level densities of both nuclei.

estimated from a spline fit as implemented in the TALYS reaction code [8], while the $\rho(S_n)$ value was extracted by normalizing $\rho(E_x)$ of ^{138}La with the

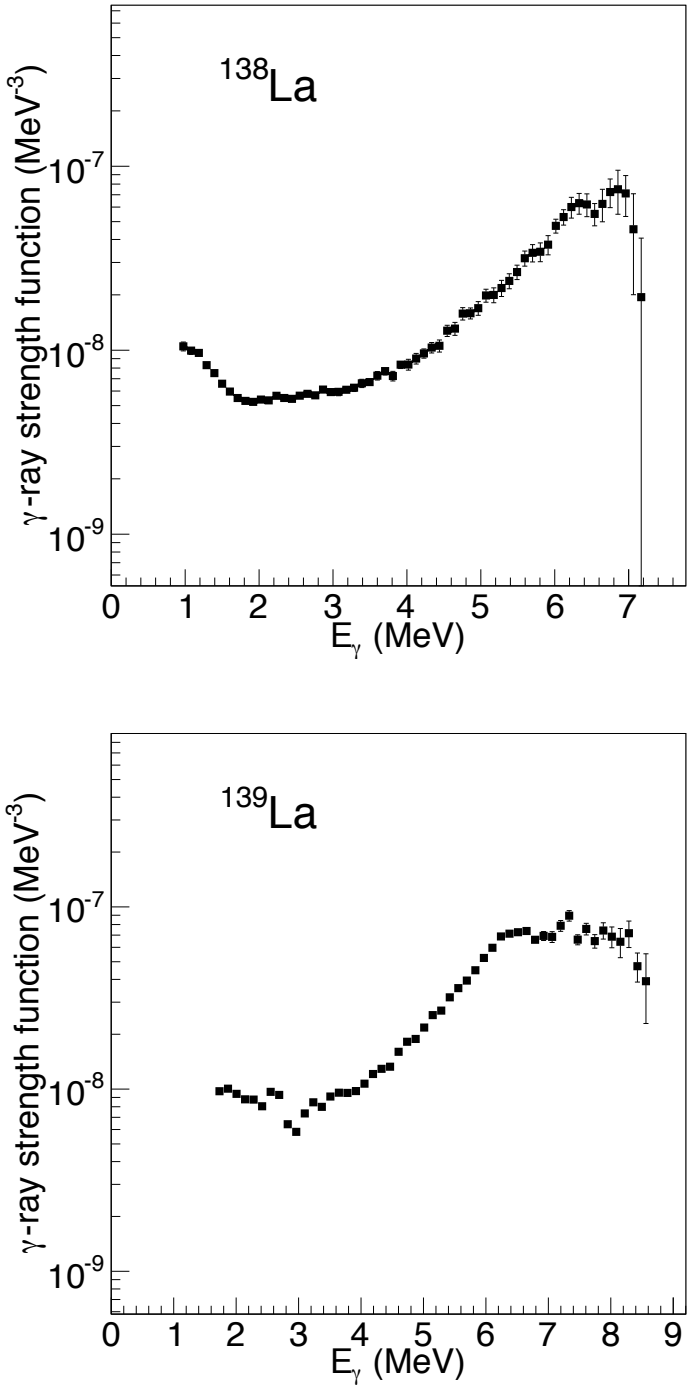

Figure 4.21: Radiative strength functions of both nuclei.

requirement of having the same slope as $\rho(E_x)$ in ^{139}La. It is expected that $\rho(E_x)$ of neighboring isotopes have the same slope as it is observed in other

nuclear species [43, 61, 62]. This is illustrated in figure 4.22 for ^{138,139}La. The resulting value for $\rho(S_n)$ is then used to calculate D_0 for ^{138}La with equation (2.19). The parameters which were used for the normalization of $\rho(E_x)$ and $f(E_\gamma)$ are summarized in Table 4.1.

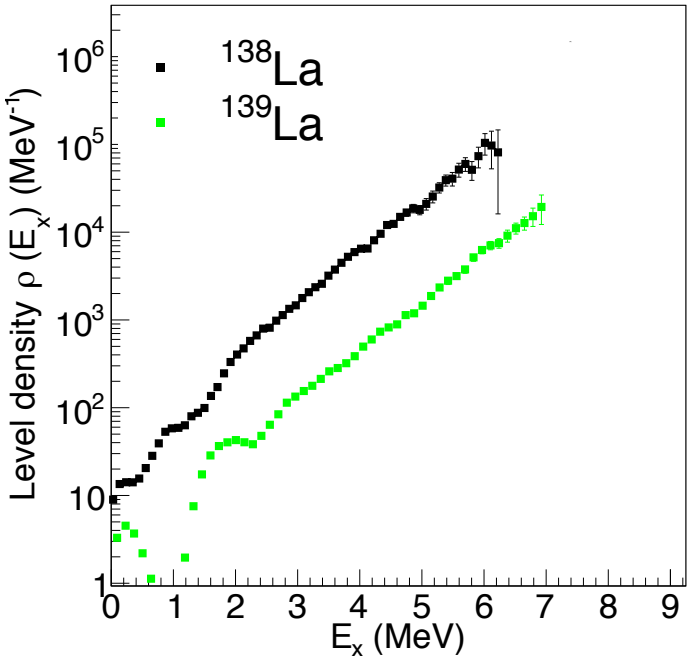

Figure 4.22: The nuclear level densities of ^{138}La and ^{139}La.

Table 4.1: Parameters used for the normalization of $\rho(E_x)$ and $f(E_\gamma)$ in ^{138,139}La.

Isotope	σ	D_0 (eV)	$\rho(S_n)$ (10^5MeV^{-1})	$\langle\Gamma_\gamma(S_n)\rangle$ (meV)
^{138}La	6.9±0.7[a]	20.0±4.4[b]	7.1±1.9[b]	71.0±13.6[b]
^{139}La	5.5±0.6[a]	31.8±7.0[c]	2.9±0.6[a]	95.0±18.2[c]

[a] Calculated with the HFB + Combinatorial model.
[b] Estimated values (see text for details).
[c] Average value from Refs. [20, 60].

Figure 4.23 shows the $f(E_\gamma)$ of both nuclei of interest together with data extracted from the ^{139}La(γ, n) and ^{139}La$(\gamma$, x) cross-sections, taken from [63, 64] for comparison. The $f(E_\gamma)$ of ^{138}La has the same slope, α, as $f(E_\gamma)$ of

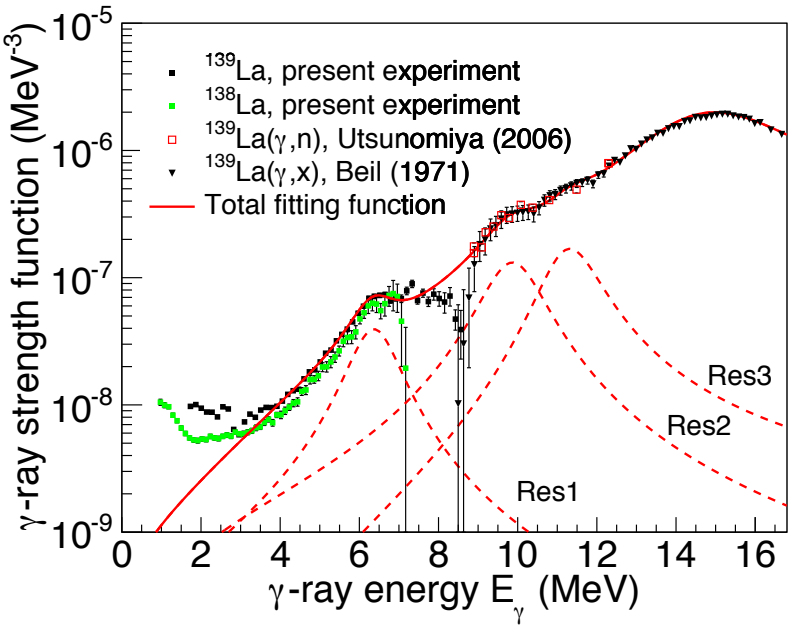

Figure 4.23: Comparison of $f(E_\gamma)$ with photoneutron cross-section data. "Res1", "Res2", and "Res3" indicate the fits to the individual resonance structures.

^{139}La due to the normalization of the $\rho(E_x)$ of ^{138}La as discussed above, and the fact that for each nucleus the $\rho(E_x)$ and $f(E_\gamma)$ have the same value of α (see section 2.1.6). The giant electric dipole resonance (GEDR) of ^{139}La at $E_\gamma \approx 15.6$ MeV was fitted with an enhanced generalized Lorentzian function, f^{EGLO} (see section 2.4.5), with a constant nuclear temperature, $T_f = 0.1$ MeV, which was considered as a free parameter. The excess strengths at $E_\gamma \approx 11.4$ ("Res3" in figure 4.23) and 9.9 MeV ("Res2" in figure 4.23) were fitted with the standard Lorentzian function, f^{SLO} (see section 2.4.5), respectively. In addition, an enhancement in the strength of ^{139}La at $E_\gamma \approx 6.4$ MeV is observed and labelled as "Res1". In figure 4.23 this resonance is described using the f^{SLO}. Therefore, the total fitting function is given by $f(E_\gamma) = f^{SLO}_{Res1}(E_\gamma) + f^{SLO}_{Res2}(E_\gamma) + f^{SLO}_{Res3}(E_\gamma) + f^{EGLO}_{GEDR}(E_\gamma)$. The Lorentzian parameters used in this fit are listed in Table 4.2. For the GEDR the parameters were somewhat increased from Ref. [20] to obtain the best fit to the experimental data, while for other resonances they were directly determined from the fit

to the data. Overall, the present data exhibit very good agreement with the extrapolated tail of the GEDR data of Ref. [63, 64]. The total fitting function is not fitted to the $f(E_\gamma)$ of ^{138}La measured in the present work, but $f(E_\gamma)$ of ^{138}La is included in figure 4.23 for comparison.

Table 4.2: Lorentzian parameters used for the fit to the experimental data, where E_0, σ_0 and Γ_0 are the centroid energies, cross-sections and widths of the resonances.

Resonance	E_0 (MeV)	σ_0 (mb)	Γ_0 (MeV)
Res1	6.4	2.9	1.3
Res2	9.9	15	1.6
Res3	11.4	15	1.4
GEDR	15.6[a]	336	5.6[a]

[a] Modified from Ref. [20] (see text for details).

Chapter 5

Discussion

5.1 Radiative Strength Function and Nuclear Level Density

The $f(E_\gamma)$ of the ^{138,139}La nuclei show several interesting and unexpected features, 1) the pronounced low-energy enhancement in the $f(E_\gamma)$ of ^{138}La at $E_\gamma \leq 1.7$ MeV, 2) a small resonance in $f(E_\gamma)$ of ^{139}La at $E_\gamma \approx 6.4$ MeV, and 3) a plateau behaviour between 2 and 4 MeV for both La isotopes.

The low-energy enhancement, discussed in detail in section 2.5, has been observed, using the Oslo Method (see section 2.1) which the same technique used in the present work, in all light to medium mass isotopes (^{44,45}Sc [22], ^{50,51}V [36], ^{44,45,46}Ti [37, 38, 39], ^{56,57}Fe [41], $^{93-98}$Mo [42]) with the possible transitional region reported in ^{106,107}Cd [43]. The existence of the low-energy enhancement has been independently confirmed for ^{95}Mo using a different experimental setup and extraction technique reported in Ref. [44]. Moreover, if the up-bend is a statistical feature it has to be independent of E_x. In the present work, the $f(E_\gamma)$ of ^{138}La was extracted from two different E_x regions, 3.5 MeV $\leq E_x \leq$5 MeV and 5 MeV $\leq E_x \leq$ 7.1 MeV. The low-energy en-

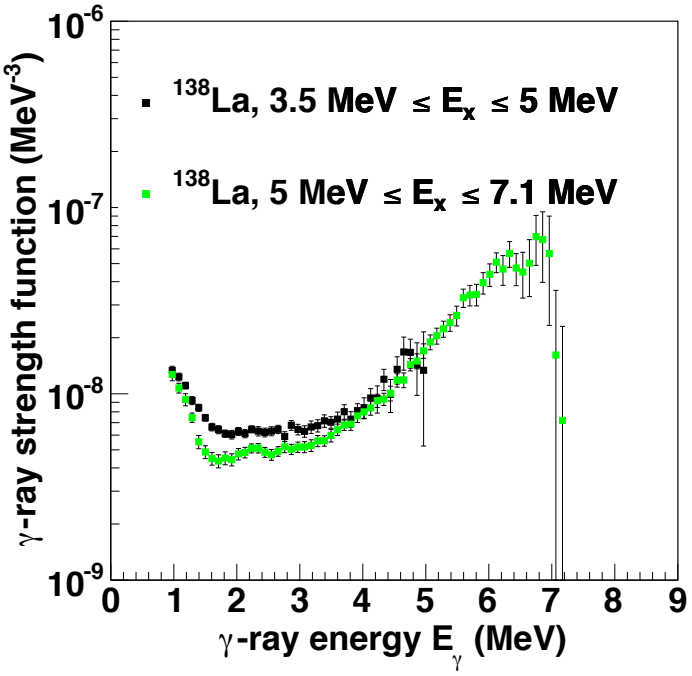

Figure 5.1: Radiative strength function of ^{138}La extracted from two different regions of E$_x$.

hancement is clearly visible in both cases, in fact the overall $f(E_\gamma)$ for both E_x regions is very similar (see figure 5.1). This suggests that the up-bend is indeed independent of the E_x region, within which the first-generation matrix is factorized, and supports the validity of the Brink hypothesis. The unexpected appearance of the enhancement in ^{138}La also suggests that this feature is not confined to specific mass regions as assumed prior to this work but may be found across the nuclear chart.

No conclusive theoretical results exist which can reproduce or explain these experimental observations although different models have suggested that the low-energy enhancement may be due to: 1) a reorientation of the spins of high-j neutron and proton orbits producing $M1$ transitions [45], and 2) transitions within the single-particle continuum producing $E1$ radiation [46]. It is intriguing to note that ^{138}La is located within a predicted region of magnetic

rotation (at Z = 57 and N = 81, see figure 5.2) [65] which is consistent with the theoretical approach 1).

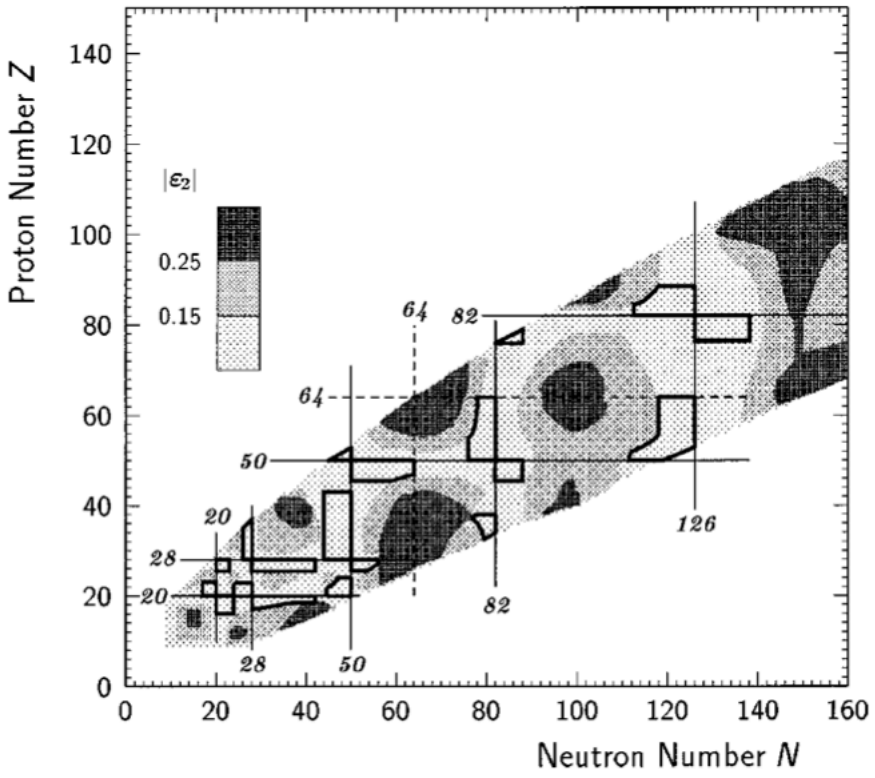

Figure 5.2: Magnetic rotation in different mass regions. The predicted regions are enclosed by solid lines [65].

The observation of the resonance at 6.4 MeV and labeled "RES1" in figure 4.23 is in excellent agreement with a previous ^{139}La(γ,γ') measurement reported in Ref. [9] (see figure 5.3, the red solid circles). Its origin has been discussed to be an $E1$ pygmy resonance.

The measured $\rho(E_x)$ for both La nuclei are in decent agreement with the ones calculated with the HFB + Combinatorial Model (see figure 5.4). For ^{138}La the agreement is excellent while for ^{139}La the experimental $\rho(E_x)$ is somewhat larger than the calculated $\rho(E_x)$ between 1.25 and 3.8 MeV. It can be noticed from figure 4.22 that these measured $\rho(E_x)$ have very similar slopes, but the

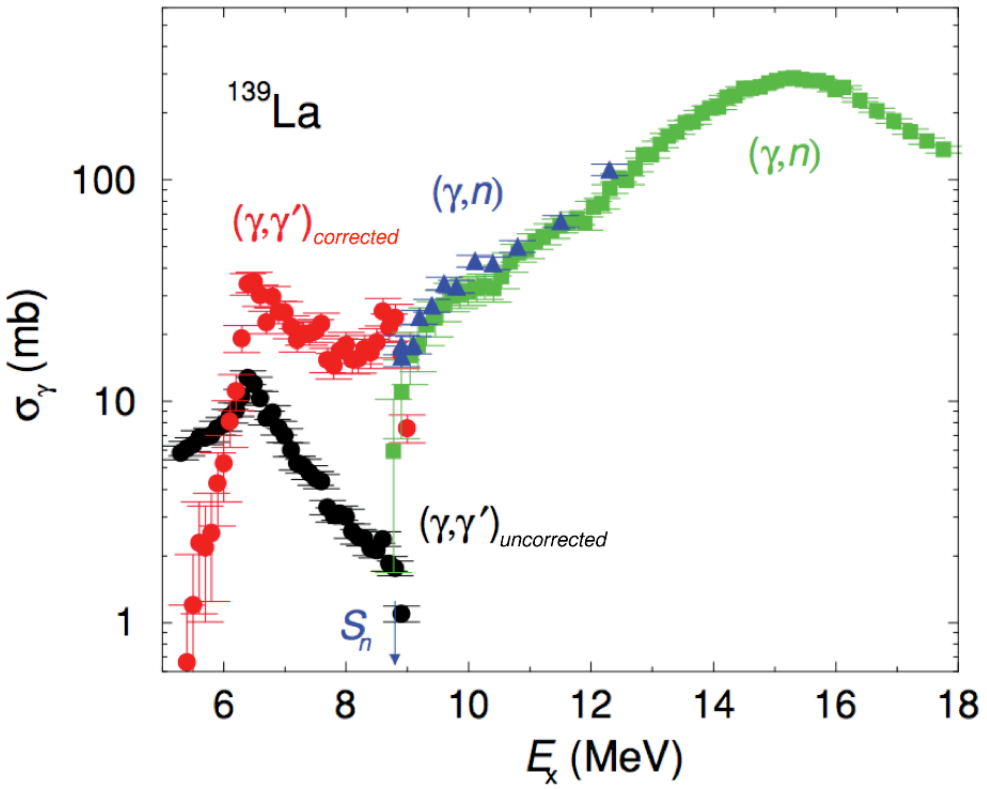

Figure 5.3: cross-section of ^{139}La measured in the ^{139}La(γ,γ') experiment (black and red data) [9]. The (γ,n) data were measured by Ref. [47] (green data) and Ref. [63] (blue data).

$\rho(E_x)$ of ^{138}La is higher compared to $\rho(E_x)$ of ^{139}La. This is an expected feature since ^{138}La is an odd-odd nucleus which gives it an extra degree of freedom.

It will be interesting to explore the existence of the low-energy enhancement across the nuclear chart. Further, the low-energy enhancement has been only measured using stable beams and targets, but many r-process calculations rely on the extrapolation of these data. Measurements of the $f(E_\gamma)$ and $\rho(E_x)$ for neutron-rich nuclei at radioactive ion beam facilities are desirable to investigate if the up-bend persists towards the neutron-drip line.

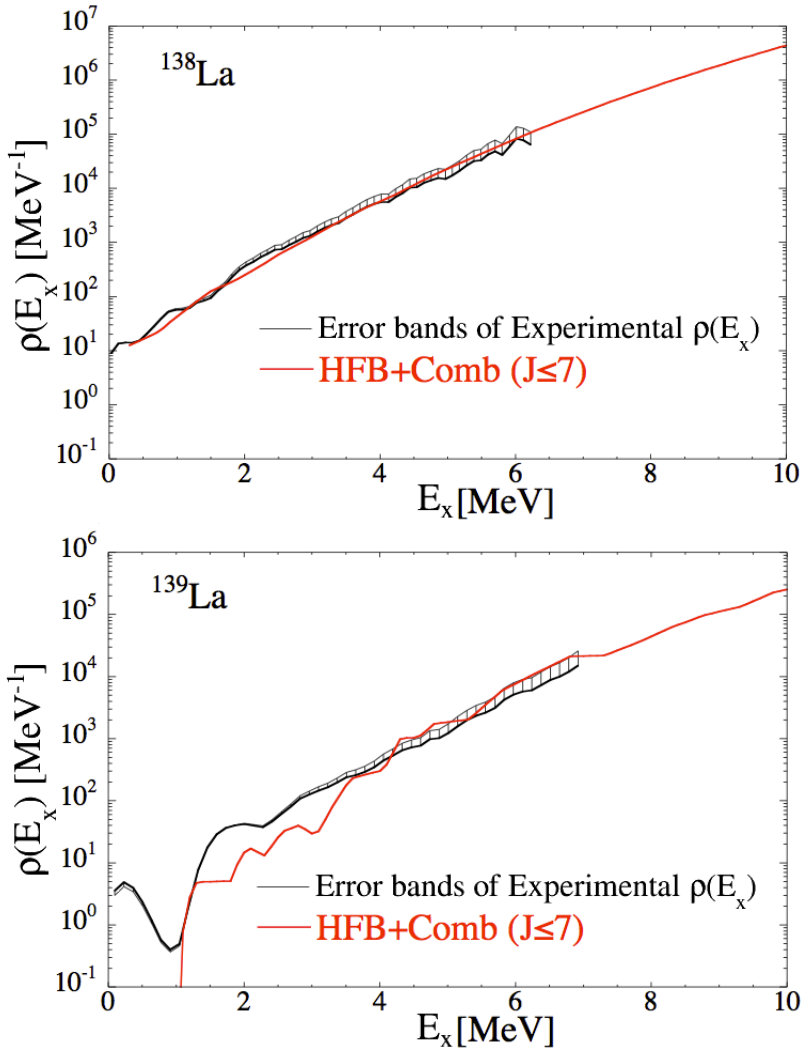

Figure 5.4: Comparison of the HFB + Combinatorial model and experimental nuclear level density.

5.2 Astrophysical Neutron Capture cross-section Calculations

To estimate the ^{137,138}La radiative neutron capture cross-sections and the corresponding reverse photoneutron emission rates of astrophysical interest, statistical model calculations were carried out using the TALYS code as discussed in section 2.6. Some of the principal ingredients of these calculations are $f(E_\gamma)$ and $\rho(E_x)$. As far as the strength function is concerned, the new experimental

results are now considered and entered directly in the TALYS calculation of the electromagnetic transmission coefficients. Indeed, the present experiment provides a direct measurement of the $f(E_\gamma)$ up to S_n. For incident neutron energies, typically below 1 MeV, it is found that the energy window giving rise to the dominant contribution to the neutron capture cross-section corresponds to photon energies of ≈ 3 to 7 MeV (see figure 5.5), i.e. energies at which the $f(E_\gamma)$ have now been determined experimentally (figure 4.23). The $\rho(E_x)$ also plays an important role in the calculation of the radiative capture cross-section. By default, the calculations use the $\rho(E_x)$ of the HFB + Combinatorial model, normalized to the experimental cumulative number of low-lying states, as well as the s-wave resonance spacings (with their corresponding error bars) at S_n (see Table 4.1). The calculated nuclear level densities are in general agreement with the experimental ones (see figure 5.4).

The final neutron capture cross-sections, $\sigma(E_n)$, including the uncertainties affecting the $f(E_\gamma)$ and the $\rho(E_x)$ (Table 4.1), are given in figure 5.6. The uncertainties of the $f(E_\gamma)$ were modified from those shown in figure 4.23 with the upper error bars obtained by replacing D_0 by $D_0 - \Delta D_0$ and $\langle\Gamma(S_n)\rangle$ by $\langle\Gamma(S_n)\rangle + \langle\Delta\Gamma(S_n)\rangle$ during normalization of $f(E_\gamma)$. The lower error bars of the $f(E_\gamma)$s were obtained by replacing D_0 by $D_0 + \Delta D_0$ and $\langle\Gamma(S_n)\rangle$ by $\langle\Gamma(S_n)\rangle - \langle\Delta\Gamma(S_n)\rangle$. This modification is necessary because the error bars obtained with the Oslo Method do not include the uncertainties of the D_0 and $\langle\Gamma(S_n)\rangle$, which significantly contribute to the error bars. For ^{138}La the new uncertainties in $f(E_\gamma)$ are $^{+52}_{-34}\%$ at $E_\gamma = 7.2$ MeV and gradually decreasing to $^{+15}_{-17}\%$ at $E_\gamma = 1.0$ MeV, while for ^{139}La the ranges are $^{+69}_{-39}\%$ at $E_\gamma = 8.6$ MeV and decreasing to $^{+15}_{-15}\%$ at $E_\gamma = 1.7$ MeV. This is illustrated in figure 5.7 which shows the corresponding error bands and the observed $f(E_\gamma)$. The corresponding astrophysical Maxwellian-averaged cross-sections amount to $\langle\sigma\rangle = 366 \pm 126$ mb and 116 ± 44 mb for $^{137}\mathrm{La}(n,\gamma)^{138}\mathrm{La}$ at the s-process

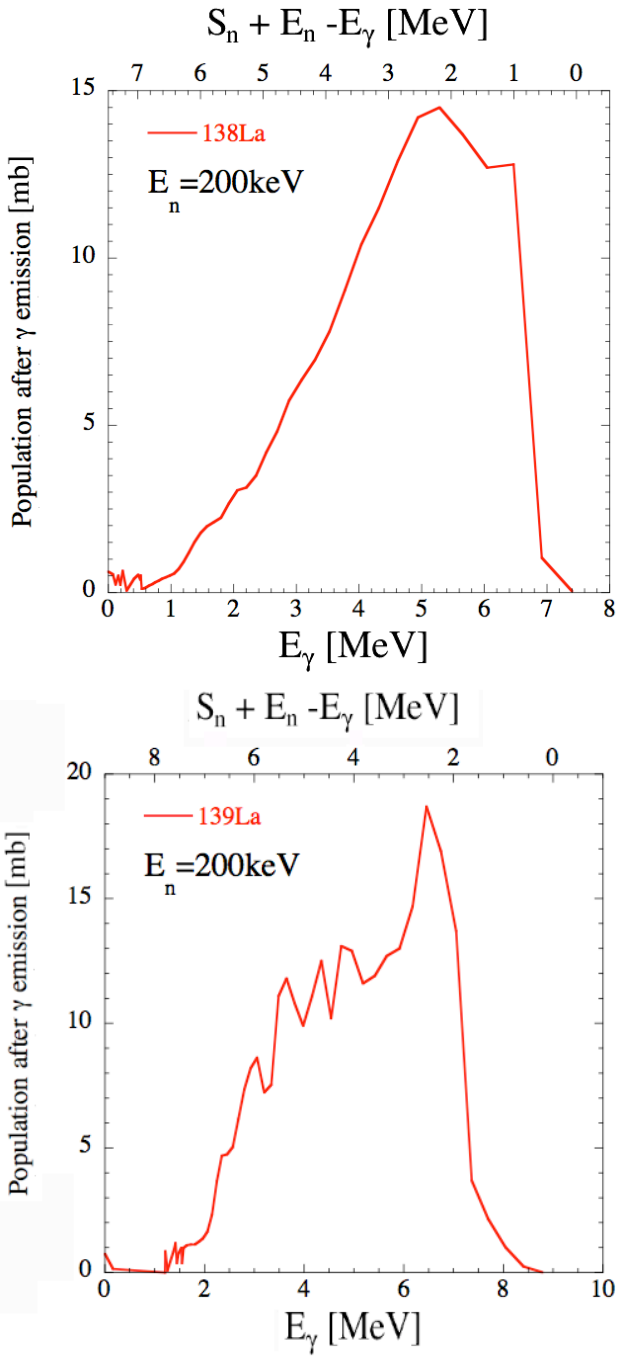

Figure 5.5: Population of ^{138}La (upper panel) and ^{139}La (lower panel), after binary γ emission, through the (n, γ) reaction calculated with the TALYS code.

thermal energy of $kT = 30$ keV (i.e. a temperature of $T = 3.5 \times 10^8$ K) and at the p-process energy of 215 keV ($T = 2.5 \times 10^9$ K), respectively. For $^{138}\mathrm{La}(n, \gamma)^{139}\mathrm{La}$, the obtained values are 618 ± 174 mb and 54 ± 20 mb at

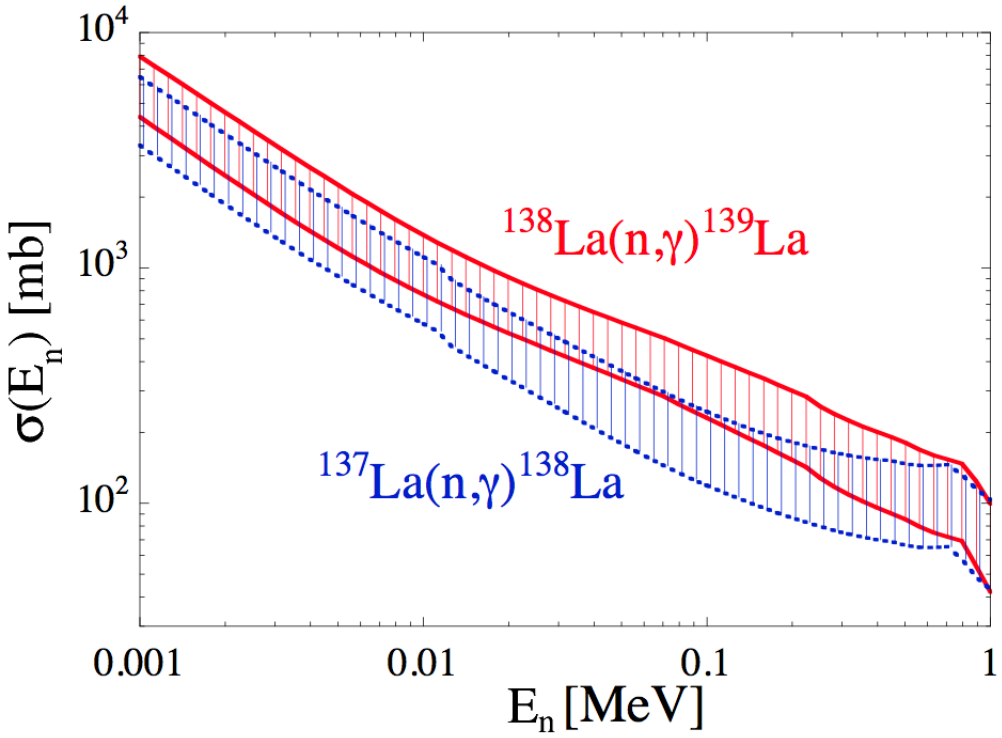

Figure 5.6: $^{137}\mathrm{La}(n,\gamma)^{138}\mathrm{La}$ (dashed line) and $^{138}\mathrm{La}(n,\gamma)^{139}\mathrm{La}$ (solid line) cross-sections as a function of neutron energy.

$T = 3.5 \times 10^8$ K and 2.5×10^9 K, respectively.

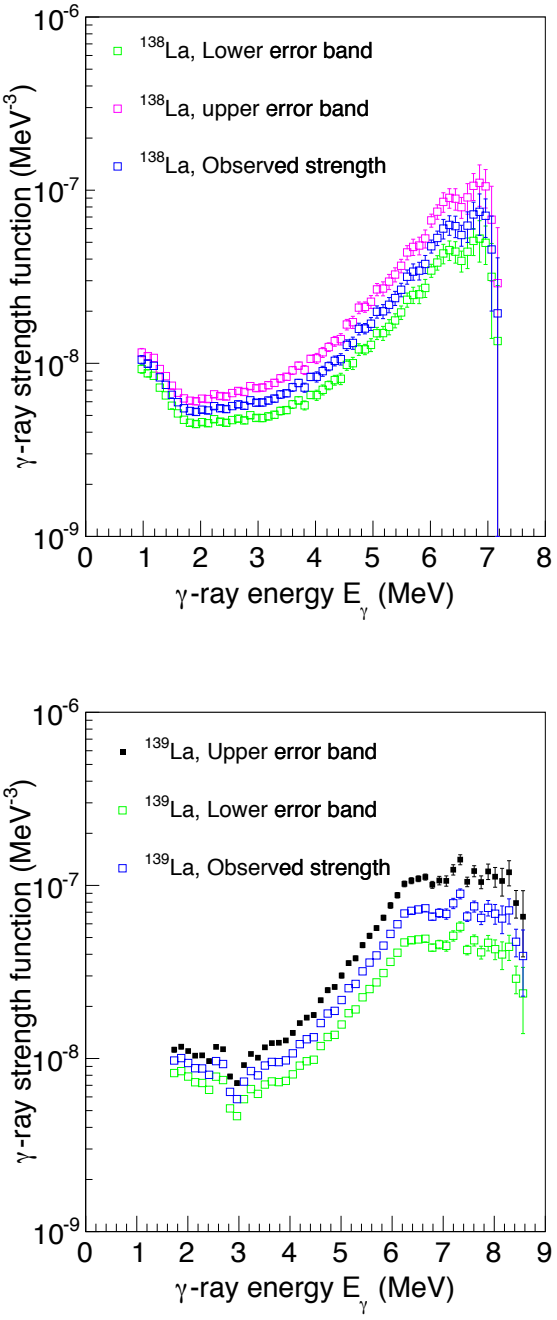

Figure 5.7: Modified error bands of the $f(E_\gamma)$ of ^{138,139}La, to take D_0 and $\langle\Gamma(S_n)\rangle$ uncertainties into account, and corresponding measured $f(E_\gamma)$.

5.3 ^{138}La Galactic Production

The newly calculated ^{138}La$(n,\gamma)^{139}$La cross-section at $T = 3.5 \times 10^8$ K is about 45% larger than the theoretical value compiled in Ref. [66]. At the p-process temperature $T = 2.5 \times 10^9$ K (215 keV), the Maxwellian-averaged cross-sections (MACS) of 116 ± 44 mb and 54 ± 20 are close (within less than 15%) to the values of 123 mb and 62 mb derived in Ref. [3] for ^{137}La and ^{138}La, respectively. On the basis of detailed balance relations, the calculated MACS correspond to ^{139}La$(\gamma,n)^{138}$La reaction rates that are smaller than the destructive ^{138}La$(\gamma,n)^{137}$La rates. Therefore, from these derived cross-sections it can be deduced [3] that the synthesis of ^{138}La through photodisintegration processes cannot be efficient enough to account for the observed abundance.

There are various plausible astrophysical sites for the p-process to take place that have been suggested. These include pre-supernova phases of massive stars and Type Ib/Ic supernovae stages following the loss of their hydrogen envelope prior to the explosion [67]. However, the O/Ne-rich layer of Type II supernova is the most promising and quantitatively studied site [3, 67, 5], because i) the minimum temperature of $\approx 1.5\times10^9$ K is required for the photodisintegration process to take place, ii) this temperature must not exceed 3.5×10^9 K to prevent strong photoerosion of heavy nuclei and iii) it is also mandatory to freeze-out the p-process on a short enough time scale on the order of 1 second. These conditions are well satisfied in the deep O/Ne-rich layers of massive (typically $25\,M_\odot$) stars exploding as Type II supernova.

To investigate the impact of these new reaction rates (see section 5.2) on the ^{138}La p-process production, nucleosynthesis calculations in the O/Ne-rich layers of Type II supernovae for a solar metallicity star of $25\,M_\odot$ were performed, in the absence of neutrino nucleosynthesis. The model used is discussed in section 2.6 (more details on the nucleosynthesis can be found in Refs. [3, 68];

note, however, that theoretical rates are determined here using the TALYS code [8, 53]). The resulting overproduction factors (with respect to the solar abundances) in the 0.75 $M_\odot$ p-process layers are shown in figure 5.8, where the upper and lower limits on the ^{138}La abundance are obtained with the reaction rates from this work (figure 5.6). This newly calculated mean overproduction factor (see figure 5.8) shows that ^{138}La remains underproduced by a factor of about 10 with respect to the neighbouring p-nucleus ^{138}Ce. The determination of the reaction rates with the improved statistical parameters therefore shows that ^{138}La cannot be produced by photoreactions during the standard p-process. These results put the ν-process (ν_e + ^{138}Ba $\rightarrow$ e$^-$ + ^{138}La) as the dominant production process for ^{138}La on a very strong footing.

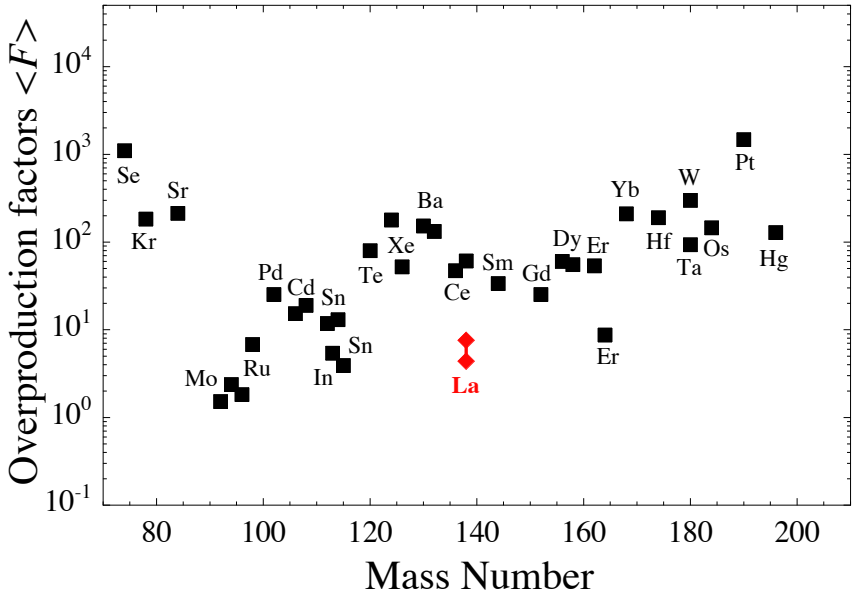

Figure 5.8: p-nuclide overproduction factors $\langle F \rangle$ in the 0.75 $M_\odot$ p-process layers of a 25 $M_\odot$ Type II supernova, as a function of the mass number A.

The synthesis of ^{138}La in the ν-process is thought to be taking place in the O/Ne-rich layers of core-collapse supernovae when all flavors of neutrinos,

emerging from the proto-neutron stars, flow through this layer [69]. Figure 5.9 illustrates the different layers of a massive star. The synthesis of ^{138}La through ν-induced reactions was suggested by S.E. Woosley *et al.* [6]. The first quantitative analysis of the production of this p-isotope through ν-reactions, in the O/Ne-rich layers of core-collapse supernovae of 25 $M_{\odot}$ stars, was performed by S. Goriely *et al.* [3] (see figure 1.4). The ^{138}La solar abundance was found to be produced by the charged-current and neutral-current reactions, ^{138}Ba(ν_e, e$^-$)^{138}La and ^{139}La (ν_x, $\nu'_x n$)^{138}La where $x = \tau$ and μ, respectively.

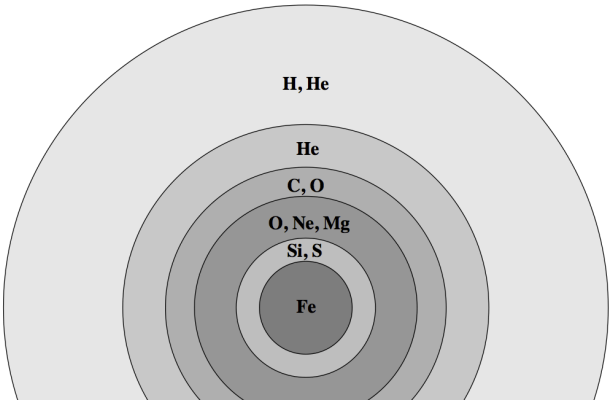

Figure 5.9: Schematic layout of onion-skin of a massive star ($M > 8\,M_{\odot}$) at the end of its evolution [71].

However, the ^{139}La (ν_x, $\nu'_x n$)^{138}La reaction was found to be insignificant compared to the ^{138}Ba(ν_e, e$^-$)^{138}La reaction. This was later confirmed (see figure 5.10) by A. Heger *et al.* [70] using improved cross-sections based on random phase approximation calculations. The estimated cross-sections for ν_e-capture on ^{138}Ba and ν_x neutron knockout by ^{139}La are on the order of 10^{-14} mb at neutrino temperatures, T_{ν}, of 4 and 6 MeV, respectively [3, 70]. Furthermore, the cross-section for ^{138}Ba(ν_e, e$^-$)^{138}La has been recently improved on the basis of experimental Gamow-Teller strength distribution in ^{138}La and confirmed to be on the order of 10^{-14} mb [72]. In fact, the improved cross-section, 7.4×10^{-14} mb, for ^{138}Ba(ν_e, e$^-$)^{138}La is in excellent agreement with 7.5×10^{-14} mb estimated by Ref. [3]. The results from Ref. [72] further confirm that the

charged-current interaction is needed to explain the ^{138}La solar abundance and that $T_\nu = 4$ MeV is sufficient.

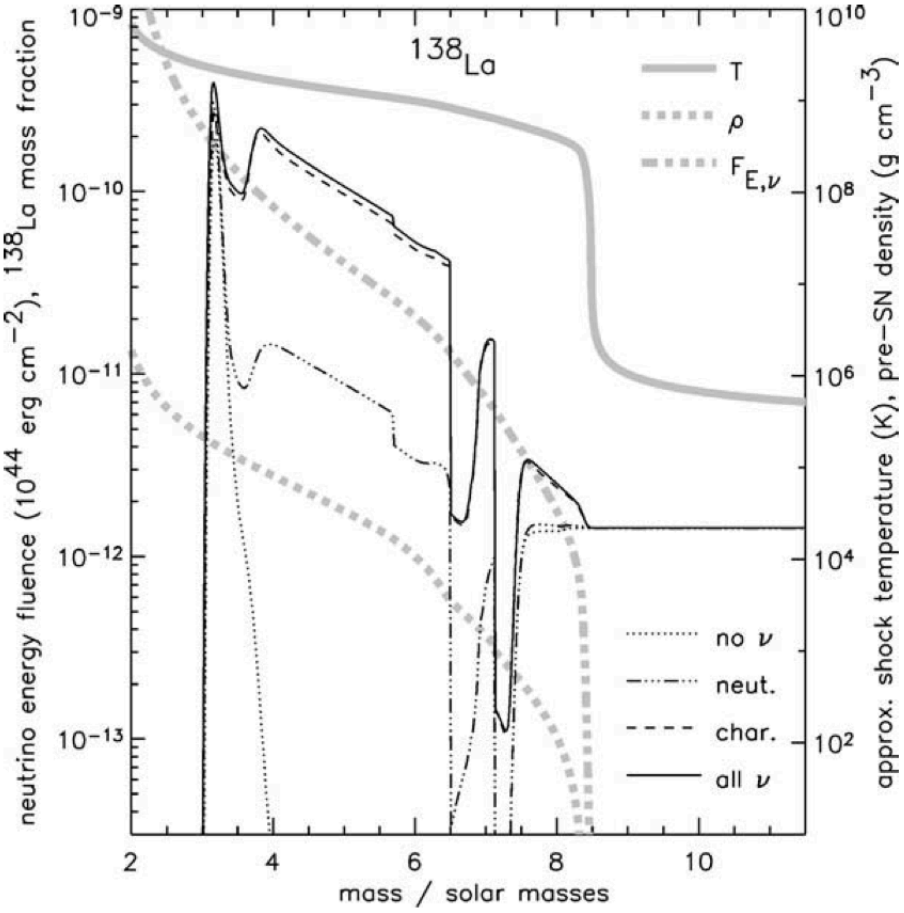

Figure 5.10: Production of ^{138}La in the supernova of a 25 $M_\odot$ star. The production without neutrinos, with charged-current reaction ^{138}Ba(ν_e, e$^-$)^{138}La, with the neutral current reaction ^{139}La (ν_x, $\nu'_x n$)^{138}La and both reactions are denoted by no ν, char., neut. and all ν, respectively [70].

It is desirable to directly measure the cross-sections for the ^{138}Ba(ν_e, e$^-$)^{138}La and ^{139}La (ν_x, $\nu'_x n$)^{138}La reactions in order to confirm the quantitative argument of Ref. [3]. This would be accomplished by exposing ^{138}Ba and ^{139}La to neutrino environments similar to the one existing in O/Ne-rich layers of core-collapse supernovae. However, challenges of artificially generating ν environments with the required flux on earth, combined with the very small an-

ticipated cross-sections make a direct measurement impractical with currently available technologies.

Chapter 6

Summary and Conclusions

The origin of the rare earth p-nucleus ^{138}La has been an open question for a long time. In particular uncertainty exists whether this p-isotope is synthesized by photodisintegration of s- and r-seed nuclei or in the ν_e-process. The nucleosynthesis calculations performed by S. Goriely *et al.* [3] show that the observed solar abundance of this nucleus cannot be accounted for through the p-process but is reproduced by invoking the $\nu_e + {}^{138}\mathrm{Ba} \rightarrow \mathrm{e}^- + {}^{138}\mathrm{La}$ reaction, which takes place in the O/Ne-rich layers of core-collapse supernovae. The ^{138}La underproduction in the p-process could still not be confirmed with certainty, due to the unavailability of experimental $f(E_\gamma)$ and $\rho(E_x)$ data for ^{138,139}La, which are critical ingredients to Hauser-Feshbach calculations on which the ^{138}La production and destruction rates are based.

These statistical parameters have now been successfully measured for the first time, below S_n, for ^{138}La and below 6 MeV excitation energy for ^{139}La, using the ^{139}La(^{3}He, $\alpha\gamma$) and ^{139}La(^{3}He, ^{3}Heγ) reactions. The Oslo Method used for the data analysis utilizes detected particle-γ coincidence events. The charged particles were detected using the SiRi array, while the γ rays in coincidence with these charged ejectiles were detected using the CACTUS array. The $^{138}\mathrm{La}(n,\gamma)^{139}\mathrm{La}$ and $^{137}\mathrm{La}(n,\gamma)^{138}\mathrm{La}$ cross-sections of 54 ± 20 and 116 ± 44

mb, corresponding astrophysical MACS at the p-process temperature, $T_9 = 2.5$, have been calculated. These calculations were performed with the TALYS reaction code, using the experimentally measured $f(E_\gamma)$ and $\rho(E_x)$ calculated within the HFB + Combinatorial model and compared to experimental data. These MACS were used to calculate the abundance of ^{138}La within astrophysical reaction network calculations and their impact on the ^{138}La p-process production has been investigated.

These nucleosynthesis calculations show that even with the newly measured properties, ^{138}La cannot be sufficiently produced by photodisintegration of s- and r-process seed nuclei in O/Ne-rich layers of Type II supernovae. It is therefore concluded that the results of the present work put the ν_e capture on ^{138}Ba on a very strong footing as the dominant production process for the neutron-deficient ^{138}La nucleus.

Future measurements of the $f(E_\gamma)$ and $\rho(E_x)$ in particular for neutron-rich nuclei are necessary to understand the existence of the low-energy enhancement. Direct ν-process measurement are desirable but impractical with today's technology.

Bibliography

[1] I. J. Thompson and F. M. Nunes, *Nuclear Reactions for Astrophysics*, (Cambridge University Press, 2009).

[2] K. Sonnabend *et al.*, Eur. Phys. J. A 27, 149 (2006).

[3] S. Goriely *et al.*, A & A 375, L35 (2001).

[4] H. Schatz *et al.*, Phys. Rev. Lett. 86, 16 (2001).

[5] M. Rayet *et al.*, A & A 298, 517 (1995).

[6] S.E. Woosley *et al.*, Astrophys. J. 356, 272 (1990).

[7] T. Kajino, *et al.*, J. Phys. G: Nucl. Part. Phys. 41, 044007 (2014).

[8] A.J. Koning *et al.*, *Nuclear Data for Science and Technology* (EDP Sciences; eds O. Bersillon *et al.*), p. 211 (2008) (see also http://www.talys.eu)

[9] A. Makinaga *et al.*, Phys. Rev. C 82, 024314 (2010).

[10] R. Cayrel *et al.*, Nature 409, 691 (2001).

[11] S. Goriely *et al.*, Phys. Rev. C 78, 064307 (2008).

[12] A. Schiller *et al.*, Nucl. Instr. and Meth. Phys. Res. A 447, 498 (2000).

[13] A.C. Larsen *et al.*, Phys. Rev. C 83, 034315 (2011).

[14] M. Guttormsen *et al.*, Nucl. Instr. and Meth. Phys. Res. A 374, 371 (1996).

[15] A. C. Larsen, PhD thesis, University of Oslo, 2008.

[16] M. Guttormsen *et al.*, Nucl. Instr. and Meth. Phys. Res. A 255, 518 (1987).

[17] E. Fermi, *Nuclear Physics*, (University of Chicago Press, Chicago, 1950).

[18] N. Bohr, Nature 137, 344 (1936).

[19] D. M. Brink, Ph.D. thesis, Oxford University, 1955, pp. 101-110.

[20] R. Capote *et al.*, Reference Input Parameter Library, RIPL-2 and RIPL-3; available online at http://www-nds.iaea.org/RIPL-3/

[21] www.nndc.bnl.gov.

[22] A.C. Larsen *et al.*, Phys. Rev. C 76, 044303 (2007).

[23] H.K. Toft *et al.*, Phys. Rev. C 81, 064311 (2010).

[24] H.T. Nyhus *et al.*, Phys. Rev. C 81, 024325 (2010).

[25] A. Gilbert and A.G.W. Cameron, Can. J. Phys. 43, 1446 (1965).

[26] T. von Egidy and D. Bucurescu Phys. Rev. C 80, 054310 (2009).

[27] S. Hailare and S. Goriely, Nucl. Phys. A 779, 63 (2006).

[28] M. Baranger *et al.*, *Advances in Nuclear Physics*, (Plenum Press, New York 7, 1973).

[29] J. Speth and J. Wambach, *Electric and Magnetic Giant Resonances in Nuclei*, (World Scientific Publishing Co. Pte. Ltd 7, 1991).

[30] W. Greiner and J. A. Maruhn, *Nuclear Models*, (Springer, 1996).

[31] W. Ziegler *et al.*, Phys. Rev. Lett. 65, 2515 (1990).

[32] D. Savran *et al.*, Progress in Particle and Nuclear Physics 70, 2013 (210).

[33] K. Heyde *et al.*, Rev. Mod. Phys. 82, 2365 (2010).

[34] J. Kopecky and M. UHL, Phys. Rev. C. 41, 1941 (1990).

[35] J. Kopecky *et al.*, Phys. Rev. C 47, 312 (1993).

[36] A.C. Larsen *et al.*, Phys. Rev. C 73, 064301 (2006).

[37] A.C. Larsen *et al.*, Phys. Rev. C 85, 014320 (2012).

[38] N.U.H. Syed *et al.*, Phys. Rev. C 80, 044309 (2009).

[39] M. Guttormsen *et al.*, Phys. Rev. C 83, 014312 (2011).

[40] A. Voinov *et al.*, Phys. Rev. Lett. 93, 14 (2004).

[41] A.C. Larsen *et al.*, Phys. Rev. Lett. 111, 242504 (2013).

[42] M. Guttormsen *et al.*, Phys. Rev. C. 71, 044307 (2005).

[43] A.C. Larsen *et al.*, Phys. Rev. C 87, 014319 (2013).

[44] M. Wiedeking *et al.*, Phys. Rev. Lett. 108, 162503 (2012).

[45] R. Schwengner *et al.*, Phys. Rev. Lett. 111, 232504 (2013)

[46] E. Litvinova and N. Belov, Phys. Rev. C. 88, 031302(R) (2013).

[47] H. Beil *et al.*, Nucl. Phys. A227, 427 (1974).

[48] A. C. Larsen and S. Goriely, Phys. Rev. C 82, 014318 (2010).

[49] H.K. Toft *et al.*, Phys. Rev. C 83, 044320 (2011).

[50] S. Goriely, Phys. Lett. B. 436, 10 (1998).

[51] S. Goriely and M. Arnould, A & A. 312, 327 (1996).

[52] M. Thoennessen (MSU) adopted from S. Goriely, Phys. Lett. B 436, 10 (1998).

[53] S. Goriely *et al.*, A & A 487, 467 (2008).

[54] D. Belkic, *Principles of Quantum Scattering Theory*, (Institute of Physics Publishing, 2004).

[55] M. Rayet *et al.*, A & A 227, 271 (1990).

[56] M. Guttormsen *et al.*, Nucl. Instr. and Meth. Phys. Res. A 648, 168 (2011).

[57] M. Guttormsen *et al.*, Phys. Scr. T32, 54 (1990).

[58] https://unarydigits.com/jkinz/

[59] W. R. Leo *et al.*, *Techniques for Nuclear and Particle Physics Experiments*, (Springer-Verlag, New York, 1994) 2^{nd} revised ed.

[60] S. F. Mughabghab, *Atlas of Neutron Resonances*, (Elsevier Science, Amsterdam, 2006). 5^{th} ed.

[61] S. Siem *et al.*, Phys. Rev. C 65, 044318 (2002).

[62] H.T. Nyhus *et al.*, Phys. Rev. C 85, 014323 (2012).

[63] H. Utsunomiya *et al.*, Phys. Rev. C 74, 025806 (2006).

[64] H. Beil and *et al.*, Nucl. Phys. A172, 426 (1971).

[65] S. Frauendorf, Rev. Mod. Phys 73, 463 (2001).

[66] Z. Y. Bao *et al.*, Atomic Data and Nuclear Data Tables 76, 70 (2000).

[67] M. Arnould and S. Goriely, Phys. Rep. 384, 1 (2003).

[68] M. Arnould *et al.*, Phys. Rep. 450, 97 (2007).

[69] T. Kajino *et al.*, J. Phys. G: Nucl. Phys. 41, 04407 (2014).

[70] A. Heger *et al.*, Phys. Lett. B 606, 258 (2005).

[71] http://www.astro.uni-bonn.de/∼nlanger/siu_web/ssescript/new/chapter11.pdf.

[72] A. Byelikov *et al.*, Phys. Rev. Lett. 98, 082501 (2007).

Appendix

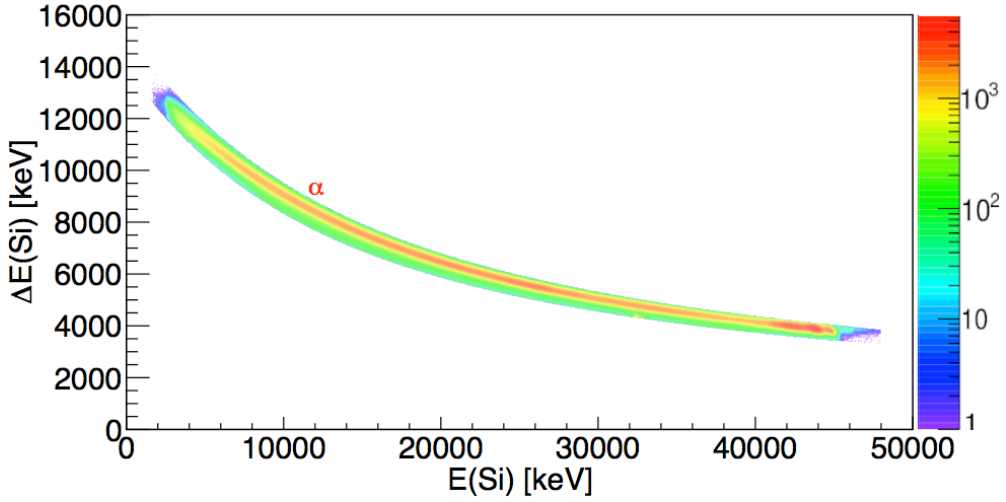

Figure 6.1: The $\Delta E - E$ plot for the ^{139}La(^{3}He, X) experiment gated on α particles.

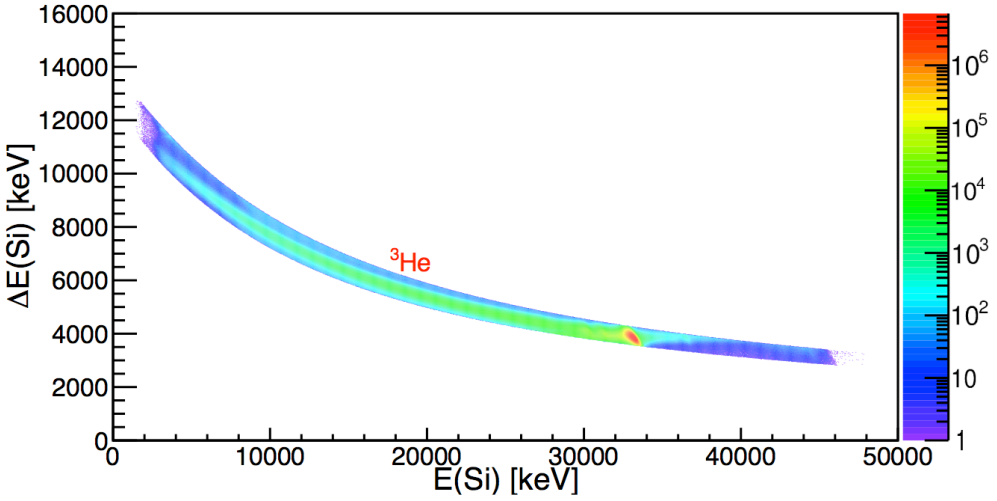

Figure 6.2: The $\Delta E - E$ plot for the ^{139}La(^{3}He, X) experiment gated on ^{3}He.

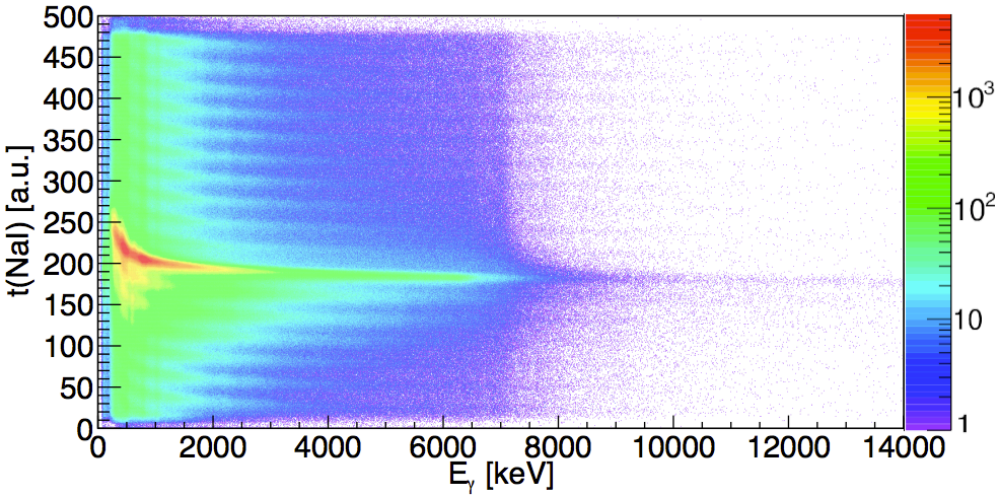

Figure 6.3: The energy-time matrix for the ^{139}La(^{3}He, $\alpha\gamma$)^{138}La reaction of the CACTUS array.

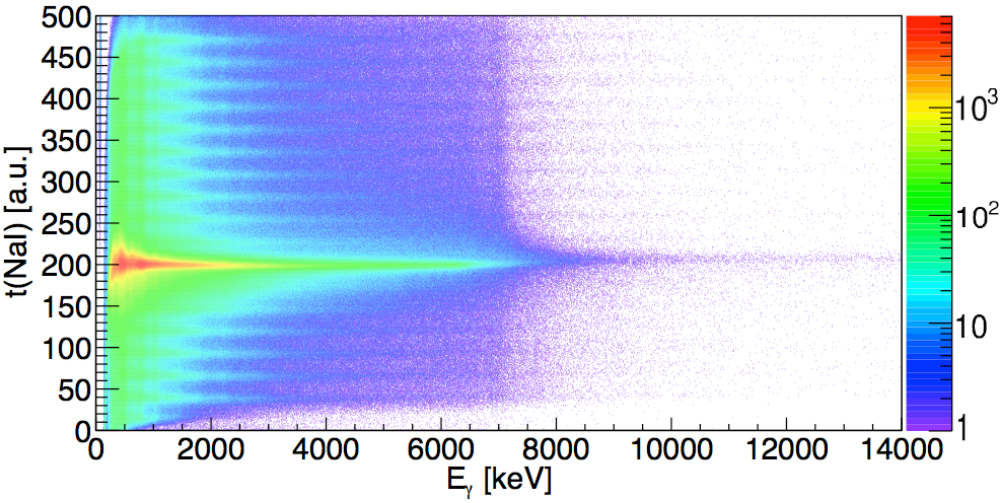

Figure 6.4: The energy-time matrix from the ^{139}La(^{3}He, $\alpha\gamma$)^{138}La reaction after *walk* correction for the CACTUS array.